12-2016

Generation and Microwave Scattering Diagnostics of Small Volume Plasmas

Jordan Chase Sawyer
University of Tennessee, Knoxville, jsawyer9@utk.edu

Recommended Citation

Sawyer, Jordan Chase, "Generation and Microwave Scattering Diagnostics of Small Volume Plasmas. " PhD diss., University of Tennessee, 2016.
https://trace.tennessee.edu/utk_graddiss/4162

To the Graduate Council:

I am submitting herewith a dissertation written by Jordan Chase Sawyer entitled "Generation and Microwave Scattering Diagnostics of Small Volume Plasmas." I have examined the final electronic copy of this dissertation for form and content and recommend that it be accepted in partial fulfillment of the requirements for the degree of Doctor of Philosophy, with a major in Aerospace Engineering.

Zhili Zhang, Major Professor

We have read this dissertation and recommend its acceptance:

Kivanc Ekici, Feng-Yuan Zhang, Vasilios Alexiades

Accepted for the Council:
Carolyn R. Hodges

Vice Provost and Dean of the Graduate School

(Original signatures are on file with official student records.)

Generation and Microwave Scattering Diagnostics of Small Volume Plasmas

A Dissertation Presented for the

Doctor of Philosophy

Degree

The University of Tennessee, Knoxville

Jordan Chase Sawyer

December 2016

ACKNOWLEDGEMENTS

Any meaning or achievement derived from the following pages was brought on by the love and gift of having these people in my life.

My grandmother Sammie Hensley has taught me about strength and dignity. As a survivor of polio, her ferocity of independence has only been matched by her love of God and family. My grandmother Pat Owen's taught me so much about human nature and curiosity. The wisdom she passed on to me has shaped how I see the world and try to find my place in it. My grandfather RT Rogers had a heart for sacrifice and family.

My mother Pam Sawyer has always shown me unbounded love and set an example for how to live a life built on generosity. My father Dale Sawyer has shown me how to build a family based on commitment and hard work. My sisters Brittany and Bailey have always been sources of constant joy and surprising youthful wisdom.

My friends Thomas Gietema and Rob Sawyer are the brothers I feel I have always had and can always rely on. My friends John and Emily Clark have bestowed empathy and advice during some of the more troublesome times that accompanies any young graduate student's life.

My advisor Dr. Zhili Zhang has always given me the guidance and patience I needed to grow as a researcher. His example as a mentor will be next to impossible to ever live up to due to his enthusiasm for research and commitment to those under his tutelage.

ABSTRACT

This dissertation focuses on the development of novel generation and microwave scattering diagnostic techniques for small volume plasmas. The small volume plasmas presented in this work fall under the two generalized categories: 1) laser-induced plasmas and 2) non-equilibrium microdischarges.

Chapter I presents the application of microwave scattering theory to laser-induced breakdown in air. The MIE solution to Maxwell's equations is employed to reveal three distinct phases of the evolution of the laser-induced breakdown in air. Chapter II presents a novel method of quantifying thresholds for laser-induced breakdown. These thresholds are established via total electron number measurement from dielectric calibration of microwave scattering. Chapter III presents high-repetition-rate (HRR) nanosecond laser pulse train scheme for laser ignition. Demonstration of the ignition of combustible gaseous mixtures is shown to have an order-of-magnitude reduction in per-pulse energy using the HRR LI method over traditional laser ignition methods.

Chapter IV presents ion-kinetic measurements of a laser induced plasma in sodium-argon and sodium-air gaseous mixtures. Coherent microwave Rayleigh scattering (Radar) from Resonance Enhanced Multi-Photon Ionization (REMPI) is utilized for the measurement of sodium ion neutral stabilized and cluster dissociative recombination rates. Chapter V presents rotational temperature measurements in a DC microdischarge produced in air. Radar REMPI measurements of O_2 rotational temperature is performed at eight axial locations between pin-to-pin electrodes. Chapter VI presents relative concentration measurements of atomic oxygen in DC and pulsed Discharges. Relative atomic oxygen concentrations were obtained via Radar REMPI. The effects of pressures, gas composition, and discharge voltage were explored for the DC and pulsed discharges. Comparisons between two-photon absorption laser induced fluorescence (TALIF) and Radar

REMPI techniques were made for atomic oxygen concentration measurements in a pulsed discharge. Chapter VII presents a method of reducing the breakdown voltage of a DC microdischarge via metal nanoparticle seeding. Reductions in the breakdown voltage were seen to be as high as 25% for a *PD* scaling of 40 Torr-cm from the seeding of iron and aluminum nanoparticles into the discharge gap.

TABLE OF CONTENTS

LIST OF TABLES

LIST OF FIGURES

INTRODUCTION

There is an ever growing number of small volume plasma applications in engineering disciplines. Small volume plasmas have characteristic lengths of a few millimeters down to 10's of microns that lead to many unique properties. Small volume plasmas produced by high intensity laser beams are broadly categorized as laser-induced plasmas, but they may manifest from one or more physical mechanism including: avalanche ionization (AI), direct multiphoton ionization (MPI), tunneling ionization (TI), and resonant enhanced multiphoton ionization (REMPI). Typically, a small volume plasma generated by electric fields produced by high-voltage direct current (DC), radio frequency (RF), or microwave sources is termed a microdischarge. In this work, unique approaches for the generation and microwave scattering diagnostics of these two types of small volume plasmas are explored.

Laser-induced plasmas have been extensively studied since the 1960s when laser sparks or laser-induced breakdown were first observed.[1-5] The application of laser-induced breakdown to energy deposition, material processing, diagnostics, and combustion have fueled this research. Flow control through the energy deposition of laser-induced plasmas has been proposed.[6, 7] In material processing, laser-induced plasmas have been used for thin film depositions.[8, 9] Laser Induced Breakdown Spectroscopy (LIBS) is a diagnostic technique that has been utilized in determining material compositions in the solid, liquid, and gaseous phases.[10-14] Laser-induced spark ignition has been shown to have many advantages over traditional combustion systems.[15, 16]

Laser-induced breakdown begins with the generation of seed electrons via multiphoton ionization (MPI) process, in which a gaseous atom or molecule simultaneously absorbs multiple photons to be ionized.[17] The seed electrons are then accelerated by the beam's electromagnetic field via the inverse Bremsstrahlung effect. If a sufficient field is applied, the electrons are accelerated to energies that cause electron impact ionization upon collisions with the neutral gas atoms and molecules. The newly liberated electrons then are accelerated by the field leading to an electron avalanche ionization (EAI) process during the laser pulse duration. The EAI process manifests as a visible laser spark which emits light and heats the surrounding medium producing a shock wave that propagates from the breakdown region. Various studies have focused on the effects of a range of parameters including those of the laser beam (i.e. laser wavelengths[18-20], laser pulse widths [21, 22], focal areas[23]), and gas pressures [24], and other gas properties on the laser-induced gas breakdown process with various diagnostics such as emission spectroscopy[25, 26], interferometry[27, 28] and Thomson scattering.[29, 30] These parameters have been shown to be related to either the MPI or EAI phases of the laser-induced gas breakdown process [31].

Even with years of extensive research, knowledge on the generation of laser-induced breakdown in air is still lacking key details, such as electron number density. Primarily, optical diagnostic techniques, such as optical emission spectroscopy and stark shifting, have been applied to laser-induced breakdown in air to determine plasma, thermodynamic, and transport properties.[32-34] Unfortunately, the limitations of achievable temporal and spatial resolutions of these methods make it difficult to study the avalanche ionization phase in laser-induced breakdown. Traditional microwave measurement methods, such as absorption and interferometry, are not effective due to the small dimensions of the plasma relative to the microwave wavelength.

Until recently the initiation of laser-induced gas breakdown was commonly detected by human eyes, photodiodes, and/or cameras with a probability-based criterion[21]. Typically, this criterion is the visible observation of a glow or flash in the focal region for a probability of 10%-50% of the laser firings.[20] Such criteria are qualitative in nature and maybe inaccurate. A visible spark produced by an intense laser beam generally occurs at the end of or after the laser pulse duration which cannot clearly reveal the MPI and EAI processes and their corresponding effects during the laser-induced gas breakdown processes. Moreover, at higher pressures self-absorption becomes prominent, possibly leading to inaccurately high intensity threshold measurements.

One of the main applications of laser-induced plasma is laser ignition (LI) in combustion systems. LI is an advanced ignition method that has several advantages over traditional electric spark plugs and gaseous torches for fuel-lean, high-pressure ignition environments [16, 35-38]. It also provides precise ignition timing, large penetration depth, and ignition at desired location(s) for optimal combustion performance. LI has been used for a wide variety of applications, including ignition of gaseous fuels for internal-combustion engines [39] and rocket engines [40] and initiation of nuclear fission/fusion reactions [41]. There is particular interest in the use of LI for stationary gas engines owing to the possibility of increased engine efficiency and reduced NOx emission [38]. Additionally, there is interest in using laser sparks for ignition of aircraft gas turbine engines to achieve rapid relight [42].

Among the available LI methods, the non-resonant breakdown LI technique has been the most widely used because of its simplicity in implementation and rapid ignition [16, 35-38]. In the Non-resonant breakdown LI process, seed electrons are generated through the non-resonant, multi-photon ionization process using a high-intensity laser pulse (intensity must exceed the air-breakdown threshold ~10^{11} W/cm^2). Subsequently, the electrons are accelerated via the inverse-bremsstrahlung process with the same intense pulse. Collisions between these accelerated electrons and other molecules liberate additional electrons and induce an electron avalanche that forms a laser-induced plasma. Joule heating of the surrounding combustible gaseous mixture and the production of highly reactive chemical intermediates leads to localized thermal runaway. Non-resonant LI pulse energy [i.e, minimum ignition energy (MIE)] varies with the applications but, in general, is ~10-20 mJ/pulse for natural-gas engines [43] and ~30-60 mJ/pulse for aero-turbine engines [44]. The MIE increases significantly when the fuel/air mixture becomes lean (i.e., equivalence ratio φ <0.7) [16, 35, 36, 44]. Additionally, the MIE increases with flow rate and flow turbulence level [45].

This conventional LI technique faces stiff challenges when implemented in practical engines and combustion devices where optical access is typically limited. During the past decade, researchers attempted to develop a fiber-optic beam-delivery system for LI [46-52]. However, because of the high-energy requirements for conventional LI, it remains difficult to deliver the required laser beam through flexible optical fibers for practical engine applications. A solid-core silica fiber with large core size (~1 mm) can transmit ~10 mJ/pulse [47-49, 53], which is barely sufficient for ignition. Hollow-core fibers, because of the absence of a solid core that enables a high damage threshold, have been used for delivering the required laser beam for ignition [48, 50]. However, since this fiber is very sensitive to bending loss, it not ideal for practical applications. Mullett et al. investigated various available fibers for LI and came to the conclusion that until significant advances in the development of optical fibers are made, the ability to reliably deliver the laser beam for single-pulse LI will be severely limited in real-world applications [48]. Recently Beaudou et al. [51] and Dumitrache et al. [52] demonstrated the delivery of high-energy laser pulses (~4 mJ/pulse of 10-ns-duration or ~30 mJ/pulse of 30-ns-duration) while maintaining high beam quality using a special hollow-core, photonic crystal fiber for ignition of a combustible mixture limited to near-stoichiometric conditions (φ ~1). In order to achieve LI in fuel lean or high speed flows, while not exceeding the fiber damage threshold, a deviation from the traditional single pulse methods may be necessary.

Osborne et al. [40] and Cheng et al. [54] report enhancement in igniting lean fuel/air mixtures using dual pulse (pulse spacing ~10-200 ns). Osborne et al. showed that extension of the laser spark lifetime and optimization of the local energy deposition are highly dependent on delays between two pulses [40]. Zhang et al. [55]showed that in atmospheric-pressure air, plasma enhancement can be achieved with two pulses that are separated by > 50 μs.

Laser-induced plasmas may also serve as a testbed laboratory plasma for limited study of ion kinetics. One example of such is presented by coherent Rayleigh scattering from a laser-induced plasma generated by resonance enhanced multiphoton ionization (REMPI) of vaporized alkali metals. The ion kinetics of alkali metals are of particular interest to the aerospace community. The unique combination of the relatively low ionization potential of alkali metals and the high temperatures behind the bow shock of a hypersonic vehicle in flight allows for rapid vaporization and thermal ionization of alkali metals.[56] Studies have shown that the electrical conductivity of the flow near the surface of a hypersonic vehicle can be augmented by seeding the flow with alkali metals. This in turn would allow for better control of a hypersonic vehicle via magnetohydrodynamics (MHD).[57, 58] Additionally, hypersonic and atmospheric reentry vehicles have a fair amount of alkali metal impurities in the vehicle surface. During the course of hypersonic flight or atmospheric reentry a significant amount of these impurities are inevitably vaporized and ionized in the flow.[57-63] Alkali cations play a significant role in the formation of the plasma near the vehicle's boundary termed the plasma sheath. The plasma sheath leads to many adverse changes in the vehicle's communication and navigation capabilities such as loss of telemetry, GPS, and radio "blackout".[64, 65] Also, the plasma sheath can lead to significant effects in the vehicle's aerodynamic performance, stability, and thermal protection system.[63, 66, 67] Developing a better understanding of the fundamental plasma chemistry involved in the recombination processes for alkali metal ions is of vital importance to hypersonic and plasma dynamic research.

Alkali metal cations generally have a low radiative recombination rate. Thus at higher pressures in atmospheric gases, such as those around a hypersonic vehicle, the plasma neutralizations is controlled primarily by three-body processes.[68] These processes include electron (e^- as the third body) and neutral stabilized collisions as well as chaperone mechanisms. The lack of knowledge of these processes is heavily due to the difficulty to make quantitative measurements of the recombination rates. Past measurements have involved techniques such as ion storage rings, stationary afterglow (SA), and flow afterglow (FA). The main drawbacks of these techniques come in the form of a limited range of experimental pressures and temperatures. Additionally, all of these techniques use ionization methods that lead to ions others than those that are desired, which naturally complicates the overall chemistry. Primarily, Penning ionization of Ar by a He microwave discharge is used in these apparatuses.

Coherent microwave Rayleigh scattering (Radar) from small volume plasmas generated by Resonance Enhanced Multiphoton Ionization (REMPI) is a highly selective technique that does not require the extraction of ionic species or electrons from the plasma. Radar REMPI has rapidly grown as a diagnostic technique since first implemented in 2006.[69, 70] This is due largely to the benefits of separating the optical plasma generation from the standoff microwave detection. This allows the Radar REMPI system to be simpler to implement and less sensitive to the external environment than fully optical techniques. REMPI is a non-linear optical process in which m photons are simultaneously absorbed leading to the electronic excitation of a target atomic or molecular species. This is followed by an n photon ionization of the electronically excited species. Thus, REMPI transitions are often denoted as an m+n photon process. Radar consist of microwave scattering from the electrons in the laser-induced REMPI plasma. When the size of the microwave wavelength is larger than the characteristic length of the plasma and the skin depth of the plasma is much larger than the characteristic length of the plasma, then the microwave scattering falls under the term coherent Rayleigh scattering. Under such conditions, Radar from a REMPI plasma may be treated as an oscillating point dipole. Such a scattering process is analogous to light scattering off of atoms or molecules.

Detection of trace species such as NO, CO, Xe, Ar in static gas mixtures[71] and CH_3 in a methane/air flame[72] via Radar REMPI has been demonstrated. Utilizing the decay of the Radar REMPI signal has been used for kinetic measurements. This has been demonstrated by electron loss rate measurements in air[73] and sodium-argon cluster ion recombination rates[74]. O_2 rotational temperature measurement via Radar REMPI has been used to measure gas[75], flame[76], and DC discharge[77] temperatures. Atomic oxygen concentration measurements in a flame were performed using Radar REMPI.[78]

The advent of stable microdischarges dates back to the work of White in the 1950s [79] and gained much attention in spatially confined cavities in the 1990's.[80, 81] Numerous applications, have been investigated. Microdischarge devices take advantage of the scaling of breakdown voltage with the product of pressure and gap distance (*pd*) as described by Paschen's Law.[82] Typically, to maintain the stability of "normal-glow" discharges at atmospheric pressure, the inter-electrode separation is confined to distances on the order of 1 mm or less.[83] This small spacing leads to the generation of a non-equilibrium or "cold" plasma discharge.

A striking property of these non-equilibrium plasmas is that the electron temperature, T_e, is often several orders of magnitude larger than the gas temperature, T_g.[83, 84] This excess electron energy can be channeled to drive specific optical or chemical processes at relatively low gas temperature, which opens microdischarges to the wide range of applications previously mentioned. Non-equilibrium plasma discharges in general have potential applications in plasma assisted combustion [85-87], flow control [86], biomedical research [88-90], manufacturing [91], arc jet flow heating [84], vacuum ultra-violet (VUV) light sources [92], and nanoparticle synthesis[93, 94]. Due to the diversity of the applications of non-equilibrium plasma discharges there are many experimental difficulties in implementing diagnostics. First, many non-equilibrium plasma discharge devices have small volumes and limited optical access. Wide ranges of pressures from vacuum to multiple atm and temperatures from room to several thousand kelvin.

Although tremendous progress has been made in the area of plasma diagnostics in microdischarges[84], many fundamental properties, such as temperature, are still not satisfactorily measured. A non-thermal plasma is described, not by a single temperature, but by a set of temperatures including electron temperature (T_{e}) relating to the kinetic energy distribution of the electrons, as well as several molecular temperatures, T_{trans}, T_{vib}, and T_{rot} relating to the translational, vibrational, and rotational energies of the molecules. Typically the temperature set in a non-thermal plasma will have the characteristic of $T_{\mathrm{e}} >> T_{\mathrm{vib}} > T_{\mathrm{trans}} = T_{\mathrm{rot},}$ where T_{trans} and T_{rot} are commonly identified as the gas temperature, T_{g}. The gas temperature in these non-thermal plasmas can range from near room temperature for monatomic gases such as argon to above 2000K in molecular gases such as air,[83, 95] and is highly dependent on discharge source parameters such as electrical current. The most widely published temperature diagnostic works involve determining rotational temperature by optical emission spectroscopy (OES) of the N_2 second positive system.[96-98] Unfortunately, the spatial and temporal resolutions achievable by these methods have stringent limitations. Additionally, OES is limited for certain species in microdischarges.[99] Another temperature measurement using Stark shifting analysis of the H_β transition involves hydrogen seeding, which complicates the overall plasma composition.[100] Cavity Ringdown spectroscopy is a line-of-sight temperature measurement which has limited spatial resolution.[99] Overall, the diagnostic tools available for microdischarge analysis in atmospheric air are scarce and restrict, in some way, what can be accurately derived from the experimental process.

Production of chemical intermediates such as radical and atomic species greatly influence many aspects of non-equilibrium plasma discharges and their nearby environment such as: kinetics, electron density, and thermochemistry. Primarily the two techniques used to determine radical and atomic species concentrations in discharge environments is tunable diode laser absorption spectroscopy (TDLAS) and two-photon absorption laser induced fluorescence (TALIF). TDLAS has been used to measure a wide range of radical species concentrations and kinetics for non-equilibrium plasma discharges in molecular gas mixtures [101-103]. The major limitation of TDLAS is that it is a line integrated technique so it cannot be used to probe species in inhomogeneous environments. TALIF has been used to measure atomic species such as: H, O, and N.[99, 104, 105] TALIF is not applicable to high pressure environments due to rapid collisional quenching of the excited states. Both fully optical techniques can be difficult to implement in “real” facilities such as arc jets.

The mechanisms for breakdown in gas discharges have been studied extensively for over a century.[106] It is well known that the voltage required to initiate breakdown of a gaseous DC discharge depends strongly on the pressure *P* multiplied by the distance *D* of the gap between the electrodes, *PD*, as described by Paschen’s Law.[82] For a gas at atmospheric pressure, by limiting the inter-electrode separation to a distance of less than a millimeter, it is possible to produce a stable “normal-glow” microdischarge.[83] Although such a microdischarge is spatially confined compared to a traditional low pressure discharge, the normal glow properties of a non-thermal discharge still apply, such as an electron temperature, T_e, which is several orders of magnitude larger than the gas temperature, T_g.[83, 84, 107] Many applications have been explored to exploit this excess electron energy and drive optical or chemical processes such as: vacuum-ultraviolet light sources[92], biomedical systems [89, 90], nanoparticle synthesis[93, 94], and plasma ignition[87]. However in atmospheric air, even with a small inter-electrode separation of less than 1 mm, a sizeable voltage (upwards of 4 to 5 kV) may still be required to initiate breakdown.

A significant reduction of the breakdown threshold within a microdischarge could be a breakthrough that enables numerous applications. Such a breakdown voltage reduction could allow for the use of smaller, cheaper, and safer power supplies. One method of reducing the voltage required to initiate breakdown is to generate seed electrons into the discharge region. Breakdown under these conditions is termed "under-voltage breakdown". Previously studied techniques for achieving under-voltage breakdown have included electron seeding by illumination of the cathode by ultraviolet (UV) light[108-110], resonance enhanced multi-photon ionization (REMPI) by UV pulsed lasers [111, 112], and the use of secondary electrodes or spark plugs[113]. The major limitation of these methods is that they all require a secondary energy source in order to produce the seed electrons which can increase the overall cost, complexity, and weight of the microdischarge system.

On the other hand, the effect of solid particle contamination, whether intentionally introduced or not, on the breakdown process in air gaps has been explored previously. Unwanted solid particle contaminants in commercial electrical systems can lead to arcing and failure of transmission lines and gas insulation systems. Sand and dust with particle sizes above several tens of microns were shown to initiate breakdown across gap lengths of several centimeters.[114, 115] The previous works concluded that the sand and dust particles in the inter-electrode gap played a negligible role in the volume processes during breakdown; however, the formation of a thin contaminant layer on the cathode enhanced secondary electron emission and significantly reduced the breakdown voltage in some circumstances. Other works have shown that larger (100s of microns to 100s mms) conductive particles in an inter-electrode air gap can play a significant role in reducing breakdown voltage, time-lag of impulses, and breakdown probability.[116-118] These previous works have concluded that the degree of influence that the solid particles have on the breakdown process depends on both the discharge properties, namely polarity and field uniformity, as well as properties of the particles such as conductivity, shape, size, concentration, and position relative to the electrodes.

In Chapter 1, microwave scattering theory is applied to measurements from transient small volume plasmas, such as laser sparks in air, to discover their evolution process in its full cycle.[55, 119] From these measurements, it has been hypothesized that the laser spark evolution process can be characterized by three unique phases. First, an initial rise in scattered radiation intensity is caused by avalanche ionization. This is followed by a decrease in intensity due to microwave shielding effects caused by the decrease of the skin layer thickness relative to the plasma's characteristic length. Finally, as the plasma volume beings to expand, fewer electrons are shielded resulting in an increase in intensity. The computational results presented validate the existence of these three distinct phases of laser spark evolution seen in experimentation.[55]

Chapter 2 presents a new quantitative definition of the threshold intensity for generating laser-induced breakdown in air. This threshold is based on the measurement of total electron number during the onset of the laser-induced breakdown process. The free electrons produced by laser-induced breakdown were quantitatively measured by dielectric-calibrated coherent microwave scattering. The electron generation and its temporal evolution were monitored after the laser onset.

Threshold measurements were taken in air at pressures ranging from atmospheric to 40 bar_g. These thresholds are compared to the qualitative observation and probability based criteria. Additionally, the effects of laser wavelength and pulse duration on the breakdown threshold were explored for the 1st, 2nd, and 3rd harmonics of a Nd:YAG laser (i.e., 1064 nm, 532 nm, and 355 nm) and pulse durations of 10 ns and 100 ps. The quantitative breakdown thresholds were confirmed that the breakdown threshold decreases with the increase of pressure and/or laser photon energy (shorter wavelength), which is consistent with the previous assessments.

Chapter 3 presents a demonstration of laser ignition (LI) of combustible gaseous mixtures with order-of-magnitude reduction in per-pulse energy can be achieved using a high-repetition-rate (HRR) nanosecond laser pulse train. The HRR pulses are generated from a Nd:YAG-based burst-mode laser (Quasimodo, Spectral Energies)[120]. The HRR (10-100 kHz) laser pulse train induces a weakly-ionized plasma typically within the first few pulses. The subsequent laser pulses enhance the plasma through energy deposition and leads to sustained ignition. Generally, this approach can be viewed as an extension of the dual pulse technique with the number of pulses easily changeable from a few to multiple of tens. The HRR LI approach increases the ignition probability of lean combustible mixtures in high-speed flows while maintaining low individual pulse energies.

In Chapter 4, coherent microwave Rayleigh scattering (Radar) from Resonance Enhanced Multi-Photon Ionization (REMPI) is utilized for the measurement of sodium ion neutral stabilized and cluster dissociative recombination rates. The separation of the ionization and detection mechanisms greatly simplifies the experimental procedure. Radar REMPI as a stationary technique allows for a wide range of experimental temperatures and pressures including those above atmospheric conditions.[119, 121-124] REMPI allows for selective ionization of the sodium and minimizes all other cation species generated in the plasma. Coherent microwave scattering from the electrons in the decaying plasma allows in-situ measurement throughout time without extracting electrons or cations. Recombination rates were then deduced using a least-squares Monte Carlo algorithm (LSM). Neutral stabilized recombination rates for sodium ions in argon and nitrogen buffer gases along with the dissociative recombination rates of sodium-argon and sodium-nitrogen cluster ions are presented. The current model does not take into account backwards reaction of cluster ion formation making the presented rates only at best a rough estimation.

In Chapter 5, Radar REMPI measurements of local O_2 rotational temperature within an atmospheric air microdischarge are presented. Radar REMPI has previously been demonstrated for local rotational temperature measurements of molecular oxygen in static cell[75] and flame[76] environments. These measurements are performed at eight axial locations between pin-to-pin electrodes; this allowed for an axial temperature distribution within the discharge region to be determined.

Chapter 6 presents relative atomic oxygen species concentration measurements in a low pressure O_2/He DC and pulsed discharge via Radar REMPI. A 2+1 REMPI scheme of atomic oxygen was utilized. The technique by which dielectric calibration can be used to obtain absolute concentration measurements is discussed. The influence of gas composition, laser pulse energy, and pressure on the measurement technique will be explored. It will be shown that for prescribed laser intensities direct measurement of atomic oxygen can be separated from photo-dissociation. Methodology for separating electrons generated via the REMPI process from those present in the DC and pulsed discharge will be presented.

Chapter 7 demonstrates how the seeding of metal nanoparticles can be utilized to reduce the voltage required to initiate breakdown in an air DC microdischarge. Reductions in the breakdown voltage were seen to be as high as 25% for a *PD* scaling of 40 Torr-cm for the seeding of iron and aluminum nanoparticles. High-speed chemiluminescence imaging of the discharge region revealed that the breakdown process was enhanced by a reduction in the required voltage from nanoparticle seeding, and then heating from the discharge can lead to ignition of some of the nanoparticles as they flowed through the discharge. The use of scanning electron microscopy (SEM) gave detailed information regarding the particle size, shape, and oxidation distributions of the metal nanoparticles. Further use of ex-situ diagnostic techniques, such as SEM analyses, could allow for the development of empirical correlations between particle characteristics and reduction in the breakdown voltage. Visual evidence of particle charging being the most likely mechanism for breakdown voltage reduction and subsequent reduction of the effective distance between the electrodes is been presented.

References

1. Nelson, P., et al., *Experimental and Theoretical Studies of Air Breakdown by Intense Pulse of Light.* Physics Letters, 1964. **13**(3): p. 226-228.

2. Buscher, H.T., Tomlinso.Rg, and E.K. Damon, *Frequency Dependence of Optically Induced Gas Breakdown.* Physical Review Letters, 1965. **15**(22): p. 847-&.

3. Kroll, N. and K.M. Watson, *Theoretical Study of Ionization of Air by Intense Laser Pulses.* Physical Review A, 1972. **5**(4): p. 1883-&.

4. Raizer, I.F.U.F.P., *Laser-induced discharge phenomena*. Studies in Soviet science : Physical sciences. 1977, New York: Consultants Bureau. xiv, 366 p.

5. Demichel.C, *Laser Induced Gas Breakdown - a Bibliographical Review.* Ieee Journal of Quantum Electronics, 1969. **Qe 5**(4): p. 188-&.

6. Yan, H., et al., *Laser energy deposition in quiescent air.* Aiaa Journal, 2003. **41**(10): p. 1988-1995.

7. Yan, H., et al., *Effect of energy addition on MR -> RR transition.* Shock Waves, 2003. **13**(2): p. 113-121.

8. Loir, A.S., et al., Study of plasma expansion induced by femtosecond pulsed laser ablation and deposition of diamond-like carbon films. Applied Surface Science, 2003. **208**: p. 553-560.

9. Goto, T., High-speed deposition of zirconia films by laser-induced plasma CVD. Solid State Ionics, 2004. **172**(1-4): p. 225-229.

10. Vestin, F., M. Randelius, and A. Bengtson, *Laser-induced breakdown spectroscopy applied on low-alloyed zinc samples.* Spectrochimica Acta Part B-Atomic Spectroscopy, 2010. **65**(8): p. 721-726.

11. Salle, B., P. Mauchien, and S. Maurice, *Laser-Induced Breakdown Spectroscopy in open-path configuration for the analysis of distant objects.* Spectrochimica Acta Part B-Atomic Spectroscopy, 2007. **62**(8): p. 739-768.

12. Samek, O., et al., Application of laser-induced breakdown spectroscopy to in situ analysis of liquid samples. Optical Engineering, 2000. **39**(8): p. 2248-2262.

13. Adamson, M., et al., Laser-induced breakdown spectroscopy at a water/gas interface: A study of bath gas-dependent molecular species. Spectrochimica Acta Part B-Atomic Spectroscopy, 2007. **62**(12): p. 1348-1360.

14. McNaghten, E.D., et al., Detection of trace concentrations of helium and argon in gas mixtures by laser-induced breakdown spectroscopy. Spectrochimica Acta Part B-Atomic Spectroscopy, 2009. **64**(10): p. 1111-1118.

15. Phuoc, T.X., Laser spark ignition: experimental determination of laser-induced breakdown thresholds of combustion gases. Optics Communications, 2000. **175**(4-6): p. 419-423.

16. Phuoc, T.X., *Laser-induced spark ignition fundamental and applications.* Optics and Lasers in Engineering, 2006. **44**(5): p. 351-397.

17. Morgan, C.G., *Laser-Induced Breakdown of Gases.* Reports on Progress in Physics, 1975. **38**(5): p. 621-&.

18. Tambay, R. and R.K. Thareja, *LASER-INDUCED BREAKDOWN STUDIES OF LABORATORY AIR AT 0.266, 0.355, 0.532, AND 1.06 MU-M.* Journal of Applied Physics, 1991. **70**(5): p. 2890-2892.

19. Tambay, R., et al., *Laser-Induced Air Breakdown Using 0.355, 0.532, and 1.06 Mu-M Radiation.* Pramana-Journal of Physics, 1991. **37**(2): p. 163-166.

20. Thiyagarajan, M. and J.E. Scharer, *Experimental Investigation of 193-nm Laser Breakdown in Air.* Ieee Transactions on Plasma Science, 2008. **36**(5): p. 2512-2521.

21. Wang, C.C. and L.I. Davis, New Observations of Dielectric Breakdown in Air Induced by a Focused Nd3+-Glass Laser with Various Pulse Widths. Physical Review Letters, 1971. **26**(14): p. 822-&.

22. Williams, W.E., M.J. Soileau, and E.W. Vanstryland, *Picosecond Air Breakdown Studies at 0.53-Mu-M.* Applied Physics Letters, 1983. **43**(4): p. 352-354.

23. Ireland, C.L.M., et al., *Focal-Length Dependence of Air Breakdown by a 20-Psec Laser Pulse.* Applied Physics Letters, 1974. **24**(4): p. 175-177.

24. Thiyagarajan, M. and S. Thompson, *Optical breakdown threshold investigation of 1064 nm laser induced air plasmas.* Journal of Applied Physics, 2012. **111**(7).

25. Hummelt, J.S. and J.E. Scharer, Excitational energy transfer enhancing ionization and spatial-temporal evolution of air breakdown with UV laser radiation. Journal of Applied Physics, 2010. **108**(9).

26. Sturm, V. and R. Noll, Laser-induced breakdown spectroscopy of gas mixtures of air, CO2, N-2, and C3H8 for simultaneous C, H, O, and N measurement. Applied Optics, 2003. **42**(30): p. 6221-6225.

27. Way, J., J. Hummelt, and J. Scharer, Experimental measurements of multiphoton enhanced air breakdown by a subthreshold intensity excimer laser. Journal of Applied Physics, 2009. **106**(8).

28. Sobral, H., et al., Temporal evolution of the shock wave and hot core air in laser induced plasma. Applied Physics Letters, 2000. **77**(20): p. 3158-3160.

29. Diwakar, P.K. and D.W. Hahn, Study of early laser-induced plasma dynamics: Transient electron density gradients via Thomson scattering and Stark Broadening, and the implications on

laser-induced breakdown spectroscopy measurements. Spectrochimica Acta Part B-Atomic Spectroscopy, 2008. **63**(10): p. 1038-1046.

30. Dzierzega, K., et al., *Thomson scattering from laser induced plasma in air.* 14th International Symposium on Laser-Aided Plasma Diagnostics (Lapd14), 2010. **227**.

31. Yalin, A.P., et al., Laser plasma formation assisted by ultraviolet pre-ionization. Physics of Plasmas, 2014. **21**(10).

32. Boker, D. and D. Bruggemann, *Temperature measurements in a decaying laser-induced plasma in air at elevated pressures.* Spectrochimica Acta Part B-Atomic Spectroscopy, 2011. **66**(1): p. 28-38.

33. El-Rabii, H., S.B. Victorov, and A.P. Yalin, *Properties of an air plasma generated by ultraviolet nanosecond laser pulses.* Journal of Physics D-Applied Physics, 2009. **42**(7).

34. Ghorui, S., J.V.R. Heberlein, and E. Pfender, *Thermodynamic and transport properties of two-temperature nitrogen-oxygen plasma.* Plasma Chemistry and Plasma Processing, 2008. **28**(4): p. 553-582.

35. Bradley, D., et al., *Fundamentals of high-energy spark ignition with lasers.* Combustion and Flame, 2004. **138**(1): p. 55-77.

36. Tauer, J., H. Kofler, and E. Wintner, *Laser-initiated ignition.* Laser & Photonics Reviews, 2010. **4**(1): p. 99-122.

37. Dearden, G. and T. Shenton, *Laser ignited engines: progress, challenges and prospects.* Optics express, 2013. **21**(106): p. A1113-A1125.

38. Ronney, P.D., *Laser versus conventional ignition of flames.* Optical Engineering, 1994. **33**(2): p. 510-521.

39. Dale, J., P. Smy, and R. Clements, *Laser ignited internal combustion engine-an experimental study*. 1978, SAE Technical Paper.

40. Osborne, R.J., et al., ‘Evaluation and Characterization Study of Dual Pulse Laser-Induced Spark (DPLIS) for Rocket Engine Ignition System Application. Powered Flight- The Next Century, 2003.

41. Hurricane, O., et al., Fuel gain exceeding unity in an inertially confined fusion implosion. Nature, 2014. **506**(7488): p. 343-348.

42. Oldenborg, R., J. Early, and C. Lester, *Advanced ignition and propulsion technology program*. 1998, Los Alamos National Lab., NM (US).

43. Kopecek, H., et al., Laser-induced ignition of methane-air mixtures at pressures up to 4 MPa. Laser physics, 2003. **13**(11): p. 1365-1369.

44. El-Rabii, H., et al., *Laser spark ignition of two-phase monodisperse mixtures.* Optics communications, 2005. **256**(4): p. 495-506.

45. Weinrotter, M., et al., *Laser ignition of ultra-lean methane/hydrogen/air mixtures at high temperature and pressure.* Experimental Thermal and Fluid Science, 2005. **29**(5): p. 569-577.

46. Yalin, A.P., *High power fiber delivery for laser ignition applications.* Optics express, 2013. **21**(106): p. A1102-A1112.

47. El-Rabii, H. and G. Gaborel, *Laser ignition of flammable mixtures via a solid core optical fiber.* Applied Physics B, 2007. **87**(1): p. 139-144.

48. Mullett, J., et al., *A comparative study of optical fibre types for application in a laser-induced ignition system.* Journal of Optics A: Pure and Applied Optics, 2009. **11**(5): p. 054007.

49. Joshi, S., N. Wilvert, and A.P. Yalin, *Delivery of high intensity beams with large clad step-index fibers for engine ignition.* Applied Physics B, 2012. **108**(4): p. 925-932.

50. Joshi, S., A.P. Yalin, and A. Galvanauskas, Use of hollow core fibers, fiber lasers, and photonic crystal fibers for spark delivery and laser ignition in gases. Applied optics, 2007. **46**(19): p. 4057-4064.

51. Beaudou, B., et al., Millijoule laser pulse delivery for spark ignition through kagome hollow-core fiber. Optics letters, 2012. **37**(9): p. 1430-1432.

52. Dumitrache, C., J. Rath, and A.P. Yalin, *High power spark delivery system using hollow core kagome lattice fibers.* Materials, 2014. **7**(8): p. 5700-5710.

53. Hsu, P.S., et al., Investigation of optical fibers for coherent anti-Stokes Raman scattering (CARS) spectroscopy in reacting flows. Experiments in fluids, 2010. **49**(4): p. 969-984.

54. Cheng, H., et al. Multiple Pulse Laser Ignition Control Application in GDI Lean Combustion. in Laser Ignition Conference. 2015. Optical Society of America.

55. Zhang, Z.L., M.N. Shneider, and R.B. Miles, *Microwave diagnostics of laser-induced avalanche ionization in air.* Journal of Applied Physics, 2006. **100**(7).

56. Larsson, M. and A.E. Orel, *Dissociative Recombination of Moleculear Ions*. 2008, Cambridge UK: Cambridge University Press.

57. Bisek, N.J. and J. Poggie, Exploration of MHD Flow Control for a Hypersonic Blunt Elliptic Cone with an Impregnated Ablator, in 49th AIAA Aerospace Sciences Meeting including the New Horizons Forum and Aerospace Exposition. 2011, AIAA: Orlando FL.

58. Macheret, S.O., M.N. Shneider, and G. Candler, Modeling of MHD Power Generation on Board Reentry Vehicles, in 42nd AIAA Aerospace Sciences Meeting and Exhibit. 2004, AIAA: Reno, NV. p. AIAA-2004-1024.

59. Miner, E.W. and C.H. Lewis, *Hypersonic Ionizing Air Viscous Shock-Layer Flows over Sphere Cones.* Aiaa Journal, 1975. **13**(1): p. 80-88.

60. Macheret, S.O., Weakly Ionized Plasmas in Hypersonics: Fundamental Kinetics and Flight Applications, in AIP Conference Proceedings. 2005. p. 1197-1210.

61. Shneider, M.N. and S.O. Macheret, Hypersonic Aerodynamic Control and Thrust Vectoring by Nonequilibrium Cold-Air MHD Devices, in 43rd AIAA Aerospace Sciences Meeting and Exhibit. 2005, AIAA: Reno, NV. p. AIAA-2005-979.

62. Boyd, I.D., Modeling of associative ionization reactions in hypersonic rarefied flows. Physics of Fluids, 2007. **19**(9): p. 096102.

63. Ozawa, T., J.Q. Zhong, and D.A. Levin, Development of kinetic-based energy exchange models for noncontinuum, ionized hypersonic flows. Physics of Fluids, 2008. **20**(4): p. 046102.

64. Starkey, R.P., Electromagnetic Wave/Magnetoactive Plasma Sheath Interaction for Hypersonic Vehicle Telemetry Blackout Analysis, in AIAA. 2003. p. AIAA2003-4167.

65. Gillman, E.D., J.E. Foster, and I.M. Blankson, Review of Leading Approaches for Mitigating Hypersonic Vehicle Communications Blackout and a Method of Ceramic Particulate Injection Via Cathode Spot Arcs for Blackout Mitigation, in Report. 2010, NASA Glenn Research Center: Cleveland, Ohio.

66. Johnson, J.E., R.P. Starkey, and M.J. Lewis, *Aerodynamic Stability of Reentry Heat Shield Shapes for a Crew Exploration Vehicle.* Journal of Spacecraft and Rockets, 2006. **43**(4): p. 721-730.

67. Zhong, J.Q., T. Ozawa, and D.A. Levin, *Modeling of Stardust Reentry Ablation Flows in the Near-Continuum Flight Regime* AIAA Journal, 2008. **46**(10): p. 2568-2581.

68. Zhaunerchyk, V., et al., *Dissociative recombination study of Na+(D2O) in a storage ring.* The Journal of Chemical Physics, 2004. **121**(21): p. 10483-10488.

69. Zhang, Z., M.N. Shneider, and R.B. Miles, *Coherent Microwave Rayleigh Scattering from Resonance-Enhanced Multiphoton Ionization in Argon.* Physical Review Letters, 2007. **98**(26): p. 265005.

70. Shneider, M.N., Z. Zhang, and R.B. Miles, *Plasma induced by resonance enhanced multiphoton ionization in inert gas.* Journal of Applied Physics, 2007. **102**(12): p. 123103.

71. Dogariu, A. and R.B. Miles, Detecting localized trace species in air using radar resonance-enhanced multi-photon ionization. Applied Optics, 2011. **50**(4): p. A68-A73.

72. Wu, Y., et al., Direct measurement of methyl radicals in a methane/air flame at atmospheric pressure by radar REMPI. Optics Express, 2011. **19**(24): p. 23997-24004.

73. Dogariu, A., M.N. Shneider, and R.B. Miles, *Versatile radar measurement of the electron loss rate in air.* Applied Physics Letters, 2013. **103**(22): p. 224102.

74. Wu, Y., et al., Measurement of sodium-argon cluster ion recombination by coherent microwave scattering. Applied Physics Letters, 2012. **100**(11): p. 114108.

75. Wu, Y., Z. Zhang, and S.F. Adams, *O2 rotational temperature measurements by coherent microwave scattering from REMPI.* Chemical Physics Letters, 2011. **513**(4–6): p. 191-194.

76. Wu, Y., et al., Flame temperature measurements by radar resonance-enhanced multiphoton ionization of molecular oxygen. Appl. Opt., 2012. **51**(28): p. 6864-6869.

77. Sawyer, J., et al., O2 rotational temperature measurements in an atmospheric air microdischarge by radar resonance-enhanced multiphoton ionization. Journal of Applied Physics, 2013. **113**(23): p. 233304.

78. Tat Loon, C. and M. Richard, Absolute concentration measurements of atomic oxygen in a flame using radar REMPI, in 52nd Aerospace Sciences Meeting. 2014, American Institute of Aeronautics and Astronautics.

79. White, A.D., *New Hollow Cathode Glow Discharge.* Journal of Applied Physics, 1959. **30**(5): p. 711-719.

80. Schoenbach, K.H., et al., *Microhollow cathode discharges.* Applied Physics Letters, 1996. **68**(1): p. 13-15.

81. Iza, F., et al., *Microplasmas: Sources, Particle Kinetics, and Biomedical Applications.* Plasma Processes and Polymers, 2008. **5**(4): p. 322-344.

82. Paschen, F., Ueber die zum Funkenübergang in Luft, Wasserstoff und Kohlensäure bei verschiedenen Drucken erforderliche Potentialdifferenz. Annalen der Physik, 1889. **273**(5): p. 69-96.

83. Foest, R., M. Schmidt, and K. Becker, *Microplasmas, an emerging field of low-temperature plasma science and technology.* International Journal of Mass Spectrometry, 2006. **248**(3): p. 87-102.

84. Laux, C.O., et al., *Optical diagnostics of atmospheric pressure air plasmas.* Plasma Sources Science and Technology, 2003. **12**(2): p. 125.

85. Sun, W., Non-equilibrium Plasma-Assisted Combustion. 2013.

86. Adamovich, I.V., et al., *Plasma assisted ignition and high-speed flow control: non-thermal and thermal effects.* Plasma Sources Science and Technology, 2009. **18**(3): p. 034018.

87. Pancheshnyi, S.V., et al., *Ignition of Propane–Air Mixtures by a Repetitively Pulsed Nanosecond Discharge.* Plasma Science, IEEE Transactions on, 2006. **34**(6): p. 2478-2487.

88. Lu, X., M. Laroussi, and V. Puech, *On atmospheric-pressure non-equilibrium plasma jets and plasma bullets.* Plasma Sources Science and Technology, 2012. **21**(3): p. 034005.

89. Goree, J., et al., *Killing of S. mutans Bacteria Using a Plasma Needle at Atmospheric Pressure.* Plasma Science, IEEE Transactions on, 2006. **34**(4): p. 1317-1324.

90. Kim, J.Y., et al., 15-μm-sized single-cellular-level and cell-manipulatable microplasma jet in cancer therapies. Biosensors and Bioelectronics, 2010. **26**(2): p. 555-559.

91. Babayan, S.E., et al., Deposition of silicon dioxide films with a non-equilibrium atmospheric-pressure plasma jet. Plasma Sources Science and Technology, 2001. **10**(4): p. 573.

92. Ren'an, B., et al., *Development of 146nm Vacuum UV Light Source.* Physics Procedia, 2012. **32**(0): p. 477-481.

93. Chiang, W.-H. and R.M. Sankaran, Microplasma synthesis of metal nanoparticles for gas-phase studies of catalyzed carbon nanotube growth. Applied Physics Letters, 2007. **91**(12): p. 121503-3.

94. Richmonds, C. and R.M. Sankaran, Plasma-liquid electrochemistry: Rapid synthesis of colloidal metal nanoparticles by microplasma reduction of aqueous cations. Applied Physics Letters, 2008. **93**(13): p. 131501-3.

95. Becker, K.H., K.H. Schoenbach, and J.G. Eden, *Microplasmas and applications.* Journal of Physics D: Applied Physics, 2006. **39**(3): p. R55.

96. Goyette, A.N., et al., Experimental comparison of rotational and gas kinetic temperatures in N2 and He-N2 discharges Journal of Physics D: Applied Physics, 1998. **31**(13): p. 1556.

97. Nassar, H., et al., N 2 + /N 2 ratio and temperature measurements based on the first negative N 2 + and second positive N 2 overlapped molecular emission spectra. Journal of Physics D: Applied Physics, 2004. **37**(14): p. 1904.

98. Staack, D., et al., Spatially Resolved Temperature Measurements of Atmospheric-Pressure Normal Glow Microplasmas in Air. Plasma Science, IEEE Transactions on, 2007. **35**(5): p. 1448-1455.

99. Stancu, G.D., et al., *Atmospheric pressure plasma diagnostics by OES, CRDS and TALIF*. Journal of Physics D: Applied Physics, 2010. **43**(12): p. 124002.

100. Xi-Ming, Z., C. Wen-Cong, and P. Yi-Kang, *Gas temperature, electron density and electron temperature measurement in a microwave excited microplasma.* Journal of Physics D: Applied Physics, 2008. **41**(10): p. 105212.

101. Lombardi, G., et al., Quantitative detection of methyl radicals in non-equilibrium plasmas: a comparative study. Plasma Sources Science and Technology, 2004. **13**(1): p. 27.

102. Pipa, A.V., et al., Absolute production rate measurements of nitric oxide by an atmospheric pressure plasma jet (APPJ). Journal of Physics D: Applied Physics, 2008. **41**(19): p. 194011.

103. Welzel, S., et al., *Kinetic and Diagnostic Studies of Molecular Plasmas Using Laser Absorption Techniques.* Journal of Physics: Conference Series, 2007. **86**(1): p. 012012.

104. Schmidt, J.B., Ultrashort Two-Photon-Absorption Laser-Induced Fluorescence in Nanosecond-Duration, Repetitively Pulsed Discharges. 2015, The Ohio State University.

105. Sun, W., et al., Kinetic effects of non-equilibrium plasma-assisted methane oxidation on diffusion flame extinction limits. Combustion and Flame, 2012. **159**(1): p. 221-229.

106. Townsend, J., *Electricity in gases*. 1915, Oxford,: Clarendon Press. xv, 406 p. incl. tables, diagrs.

107. Sawyer, J., et al., O2 rotational temperature measurements in an atmospheric air microdischarge by radar resonance-enhanced multiphoton ionization. Journal of Applied Physics, 2013. **113**(23): p. -.

108. Frechette, M.F., N. Bouchelouh, and R.Y. Larocque. Laser-induced undervoltage breakdown in atmospheric N₂ correlated with time-resolved avalanches. in Electrical Insulation, 1994., Conference Record of the 1994 IEEE International Symposium on. 1994.

109. Kluckow, R., Über den zeitlichen Verlauf des Stromes einer Gasentladung in Wasserstoff. Zeitschrift für Physik, 1961. **161**(4): p. 353-369.

110. Varney, R.N., Liberation of Electrons by Positive-Ion Impact on the Cathode of a Pulsed Townsend Discharge Tube. Physical Review, 1954. **93**(6): p. 1156-1160.

111. Cooley, J.E. and E.Y. Choueiri, *Threshold criteria for undervoltage breakdown.* Journal of Applied Physics, 2008. **103**(9): p. -.

112. Cooley, J.E., Fundamentals of undervoltage breakdown through the Townsend mechanism. 2008.

113. Hong, T. and V. Scuka, *The breakdown mechanism of a mid-plane triggered spark gap trigatron.* Dielectrics and Electrical Insulation, IEEE Transactions on, 1996. **3**(6): p. 843-848.

114. Al-Arainy, A.A. The influence of dust particles on the DC breakdown voltage of rod-rod air gaps. in Electrical Insulating Materials, 1995. International Symposium on. 1995.

115. Al-Arainy, A.A., N.H. Malik, and M.I. Qureshi, *Influence of sand/dust contamination on the breakdown of asymmetrical air gaps under lightning impulses.* Electrical Insulation, IEEE Transactions on, 1992. **27**(2): p. 193-206.

116. Kubuki, M., et al., *Estimation of dc breakdown mechanisms in air gaps containing floating metallic particles.* Dielectrics and Electrical Insulation, IEEE Transactions on, 1997. **4**(1): p. 92-101.

117. Hara, M. and M. Akazaki, A method for prediction of gaseous discharge threshold voltage in the presence of a conducting particle. Journal of Electrostatics, 1977. **2**(3): p. 223-239.

118. Hara, M., et al., *Particle-triggered pre-breakdown phenomena in atmospheric air gap under AC voltage.* Dielectrics and Electrical Insulation, IEEE Transactions on, 2005. **12**(5): p. 1071-1081.

119. Shneider, M.N. and R.B. Miles, *Microwave diagnostics of small plasma objects.* Journal of Applied Physics, 2005. **98**(3).

120. Slipchenko, M.N., et al., *Quasi-continuous burst-mode laser for high-speed planar imaging.* Optics letters, 2012. **37**(8): p. 1346-1348.

121. Shneider, M.N., Z. Zhang, and R.B. Miles, Simultaneous resonant enhanced multiphoton ionization and electron avalanche ionization in gas mixtures. Journal of Applied Physics, 2008. **104**(2): p. 9.

122. Miles, R.B., et al., Microwave scattering from laser ionized molecules: A new approach to nonintrusive diagnostics. AIAA Journal, 2007. **45**(3): p. 513-515.

123. Zhang, Z. and M.N. Shneider, Measurement of plasma decay processes in mixture of sodium and argon by coherent microwave scattering. Physics of Plasmas, 2010. **17**(1).

124. Wu, Y., et al., Measurement of sodium-argon cluster ion recombination by coherent microwave scattering. Applied Physics Letters, 2012. **100**(11): p. -.

CHAPTER I

MICROWAVE SCATTERING FROM LASER SPARK IN AIR

This article, “Microwave Scattering from Laser Spark in Air”, was received on the 29th of May 2012, accepted on the 9th of August 2012, and published on the 17th of September 2012.

Author affiliations:

Jordan Sawyer[1], Zhili Zhang[1], Mikhail N. Shneider[2]

[1]Mechanical, Aerospace and Biomedical Engineering, University of Tennessee, Knoxville Tennessee 37996, USA

[2]Mechanical and Aerospace Engineering, Princeton University, Princeton, New Jersey 08544, USA

Sawyer, J., Z. Zhang, and M.N. Shneider, *Microwave scattering from laser spark in air.* Journal of Applied Physics, 2012. 112(6): p. 063101.

Abstract

In this chapter, microwave Mie scattering from a laser-induced plasma in atmospheric air is computed. It shows that the scattered microwave transitions from coherent Rayleigh scattering to Mie scattering based on the relative transparency of the laser-induced plasma at the microwave frequency. The microwave penetration in the plasma alters from total transparency to partial shielding due to the sharp increase of the electron number density within the avalanche ionization phase. The transition from Rayleigh scattering to Mie scattering is verified by both the temporal evolution of the scattered microwave and the homogeneity of polar scattering plots.

Introduction

Since the 1960s laser spark generation or laser breakdown has been studied extensively.[1, 2] It has been widely used in experiments involving energy deposition, material processing, diagnostics, and combustion etc. Energy deposition via laser-induced plasmas as a method of flow control has also been explored.[3, 4] In material processing, laser-induced plasmas have been used for thin film depositions.[5, 6] Laser Induced Breakdown Spectroscopy (LIBS) is a diagnostic technique that has been utilized in determining material compositions in the solid, liquid, and gaseous phases.[7-11] Laser-induced spark ignition has been shown to have many advantages over traditional combustion systems.[12, 13]

Even with years of extensive research, the evolution of laser sparks in air is still lacking key details, such as electron number density. Primarily, optical diagnostic techniques, such as optical emission spectroscopy and stark shifting, have been applied to laser sparks in air to determine plasma, thermodynamic, and transport properties.[14-16] Unfortunately, the limitations of achievable temporal and spatial resolutions of these methods make it difficult to study the avalanche ionization phase in the spark. Traditional microwave measurement methods, such as absorption and interferometry, are not effective due to the small dimensions of the plasma relative to the microwave wavelength.

Microwave scattering measurements have been applied to transient small volume plasmas, such as laser sparks in air, to discover their evolution process in its full cycle.[17] [18] From these measurements, it has been hypothesized that the laser spark evolution process can be characterized by three unique phases. First, an initial rise in scattered radiation intensity is caused by avalanche ionization. This is followed by a decrease in intensity due to microwave shielding effects caused by the decrease of the skin layer thickness relative to the plasma's characteristic length. Finally, as the plasma volume beings to expand, fewer electrons are shielded resulting in an increase in intensity. Additionally coherent microwave scattering measurements (Radar) have been combined with Resonance Enhanced Multi-Photon Ionization (REMPI) to determine species concentrations and rotational temperatures in flames.[19, 20]

In this chapter, microwave scattering theory will first be introduced along with plasma evolution modeling. The computational results presented here validate the existence of three distinct phases of laser spark evolution seen in experimentation.[18]

Theory

Microwave Scattering from a Small-volume Plasma

The laser-induced plasma is initially a small sphere, which is on the order of tens of microns and located near the laser focus. This is much smaller than the wavelength of the incident microwave (a few centimeters). The scattered microwave radiation from the plasma can be characterized by either the Rayleigh or the Mie scattering regime. The determination of the scattering regimes depends upon the plasma transparency condition of $\delta > V_0^{1/3}$, where the skin layer thickness of δ is found from $\delta = \frac{2}{\sqrt{2\mu_0\sigma_\omega\omega}}$, the plasma conductivity at the microwave frequency ω is σ_ω, and plasma volume is V_0, respectively. Assuming a spherical geometry for the laser induced plasma, the plasma transparency condition can be described by $\delta > a$, where a is the sphere's radius.

If the plasma transparency criterion is satisfied, the scattering can be described by the Rayleigh approximation in the far field. The distance between the microwave receiver horn and the plasma, R, is significantly larger than the microwave wavelength. The incident microwave causes a modulating charge separation leading to an oscillating induced point dipole. The re-radiation from the point dipole forms the scattered microwave signal and exists in the Rayleigh regime. Microwave scattering in the Rayleigh regime is both coherent and isotropic, which makes it diagnostically favorable because the electric field of the scattered signal is linearly proportional to the total electron number inside the plasma.

However, if the plasma transparency criterion is not met, the scattering effect is described by general Mie scattering. In this regime, the plasma can no longer be taken to be an induced point dipole so that the electric field of the scattered microwave is not directly proportional to the total electron number of the plasma. Additionally, the skin layer thickness is smaller than the characteristic size of the plasma which causes some of the electrons to be shielded from the incident microwave radiation. This shielding causes the scattered signal to have a reduction in its electric field and be anisotropic in nature.

In a general, microwave scattering can be described by the Mie solution in both the Rayleigh and Mie regimes.[21] In the Mie solution, the plasma conductivity at the microwave frequency and electric permittivity are given as

$$\sigma_\omega = \frac{e^2 n_e \nu_{eff}}{m_e\left(\omega^2+\nu_{eff}^2\right)} \qquad (1)$$

$$\epsilon = 1 - \frac{e^2 n_e}{\epsilon_0 m_e\left(\omega^2+\nu_{eff}^2\right)} \qquad (2)$$

where e is the electron's charge, m_e is the mass of an electron, n_e is the electron number density inside the plasma, and the effective plasma collisional frequency of ν_{eff}, is the sum of the electron neutral and electron-ion (Coulomb) momentum exchange collisional frequencies; ε_0 is the vacuum permittivity.

A depiction of microwave scattering in the Mie regime from a small-volume plasma can be seen in Figure 1. The electric field of the incident microwave source propagates along the x-axis and oscillates along the z-axis while the laser producing the plasma propagates along the y-axis. The spherical coordinates R, θ, and Φ are used to describe the position of the microwave receiver horn with respect to the plasma. As can be seen in Figure 1, the electrons inside the skin layer thickness

, δ, oscillate in phase and reradiate due to scattering of the incident microwave radiation, I_0. The scattered signal is a function of both angular coordinates and time. Beyond the skin layer thickness, electrons are shielded from the incident microwave radiation and remain unaffected.

The first phase of the plasma evolution process occurs in the Rayleigh regime. A time delay is seen until the total electron number reaches a threshold detectable by the microwave system. Following the time delay, the scattering intensity is then proportional to the square of the total electron number during the initial avalanche ionization phase and the collisional frequency can be estimated by the electron neutral collisional frequency. The intensity of the scattered radiation continually rises until a peak value is reached and then begins to decreases. This is the start of the second phase which occurs in the Mie regime. In this phase microwave shielding effects act to reduce the intensity of the scattered signal making it no longer proportional to the total electron number squared. Also, collisions due to Coulomb forces begin to play an increasingly important role in the collisional frequency of the plasma as time progresses.

Additionally, with increasing conductivity, the field in the laser plasma is attenuated due to polarization screening as given by

$$E \approx E_0 / \sqrt{\left[1+\left(q\frac{\sigma_\omega}{\varepsilon_0\omega}\right)^2\right]}, \qquad (3)$$

where E_0 is the amplitude of the incident field; q is the geometric factor (for the assumed spherical shape of the laser plasma, q = 1/3). Polarization screening also reduces the intensity of the scattered signal and is automatically taken into account by the Mie solution.[22]

Plasma Dynamic Modeling

In the optical breakdown calculation, several approximations were made. The initial non-equilibrium stage of avalanche ionization was neglected. The conditions for local thermodynamic equilibrium (LTE) were assumed valid during the whole process of the optical breakdown development, as done in the previous work.[23] The calculations were carried out using the same approximations as the simulation of a pulsed arc in air.[24-26] The heat source is approximated by the formulas

$$P(r,t) = \frac{3P_L(t)}{4\pi r_0^3}\exp\left(-\frac{r^2}{r_0^2}\right); \quad Q_L = \int_0^{\infty} P_L(t)dt \quad . \qquad (4)$$

where $P_L(t)$ and Q_L are the instantaneous power and total energy of the laser pulse which is dissipated in the gas via the heating, dissociation, ionization and radiation losses of the plasma. This absorbed energy is usually about 1-10% of the total energy of the laser pulse. The simulations were conducted for cases of absorbed energies of 100, 200, and 400 µJ.

One dimensional gas dynamics equations were solved in a spherical Lagrange coordinate system using the Brode algorithm.[27] The equation of state took into account neutral and dissociated molecules, electrons, and ions both single and double ionized. The total number of particles and the local instantaneous molar fractions of neutral and ion molar components were computed in the LTE approximation using Plooster's algorithm.[24] Energy loss by radiation was taken into account in the approximation of radiant heat transfer as in the prior model.[26] The instantaneous local values of the electron number density $n_e(r,t)$ were determined in the ideal gas approximation for known local instantaneous pressure $p(r,t)$ and the local instantaneous single and double ion molar fractions. The instantaneous electron number density $n_e(t)$ was averaged over a spherical volume with a radius of *a* equal to the effective radius of the laser beam: $n_e(t) = \langle n_e(r,t) \rangle_{r=a}$. The average $n_e(t)$ was used in the calculation of microwave scattering by Mie theory.

Results and Discussion

Figure 2 shows the average electron number density, $n_e(t)$, of the simulated laser induced plasma for absorbed laser energies of 100, 200, and 400 µJ versus time. It is apparent that in the early time frame, approximately the first 10 to 15 ns, there is a very rapid increase in electron number density due to avalanche ionization. Following the end of the laser pulse, the electron number density begins to quickly decrease. If the laser induced plasma existed entirely in the Rayleigh regime during its lifetime, the scattering intensity would follow a similar trend.

However, Figure 3 shows the normalized microwave signal, via the Mie solution, from the simulated laser induced plasma for all three absorbed energy cases throughout time. All presented computed results correspond to the assumed microwave frequency $f = \omega / 2\pi = 12$ GHz, as in experiments.[18] There are essentially three distinct regions that characterize the scattered radiation intensity throughout time after the initial zero signal response. The initial zero signal response is due to the fact that the total electron number has not yet reached the minimum detectable threshold of the microwave system. This time delay is obviously dependent on the absorbed laser energy which causes the 400 µJ case to be the first to reach the threshold. The first phase is the avalanche ionization which causes a rapid increase in the total electron number. This in turn causes a swift increase in microwave signal response. The second phase begins when the signal reaches a peak value prior to reaching a maximum total electron number. The intensity then begins to decreases due to microwave shielding effects from the skin layer thickness. Interestingly, the intensity of the scattered microwave radiation is, in fact, higher in the 100 µJ than in the 400 µJ case. This is because the larger skin layer thickness in the 100 µJ case leads to the shielding of significantly fewer electrons from the incident microwave radiation. Finally, in later time frames, as the plasma volume begins to expand the signal increases due to a reduction in the fraction of shielded electrons.

The ratio of skin layer thickness to plasma radius of the simulated laser induced plasma and the normalized laser intensity profile throughout time can be seen in Figure 4. Skin layer thickness was calculated from $\delta = \frac{2}{\sqrt{2\mu_0\sigma_\omega\omega}} = \frac{1}{\sqrt{\pi\mu_0\sigma_\omega f}} = \frac{2}{2\sqrt{2\mu_0\sigma_\omega}}$. The high-frequency conductivity $\sigma_\omega(t)$ was calculated by formula (1) with $n_e(t) = \langle n_e(r,t)\rangle_{r=a}$ and the effective collision frequency $\nu_{eff}(t) = \frac{e^2 n_e(t)}{m_e\langle\sigma(r,t)\rangle_{r=a}}$. Here $\sigma(r,t)$ is the local instantaneous static conductivity computed as suggested in previous work.[24]

As seen in the Figure 4, the ratio of skin layer thickness to plasma radius falls off sharply prior to the time of the maximum laser intensity resulting in the peak scattered power occurring prior to the moment of maximum total electron number. The 100 µJ case has the largest skin layer thickness to plasma radius ratio throughout time and thus experiences less of an effect from microwave shielding and correspondingly has a higher scattered power in later times as previously shown in Figure 3.

Since the microwave scattering from the laser induced plasma lies in the Mie regime for the majority of its lifetime, it is important to show the anisotropic nature of the scattered radiation throughout time. A plot of the normalized scattered signal from the simulated laser induced plasma throughout time, for receiver angles of 0, 45, and 60 degrees, is shown in Figure 5. In early time frames, the scattered intensities are roughly equal but quickly diverge due to the inhomogeneous nature of Mie scattering. This shows the effect of the transition from Coherent Rayleigh to Mie scattering on signal response.

Polar plots of the normalized intensity of the scattered signal versus the receiver horn angular position θ , with Φ held constant at 0^o, from the laser induced plasma at times of 1, 5, 7.5, and 9.2 ns are shown in Figure 6. These key times show the angular dependence of scattering intensity both before and after the initial peak in intensity. The isotropic Coherent Rayleigh Scattering can be seen in early time frames whereas the anisotropic Mie Scattering is highly evident in later time frames. The scattering is highly homogenous until roughly 7.5 ns and quite inhomogeneous afterwards. The change in homogeneity of these polar plots throughout time is further evidence showing the transition from Coherent Rayleigh to Mie Scattering.

Conclusions

Through the implementation of microwave scattering theory and the modeling of the plasma evolution induced by a laser spark in air at atmospheric conditions, the apparent differences of Rayleigh and Mie scattering can be seen. The signal response can be characterized by three distinct phases. First, a rapid increase occurs due to avalanche ionization in the Rayleigh regime in the early stages of optical breakdown when the conductivity is relatively low. This is followed by a decrease due to microwave shielding effects in the Mie regime. Finally, an increase as the plasma volume begins to expand and fewer electrons are shielded. This apparent transition from Coherent Rayleigh Scattering to Mie Scattering provides a logical explanation for the signal response seen in experimentation.

Acknowledgments

The work at the University of Tennessee Knoxville was supported by NSF CBET-1032523.

References

1. Raizer, I.F.U.F.P., *Laser-induced discharge phenomena*. Studies in Soviet science : Physical sciences. 1977, New York: Consultants Bureau. xiv, 366 p.

2. Demichel.C, *Laser Induced Gas Breakdown - a Bibliographical Review.* Ieee Journal of Quantum Electronics, 1969. **Qe 5**(4): p. 188-&.

3. Yan, H., et al., *Laser energy deposition in quiescent air.* Aiaa Journal, 2003. **41**(10): p. 1988-1995.

4. Yan, H., et al., *Effect of energy addition on MR -> RR transition.* Shock Waves, 2003. **13**(2): p. 113-121.

5. Loir, A.S., et al., Study of plasma expansion induced by femtosecond pulsed laser ablation and deposition of diamond-like carbon films. Applied Surface Science, 2003. **208**: p. 553-560.

6. Goto, T., High-speed deposition of zirconia films by laser-induced plasma CVD. Solid State Ionics, 2004. **172**(1-4): p. 225-229.

7. Vestin, F., M. Randelius, and A. Bengtson, *Laser-induced breakdown spectroscopy applied on low-alloyed zinc samples.* Spectrochimica Acta Part B-Atomic Spectroscopy, 2010. **65**(8): p. 721-726.

8. Salle, B., P. Mauchien, and S. Maurice, *Laser-Induced Breakdown Spectroscopy in open-path configuration for the analysis of distant objects.* Spectrochimica Acta Part B-Atomic Spectroscopy, 2007. **62**(8): p. 739-768.

9. Samek, O., et al., Application of laser-induced breakdown spectroscopy to in situ analysis of liquid samples. Optical Engineering, 2000. **39**(8): p. 2248-2262.

10. Adamson, M., et al., Laser-induced breakdown spectroscopy at a water/gas interface: A study of bath gas-dependent molecular species. Spectrochimica Acta Part B-Atomic Spectroscopy, 2007. **62**(12): p. 1348-1360.

11. McNaghten, E.D., et al., Detection of trace concentrations of helium and argon in gas mixtures by laser-induced breakdown spectroscopy. Spectrochimica Acta Part B-Atomic Spectroscopy, 2009. **64**(10): p. 1111-1118.

12. Phuoc, T.X., Laser spark ignition: experimental determination of laser-induced breakdown thresholds of combustion gases. Optics Communications, 2000. **175**(4-6): p. 419-423.

13. Phuoc, T.X., *Laser-induced spark ignition fundamental and applications.* Optics and Lasers in Engineering, 2006. **44**(5): p. 351-397.

14. Boker, D. and D. Bruggemann, *Temperature measurements in a decaying laser-induced plasma in air at elevated pressures.* Spectrochimica Acta Part B-Atomic Spectroscopy, 2011. **66**(1): p. 28-38.

15. El-Rabii, H., S.B. Victorov, and A.P. Yalin, *Properties of an air plasma generated by ultraviolet nanosecond laser pulses.* Journal of Physics D-Applied Physics, 2009. **42**(7).

16. Ghorui, S., J.V.R. Heberlein, and E. Pfender, *Thermodynamic and transport properties of two-temperature nitrogen-oxygen plasma.* Plasma Chemistry and Plasma Processing, 2008. **28**(4): p. 553-582.

17. Shneider, M.N. and R.B. Miles, *Microwave diagnostics of small plasma objects.* Journal of Applied Physics, 2005. **98**(3).

18. Zhang, Z.L., M.N. Shneider, and R.B. Miles, *Microwave diagnostics of laser-induced avalanche ionization in air.* Journal of Applied Physics, 2006. **100**(7).

19. Wu, Y., et al., Direct measurement of methyl radicals in a methane/air flame at atmospheric pressure by radar REMPI. Optics Express, 2011. **19**(24): p. 23997-24004.

20. Wu, Y., Z.L. Zhang, and S.F. Adams, *O(2) rotational temperature measurements by coherent microwave scattering from REMPI.* Chemical Physics Letters, 2011. **513**(4-6): p. 191-194.

21. Wolf, M.B.a.E., Principles of Optics: Electromagnetic theory of propagation, interference and diffraction of light. 7 ed. 1999, Cambridge UK: Cambridge University Press.

22. Yu.F. Kolesnichenko, D.V.K., V.G. Brovkin, and S.A. Afanas'ev. Optimization of Laser-Pulse-Controlled MW Energy Deposition. in 45th AIAA Aerospace Sciences Meeting and Exhibit. 2007. Reno, Nevada.

23. Phuoc, T.X., *An experimental and numerical study of laser-induced spark in air.* Optics and Lasers in Engineering, 2005. **43**(2): p. 113-129.

24. Plooster, M.N., Shock Waves from Line Sources - Numerical Solutions and Experimental Measurements. Physics of Fluids, 1970. **13**(11): p. 2665-&.

25. Akram, M., The evolution of spark discharges in gases .2. Numerical solution of one-dimensional models. Journal of Physics D-Applied Physics, 1996. **29**(8): p. 2137-2147.

26. Shneider, M.N., *Turbulent decay of after-spark channels.* Physics of Plasmas, 2006. **13**(7).

27. Brode, H.L., *Numerical Solutions of Spherical Blast Waves.* Journal of Applied Physics, 1955. **26**(6): p. 766-775.

Appendix

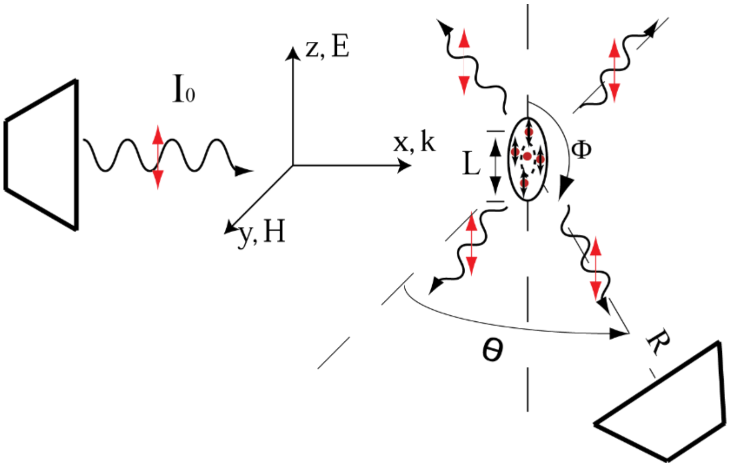

Figure 1. Depiction of microwave Mie scattering from a laser-induced plasma. The microwave is shielded from the plasma due to the skin layer thickness being smaller than the characteristic size of the plasma.

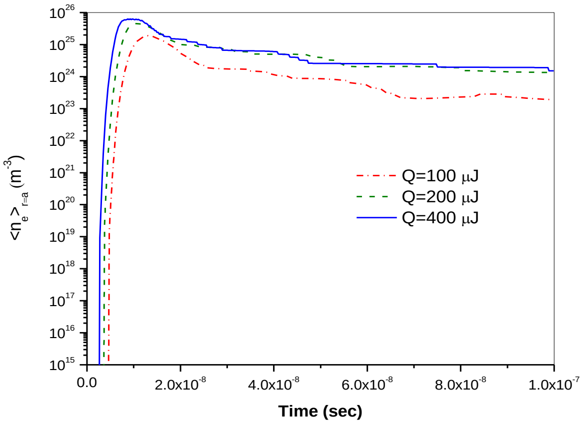

Figure 2. Electron number density versus time of the simulated laser induced plasma for absorbed laser energies of 100, 200, and 400 μJ.

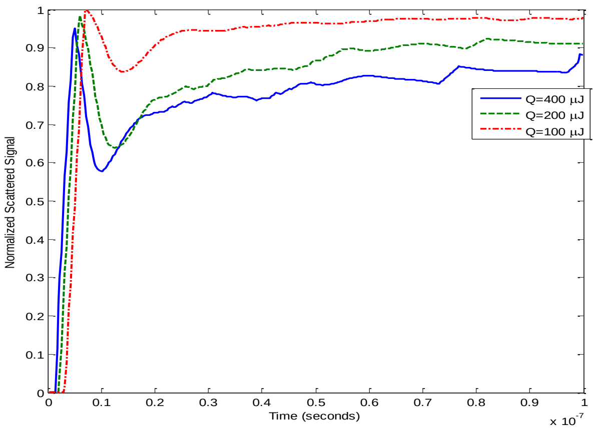

Figure 3. Normalized scattered signal versus time (seconds) from the simulated laser induced plasma for absorbed laser energies of 100, 200, & 400 μJ.

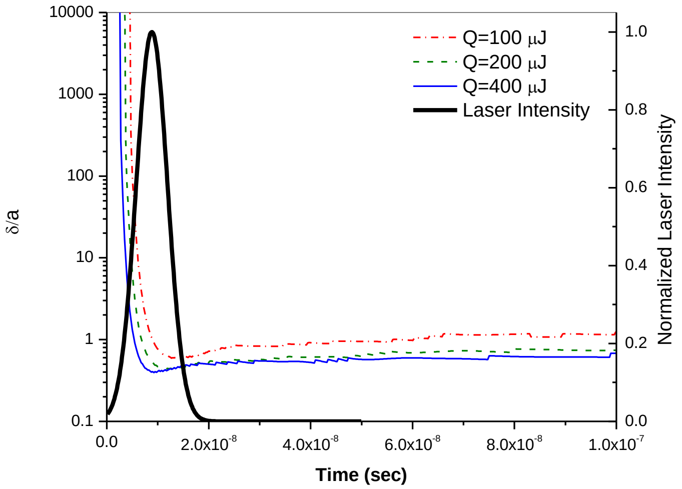

Figure 4. Ratio of skin layer thickness to plasma radius and normalized laser intensity profile versus time (seconds) of the simulated plasma for absorbed laser energies of 100, 200, & 400 μJ. Microwave frequency f=12 GHz.

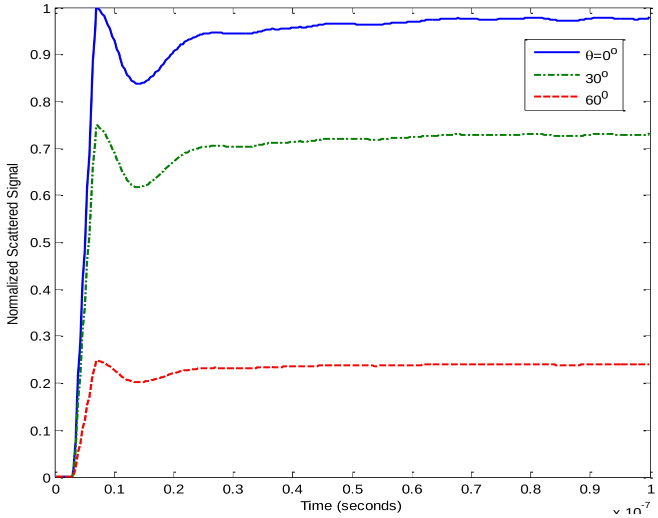

Figure 5. Normalized scattered signal versus time (seconds) from the simulated laser induced plasma for an absorbed laser power of 100 µJ and microwave receiver horn angles of 0º, 30º, & 60º.

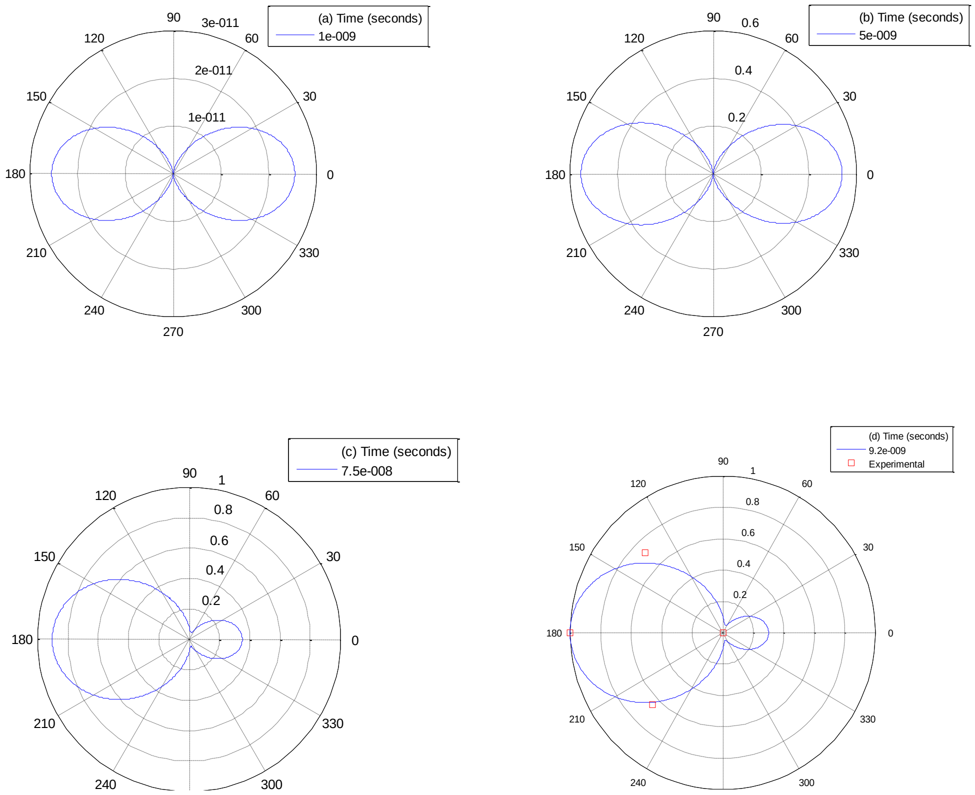

Figure 6. Polar plots of the normalized scattered signal from the simulated laser induced plasma for an absorbed laser energy of 400 μJ at times of: (a) 1 ns ,(b) 5 ns , (c) 7.5 ns , and (d) 9.2 ns (includes experimental results at peak intensity).

CHAPTER II

QUANTITATIVE MEASUREMENT OF ELECTRON NUMBER IN NANOSECOND AND PICOSECOND LASER-INDUCED AIR BREAKDOWN

This article, “Quantitative Measurement of Electron Number in Nanosecond and Picosecond Laser-induced Air Breakdown”, was received on the 21st of September 2015, accepted on the 20th of April 2016, and published on the 5th of May 2016.

Author affiliations:

Yue Wu[1], Jordan C. Sawyer[1], Liu Su[1], and Zhili Zhang[1]

[1]Department of Mechanical, Aerospace and Biomedical Engineering, University of Tennessee, Knoxville, TN 37996, USA

Wu, Y., et al., Quantitative measurement of electron number in nanosecond and picosecond laser-induced air breakdown. Journal of Applied Physics, 2016. **119**(17): p. 173303.

Abstract

In this chapter, we present quantitative measurement of total electron number in laser-induced air breakdown at pressures ranging from atmospheric to 40 bar_g, by 10 ns and 100 ps laser pulses. A quantifiable definition for the laser-induced breakdown threshold is defined by a sharp increase in the measurable total electron number via dielectric-calibrated coherent microwave scattering. For the 10 ns laser pulse, the threshold of laser-induced breakdown in atmospheric air is defined as the total electron number of $\sim10^6$. This breakdown threshold decreases with an increase of pressure and laser photon energy (shorter wavelength), which is consistent with the theory of initial multiphoton ionization and subsequent avalanche process. For the 100 ps laser pulse cases, a clear threshold is not present and only marginal pressure effects can be observed, which is due to the short pulse duration leading to stronger multiphoton ionization and minimal collisional avalanche ionization.

Introduction

Since the 1960s, laser induced air breakdown processes have been extensively studied due to its wide applications in scientific and engineering fields with minimal system complexity.[1-3] Laser-induced plasma and breakdown in gases have been extensively investigated due to their wide applications in laser ignition, laser-induced breakdown spectroscopy (LIBS) and etc.[4] Laser-induced breakdown starts with the generation of seed electrons via multiphoton ionization (MPI) process, in which a gaseous atom or molecule simultaneously absorbs multiple photons to be ionized.[5] The seed electrons are then accelerated by the beam's electromagnetic field via the inverse Bremsstrahlung effect. If a sufficient field is applied, the electrons are accelerated to energies that cause electron impact ionization upon collisions with the neutral gas atoms and molecules. The newly liberated electrons then are accelerated by the field leading to an electron avalanche ionization (EAI) process during the laser pulse duration. The EAI process manifests as a visible laser spark which emits light and heats the surrounding medium producing a shock wave that propagates from the breakdown region. Various studies have focused on the effects of various parameters of the laser beam (i.e. laser wavelengths[6-8], laser pulse widths [9, 10], focal areas[11]), and gas pressures [12], and other gas properties on the laser-induced gas breakdown process with various diagnostics such as emission spectroscopy[13, 14], interferometry[15, 16] and Thomson scattering.[17, 18] These parameters have been shown to be related to either the MPI or EAI phases of the laser-induced gas breakdown process [19].

Until recently laser-induced gas breakdown was commonly detected by human eyes, photodiodes, and/or cameras with a probability-based criterion[9]. Typically, this criterion is the visible observation of a glow or flash in the focal region for a probability of 10%-50% of the laser firings.[8] Such criteria are qualitative and maybe inaccurate. A visible spark produced by an intense laser beam generally occurs at the end of or after the laser pulse duration which cannot clearly reveal the MPI and EAI processes and their corresponding effects during the laser-induced gas breakdown processes. Moreover, at higher pressures self-absorption becomes prominent, possibly leading to inaccurately high intensity threshold measurements.

In this chapter, the free electrons produced by laser-induced plasma and breakdown have been quantitatively measured by dielectric-calibrated coherent microwave scattering. The electron generation and its temporal evolution have been monitored after the laser onset. A new quantitative definition of the threshold intensity for laser induced breakdown is presented as the total electron number during onset of the laser-induced plasma and breakdown process. Threshold measurements were taken in air at pressures ranging from atmospheric to 40 bar_g. Comparisons to the qualitative observation and probability based criteria are made. The effects of pressure and laser wavelengths (the 1st-3rd harmonics of a Nd:YAG laser, i.e., 1064 nm, 532 nm, and 355 nm) and pulse duration (10 ns and 100 ps) on the quantitative breakdown thresholds were confirmed that the breakdown threshold decreases with the increase of pressure and/or laser photon energy (shorter wavelength), which is consistent with the previous assessments.

Experimental Setup

The experimental setup for the measurement of laser-induced breakdown is shown in Figure 7. This setup is similar to that used in previous works.[20] Hence, the experimental setup is briefly introduced here. For ns laser induced breakdown, the fundamental (1064 nm), the second and third harmonics (532 and 355 nm) from a Nd: YAG nanosecond laser were individually selected to generate laser-induced breakdown in air within a high-pressure cell. For ps cases, the fundamental and second harmonics of Nd:YAG picosecond laser were used. The laser beam was first split with a portion going to a laser power meter for monitoring of the incident laser power.

A second laser power meter was used to simultaneously record the energy of the transmitted laser beam. The incident laser beam was focused into the center of the cell via a 125-mm long focal length lens. The high-pressure stainless steel cell is cylindrical in shape and rated up to 100 bar_g (gauge pressure). The high-pressure cell has three quartz windows for optical access used in the LIB experiments. Two windows provide line of sight access to the axial direction and the third in the radial direction. One high pressure port is connected to a compressed air tank (Airgas Breathing Air Grade D) while the other port is connected to a pressure transducer.

The total electron number during the laser-induced breakdown was monitored through the radial optical window using the microwave detection system (MDS). Since the size of the plasma (initially ~44 microns in diameter) being generated in the cell is much smaller than the microwave wavelength (0.3 cm), the microwave scattering mostly falls into the Rayleigh regime, with the re-radiated electric-field amplitude of the plasma proportional to the number of electrons.[21] A 10-dBm tunable microwave source (HP 8350B sweep oscillator, set at ~10 GHz) was split into two channels. One of the channels was used to illuminate the plasma by employing a microwave horn (WR75, 15-dB gain). The backscattering is monitored through a homodyne transceiver detection system (the MDS shown in Figure 8 subplot). The scattering from the plasma is collected by the same microwave horn. The signal passes through a microwave circulator and is amplified 30 dB by one preamplifier at ~10 GHz. After the frequency is down-converted with by mixing with the second channel, two other amplifiers with bandwidth in the range 2.5 kHz – 1.0 GHz amplifies the signal 60 dB. Considering the geometry of dipole radiation of microwave, the polarization of the microwave is chosen to be along the propagation direction of the laser beam, maximizing the scattering signal. The microwave detection system (MDS) can be used to monitor the generation and evolution of electrons in the breakdown region. A gated ICCD camera has been applied to estimate the size of the plasma by spontaneous emissions and then one can quantitatively determine the total electron number as a function of the incident laser intensity and absorption energy during the laser-induced breakdown in air.

Results and Discussions

Measurements of Laser Transmission and Absorption through the Cell

The detection system for laser absorption measurements was calibrated for the 10 ns beam at 1064 nm, 532 nm, and 355 nm wavelengths. During the system calibration, the focusing lens was removed from the experimental setup. This allowed for us to account for losses at the windows for all three wavelengths. Additionally, absorption of the unfocused beam by the air was determined for pressures of 0 bar_g, 20 bar_g, and 40 bar_g. When using the unfocused beam, there were no detectable ionization by the microwave system and no formation of visible laser sparks. The incident and transmitted beam energies were monitored by a laser power meter.

Figure 8 shows normalized transmitted energies versus the normalized incident laser energies for the high pressure cell. Experimental transmittance was determined by linear fitting the data with a zero intercept. The slope of the fitted line is defined as the transmittance of the system which is related to the wavelength of the laser beam and the air pressure as shown in Figure 9. The transmittance is largely independent of the air pressures at the wavelengths of 1064 and 532 nm. However, a slight dependence is seen for the 355 nm ultraviolet beam, corresponding to the larger absorption and Rayleigh scattering cross-section at this wavelength. At higher pressures, ultraviolet light (355nm) can be attenuated by more than 20%. The transmittance at these three wavelengths and pressures were used as a calibration for determining the threshold energies and intensities for laser induced breakdown.

Laser Beam Characterization

A beam profiler (Ophir BeamGate) was used to acquire a two-dimensional (2D) beam energy profile of the laser beam at the focal point. The visible laser beam (532 nm) was focused by a 125 mm focal length lens in this measurement. The focused beam profile is shown in Figure 10. with both one- and two-dimensional spatial distributions. The 2D profile is averaged over twenty laser pulses. Shot-to-shot laser energy fluctuations are accounted for in the form of error bars in the figure. The experimental data was well fitted by the Gaussian distributions with high R-square values (greater than 99%). The Full Width at Half Maximum (FWHM) was ~ 43 ± 1 μm. This technique was also applied for the laser fundamental (1064 nm) and third harmonic (355 nm). The focused beam dimensions were utilized in laser intensity calculations shown later on.

Dielectric-Calibrated Coherent Microwave Scattering

The total electron number during the laser induced plasma generation and evolution is a key parameter. The coherent microwave scattering apparatus was calibrated by using dielectric materials (e.g. alumina and PTFE). The detailed calibration strategy and procedure have been well illustrated in [22] and will be briefly introduced here. This method expands from the relative coherent microwave scattering to quantitative total electron number measurements by calibrating with simple dielectric materials of well-known properties, which can be applied for quantitative measurements of atomic and molecular species in plasmas and flames.[23, 24] In this work, the calibration allowed for a quantitative measurement of the total electron number within the laser-induced breakdown region.

The microwave scattering signal from the detection system can be written for the limiting cases of a perfect conductor or a perfect dielectric scatterer placed in the illumination region as follows:

$$U_c = A\sigma V_c, \qquad \text{for perfect conductor}$$
$$U_d = A\varepsilon_0(\varepsilon_r - 1)\omega V_d, \qquad \text{for dielectirc} \qquad (1)$$

where U_c and U_d are the microwave signals, A is the characteristic parameter of the microwave detection system, σ is the electrical conductivity of the scatter, ε_r is the relative permittivity of the scatter, ε_0 is the free space permittivity, ω is the angular frequency of microwave, and V_c and V_d are the volumes of the scatterers, respectively. By measuring the microwave scattering from a sample material with known dielectric properties placed within the illumination region one may determine the microwave detection system characteristic A at the sample's location. A small cylindrical sample of alumina or PTFE was mounted at the laser beam focal point with the cylinder's axis parallel to the laser's propagation direction. This approach slightly differed from the previous work[22], which used dielectrics launched through the microwave illumination region.

The microwave scattering signals from alumina and PTFE are shown in Fig. 5. The parameter A was measured to be 80.5 V·Ω/cm^2 and 82.6 V·Ω/cm^2 with alumina and PTFE calibrators, respectively. The measurement of A should be more accurate with the use of alumina due to its larger ε value leading to a stronger scattering signal. Therefore, the coefficient A = 80.5 V·Ω/cm^2 was used for all further calculations with a standard deviation of the coefficient less than 15%. With the same detection system and experimental setup, the temporal evolution of total electron number by laser-induced breakdown is also shown in Figure 11with the laser energy inputs of 70, 35 and 16 mJ at 1064, 532 and 355 nm, respectively. By using the system parameter A and the estimated volume of plasma column, one can determine the conductivity of the plasma column from the microwave signal. The electron density in the plasma can then be determined by using the expression:

$\sigma = 2.82 \times 10^{-4} n_e \nu_m / (\omega^2 + \nu_m^2)$ Ω^{-1} cm^{-1}, (2)

where ν_m is the frequency of electron-neutral collisions$\nu_m \approx 2 \times 10^9 p[Torr], s^{-1}$, n_e is the electron density (cm^{-3}), and ω is the angular frequency (s^{-1}). [25] Hence, the total electron number in the plasma can be explicitly expressed as:

$$N_e = \frac{\varepsilon_0(\varepsilon-1)V_d}{2.82\times10^{-4}} \cdot \frac{U_c}{U_d} \cdot \frac{\omega(\omega^2+\nu_m^2)}{\nu_m} \qquad (3)$$

Temporally resolved measurements of total electron number during the laser-induced breakdown process were made with the use of the dielectric-calibrated coherent microwave scattering technique. Figure 12(a) and (b) show two typical total electron number evolution measurements at 0 $\mathrm{bar_g}$ and 30 $\mathrm{bar_g}$. Energy absorption measurements took into account the previously calculated transmittances. In general, as more energy was absorbed at the focal region, more electrons were produced during the laser-induced breakdown processes. The total electron number increases with an increase of energy deposition. It should be noted that the time scale for microwave scattering signal to reach the maximum value are dramatically different between atmospheric pressure and elevated pressure (i.e. 30 $\mathrm{bar_g}$) as shown in Figure 12(a) and (b). At 0 $\mathrm{bar_g}$, the rising time for the maximum is around 10 ns after the laser onset while the time is around 350 ns at 30 $\mathrm{bar_g}$. A precursor signal (Figure 12(a)) is witnessed prior to the temporal evolution at atmospheric pressure. However, such precursors were not detected at any elevated pressure conditions (from 10 $\mathrm{bar_g}$). At elevated pressure conditions, the electron density of the plasma at the initial stage (less than a few hundred nanoseconds after laser onset) is much higher which reaches the critical limitation for microwave detection of plasma. The microwave could not penetrate the dense plasma and only part of electrons near plasma surface can be detected which is not able to quantitatively measure the total electrons of the plasma in such initial phase. Because of the limitation of microwave detection on dense plasma, the total electron number within plasma was calculated at different plasma evolution time for the atmospheric and elevated pressure conditions. As shown in Figure 12(a), the total electron number was calibrated from the microwave signal at 10 ns after the laser onset at 1 atm condition. While at elevated pressure conditions (i.e. 30 bar_g shown in Figure 12(b)), the total electron number calculation has been delayed 350 ns after the laser onset considering the plasma expansion and density.[26] Hence, beside the relative microwave signals shown in Figure 12, we estimated the plasma size at those specific time delays for different pressure conditions.

Figure 13(a) and (b) show a visualization of the plasma temporal evolution at 1 atm and 10 bar_g by monitoring of spontaneous emission using the 10-ns 532-nm laser beam for the air breakdown generation. The spontaneous emission within the plasma provided an access to estimate the size of plasma itself. Using the temporal coherent microwave scattering signal (Figure 12) and plasma size evolution (Figure 13) offered the chance to quantitatively measure the total number of electrons throughout the plasma evolution. Since peak microwave scattering signals are seen at different times depending on pressure, the peak total number of electron are then calculated at the corresponding peak microwave scattering time. For ambient air condition, the time is ~10 ns. For elevated pressure conditions, the time approaches 300~400 ns.

The upper limit of the measurable electron number density using this technique is determined by the plasma column diameter, skin depth, and plasma critical density. The skin depth of the plasma given by [20]:

$\delta = \frac{5.03}{\sigma f}\ [cm]$ (4)

where σ is the plasma conductivity in Ω^{-1} cm^{-1} (given by equation 2) and f is the microwave frequency in MHz. The skin depths for air plasmas at pressures ranging from atmospheric to 40

bar_g were calculated for an illuminating microwave at 10 GHz as shown in Figure 14. When the skin depth is much larger than the width of the plasma column the microwave scattering will fall into the Rayleigh regime. In this case the scattering signal is proportional to the total number of electrons within the illumination region. However, when the skin depth approaches the size of the plasma width shielding of some of the electrons will occur. As shown in the figure, this shielding effect is more prevalent at lower pressures. The limit to this case is determined by the critical density of the plasma given by

$$n_{cr} = 1.24 \times 10^{-8} \cdot (f)^2 (cm^{-3})$$

For 10 GHz microwave illumination the critical electron density is 1.24×10^{12} (cm^{-3}), which acts as the limit of measurable electron number density in the cases presented in this work. The plasma emission (Figure 13) was used to estimated plasma column for both atmospheric pressure and elevated (>10 Bar_g) pressure, which can estimate a limit on the measurable total electron number for those cases. Effective total electron number limits for these estimated plasma column sizes are 2.36×10^9 μm^3 and 5.30×10^{10} μm^3, respectively. Although the plasma volume is not perfectly cylindrical and is highly dependent on laser wavelength, this limit estimation gives the reader a scale with which to compare our threshold measurements.

With the measured microwave signals and estimated plasma column, the total electron number during the laser-induced breakdown process for the 10 ns beam at 1064 nm, 532 nm, and 355 nm wavelengths is calculated as shown in Figure 15(a), (b), and (c) respectively. In these three figures the laser-induced breakdown in air was measured for pressures ranging from atmospheric to 40 bar_g. The total electron number is presented as a function of the laser intensity. For the first two conditions (Figure 15(a) and (b)) and their corresponding laser wavelengths, there is a threshold intensity. Below the threshold intensity, at a given pressure condition, the total electron number profile is relatively independent of laser intensity. Above the threshold value, the total electron number increases significantly with increasing laser intensity. The threshold intensity is mostly clearly seen for the longer laser wavelengths and lower pressure conditions.

These threshold intensities for inducing laser-induced breakdown with a 1064 nm beam are roughly an order of magnitude higher than threshold intensities for the 532 nm and 355 nm beams. Additionally, for laser intensities below the breakdown threshold the 1064 nm and 532 nm beams have detectable total electron numbers on the order of ~10^5. The 355 nm beam at similar intensities has about an order of magnitude higher total electron number (~10^6). This is mostly likely due to higher energy photons of the UV beam producing more electrons during the MPI process.

For all three wavelengths, it is clearly shown that increasing the pressure leads to more efficient electron production for a given laser intensity. A small amount of electrons (10^5) was measured at the 0 bar_g pressure condition. When the pressure is above 10 bar_g the total electron number increases to above 10^6. At pressures above 10 bar_g, the total electron number dramatically increases with small increases in laser intensity. This indicates that the EAI process is dominant for elevated pressures for laser-induced breakdown.

Figure 16 shows the correlation between total electron number and absorbed laser energy for laser induced breakdown in air at pressures ranging from atmospheric to 40 bar_g with 1064 nm, 532 nm, and 355 nm beams. There is a clear relationship between the minimum detectable total electron number and laser wavelength. For a 355 nm beam, the energy absorption of ~0.15 mJ is needed to generate detectable plasma at the focal point. For the infrared beam (1064 nm), energy absorption must be an order of magnitude higher (~1 mJ) to generate a detectable plasma. This once again corresponds to the conclusion that the higher energy photons will be more efficient at electron production through the MPI process. At the elevated pressure conditions (above 10 bar_g), the curve of total electron number has unique pressure dependence for each laser wavelength. For the 1064 nm laser beam, the total electron number is two orders of magnitude lower at atmospheric pressures than at 40 bar_g. Such effect is far less pronounced for the 532 nm and 355 nm beams. This corresponds to a higher dependence on the EAI process for laser-induced breakdown by the 1064 nm beam.

It is worth to note that the time window for the measurement of total electron number is highly dependent on the plasma density at different pressure conditions. For atmospheric pressure condition, the electron has been detected within 10 ns short after the laser onset indicating that the plasma density is relative low and such condition is appropriate for the microwave Rayleigh scattering detection. At elevated pressure conditions, the electron measurements were accomplished at 300~400 ns after the laser onset. Because the plasma was over dense (above critical density) at the beginning of the plasma evolution and microwave could only detect a few electrons near the skin of the plasma. After the plasma expanded and the electron density decreased, the microwave detection system was then applicable for the measurement of total electron number.

ps Laser Induced Plasma and Breakdown

Figure 17 shows the peak microwave signal versus absorbed laser energy during laser induced breakdown by 100ps laser pulses at 532 nm and 1064 nm for pressures up to 40 bar_g, respectively. These peak microwave signals correspond to peaks in the total electron number. An important distinction between ns and ps cases is that the peak signals for the 100 ps pulses have no threshold phenomena observed. The electrons can be generated at very low pulse energies, which is in stark comparison with ns cases of 1064nm and 532nm. This corresponds to a dominant MPI process for the high intensity beam. Within a single pulse duration of 100ps, there is not enough time for multiple collisions, which limit the avalanche ionization processes. At higher pressures, weak threshold phenomena are shown, which is due to increased collisional frequency leading to slightly increased avalanche ionization processes. More electrons can be generated at higher pulse energies, which is consistent with the subsequent MPI and avalanche ionizations in ns cases. In Figure 17(a), the high pressure condition (i.e. 30 bar_g and 40 bar_g) favors the MPI process and generate more electrons by using 532 nm ps laser. Meanwhile, Figure 17(b) shows that the low pressure condition (i.e. 0 barg and 1 barg) favors the avalanche ionization by using 1064 nm ps laser. The difference result by using 532 nm and 1064 nm laser beam indicates that the ps laser-induced breakdown in air is dependent on the laser energy as well. Unfortunately, due to limited facility scheduling a dielectric calibration for the 100 ps data subset was not obtained. However, the peak microwave signal versus energy absorption trends has interesting behavior warranting their discussion.

Quantitative Laser Induced Breakdown Threshold

As discussed previously, the breakdown threshold is commonly defined as the lowest laser intensity at which a spark is visibly observed at a probability of 10% ~ 50% averaged over many laser pulses. The temporal evolution studies of laser sparks are mainly on the microsecond time scale which does not reveal critical information about the laser-induced breakdown process. The threshold value of laser intensity to generate laser-induced breakdown in air for pressures ranging from atmospheric to 40 bar_g for 1064 nm and 532 nm beams is shown in Figure 18. The 355 nm beam has not been shown here because there is not clear transition from MPI to EAI by using such UV beam source. The microwave detection system could detect seed electrons even with very low energy input. The threshold laser intensity profiles have little to no dependence on pressure for the 532 nm beam. The 1064 nm threshold laser intensity initially increases with increasing pressure before gradually decreasing with increasing pressure. This once again is indicative of a larger dependence on the EAI process for the laser-induced breakdown with the 1064 nm beam.

Conclusions

Quantitative measurements of threshold total electron number for laser-induced air breakdown by ns and ps laser pulses at various pressures were presented. The threshold ns laser intensities to generate laser-induced breakdown in air with pressures ranging from atmospheric were determined. Dielectric-calibrated coherent microwave scattering was used to measure the total electron number density during the laser-induced breakdown in air. The plasma size has been estimated as well in order to calculate the total number of electrons at specific times. By careful examination of the total number of electron versus laser intensity profiles, a new criterion for laser-induced air breakdown threshold was introduced. The quantitative thresholds under various conditions confirm the dependence on wavelengths and pressures on the defining criterion. Laser induced breakdown by ps pulses shows different non-threshold effects. Both measurements confirmed the interactions of MPI and avalanche ionization for laser induced breakdown processes, i.e., MPI generates initial seed electrons and subsequent avalanche ionization overtakes the growth if enough collisions are made.

Acknowledgments

The work at University of Tennessee was supported by NSF PHY-1418848 and AFOSR under Dr. Chiping Li.

References

1. Nelson, P., et al., *Experimental and Theoretical Studies of Air Breakdown by Intense Pulse of Light.* Physics Letters, 1964. **13**(3): p. 226-228.

2. Buscher, H.T., Tomlinso.Rg, and E.K. Damon, *Frequency Dependence of Optically Induced Gas Breakdown.* Physical Review Letters, 1965. **15**(22): p. 847-&.

3. Kroll, N. and K.M. Watson, *Theoretical Study of Ionization of Air by Intense Laser Pulses.* Physical Review A, 1972. **5**(4): p. 1883-&.

4. Phuoc, T.X., *Laser-induced spark ignition fundamental and applications.* Optics and Lasers in Engineering, 2006. **44**(5): p. 351-397.

5. Morgan, C.G., *Laser-Induced Breakdown of Gases.* Reports on Progress in Physics, 1975. **38**(5): p. 621-&.

6. Tambay, R. and R.K. Thareja, LASER-INDUCED BREAKDOWN STUDIES OF LABORATORY AIR AT 0.266, 0.355, 0.532, AND 1.06 MU-M. Journal of Applied Physics, 1991. **70**(5): p. 2890-2892.

7. Tambay, R., et al., *Laser-Induced Air Breakdown Using 0.355, 0.532, and 1.06 Mu-M Radiation.* Pramana-Journal of Physics, 1991. **37**(2): p. 163-166.

8. Thiyagarajan, M. and J.E. Scharer, *Experimental Investigation of 193-nm Laser Breakdown in Air.* Ieee Transactions on Plasma Science, 2008. **36**(5): p. 2512-2521.

9. Wang, C.C. and L.I. Davis, New Observations of Dielectric Breakdown in Air Induced by a Focused Nd3+-Glass Laser with Various Pulse Widths. Physical Review Letters, 1971. **26**(14): p. 822-&.

10. Williams, W.E., M.J. Soileau, and E.W. Vanstryland, *Picosecond Air Breakdown Studies at 0.53-Mu-M.* Applied Physics Letters, 1983. **43**(4): p. 352-354.

11. Ireland, C.L.M., et al., *Focal-Length Dependence of Air Breakdown by a 20-Psec Laser Pulse.* Applied Physics Letters, 1974. **24**(4): p. 175-177.

12. Thiyagarajan, M. and S. Thompson, *Optical breakdown threshold investigation of 1064 nm laser induced air plasmas.* Journal of Applied Physics, 2012. **111**(7).

13. Hummelt, J.S. and J.E. Scharer, Excitational energy transfer enhancing ionization and spatial-temporal evolution of air breakdown with UV laser radiation. Journal of Applied Physics, 2010. **108**(9).

14. Sturm, V. and R. Noll, Laser-induced breakdown spectroscopy of gas mixtures of air, CO2, N-2, and C3H8 for simultaneous C, H, O, and N measurement. Applied Optics, 2003. **42**(30): p. 6221-6225.

15. Way, J., J. Hummelt, and J. Scharer, Experimental measurements of multiphoton enhanced air breakdown by a subthreshold intensity excimer laser. Journal of Applied Physics, 2009. **106**(8).

16. Sobral, H., et al., Temporal evolution of the shock wave and hot core air in laser induced plasma. Applied Physics Letters, 2000. **77**(20): p. 3158-3160.

17. Diwakar, P.K. and D.W. Hahn, Study of early laser-induced plasma dynamics: Transient electron density gradients via Thomson scattering and Stark Broadening, and the implications on laser-induced breakdown spectroscopy measurements. Spectrochimica Acta Part B-Atomic Spectroscopy, 2008. **63**(10): p. 1038-1046.

18. Dzierzega, K., et al., *Thomson scattering from laser induced plasma in air.* 14th International Symposium on Laser-Aided Plasma Diagnostics (Lapd14), 2010. **227**.

19. Yalin, A.P., et al., Laser plasma formation assisted by ultraviolet pre-ionization. Physics of Plasmas, 2014. **21**(10).

20. Wu, Y., et al., Resonant- and avalanche-ionization amplification of laser-induced plasma in air. Journal of Applied Physics, 2014. **116**(14).

21. Zhang, Z.L., M.N. Shneider, and R.B. Miles, Coherent microwave rayleigh scattering from resonance-enhanced multiphoton ionization in argon. Physical Review Letters, 2007. **98**(26).

22. Shashurin, A., et al., Temporary-resolved measurement of electron density in small atmospheric plasmas. Applied Physics Letters, 2010. **96**(17).

23. Wu, Y., et al., Direct measurement of methyl radicals in a methane/air flame at atmospheric pressure by radar REMPI. Opt. Express, 2011. **19**(24): p. 23997-24004.

24. Shneider, M.N., Z. Zhang, and R.B. Miles, Simultaneous resonant enhanced multiphoton ionization and electron avalanche ionization in gas mixtures. Journal of Applied Physics, 2008. **104**(2).

25. Raizer, Y.P., *Gas Discharge Physics*, ed. J.E. Allen. 1991: Springer-Verlag Berlin Heidelberg. 449.

26. Zhang, Z., M.N. Shneider, and R.B. Miles, *Microwave diagnostics of laser-induced avalanche ionization in air.* Journal of Applied Physics, 2006. **100**(7): p. 074912-6.

Appendix

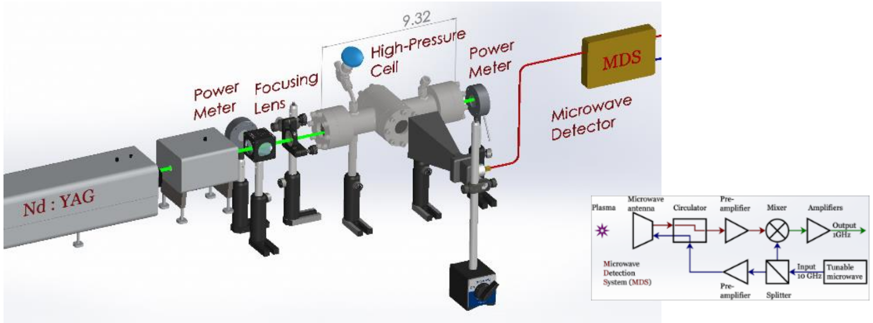

Figure 7. The experimental setup for the laser-induced breakdown thresholds and total electron number measurements.

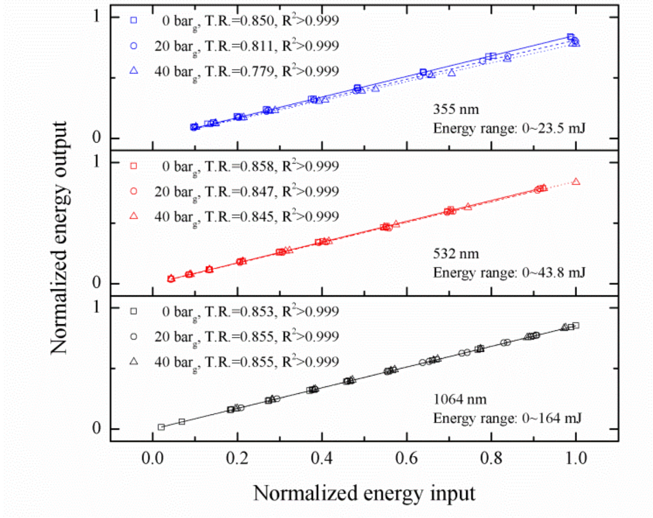

Figure 8. The system calibration with the 10 ns beam in the high pressure chamber. T.R. used here corresponds to transmittance.

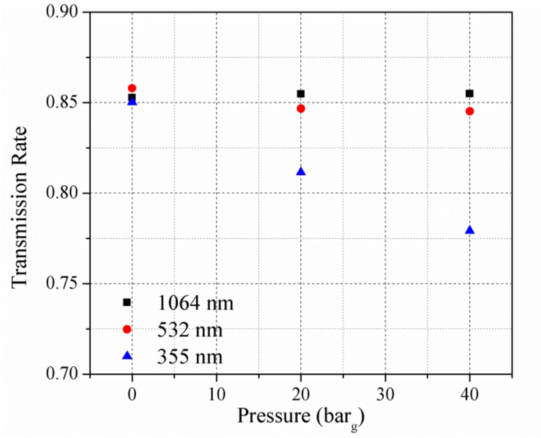

Figure 9. The transmittance of the 10 ns beam with respect to the laser wavelength at various pressure conditions in air through the 20 cm long cell.

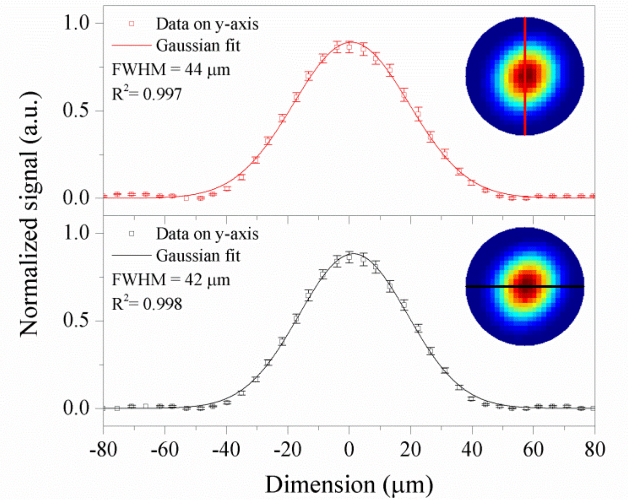

Figure 10. The intensity profile and Gaussian fit of the 10 ns 532 nm laser beam after the focusing lens.

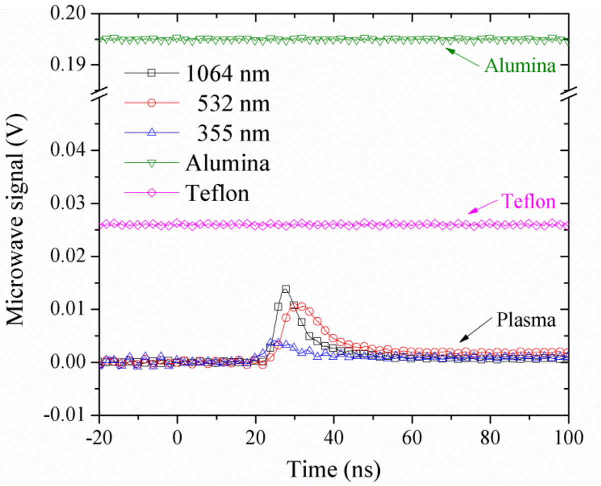

Figure 11. The microwave scattering signals from dielectric materials (alumina and PTFE) and laser-induced air breakdown by using 10 ns 1064, 532, and 355 nm laser beam, respectively.

Temporally-resolved Quantitative Measurement of Total Electron Number in ns Laser Induced Plasma

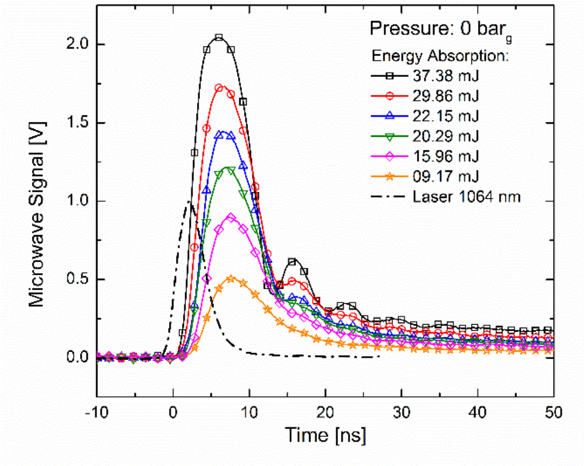

(a)

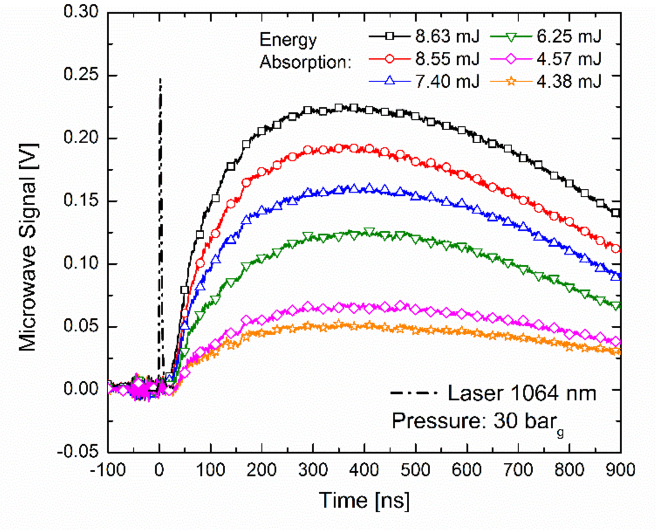

(b)

Figure 12. (a) The microwave signal corresponding to total electron number in the laser-induced breakdown in air at 0 bar$_g$ generated by the 10 ns 1064 nm laser beam. (b) The microwave signal corresponding to total electron number in the laser-induced breakdown in air at 30 bar$_g$ generated by the 10 ns 1064 nm laser beam.

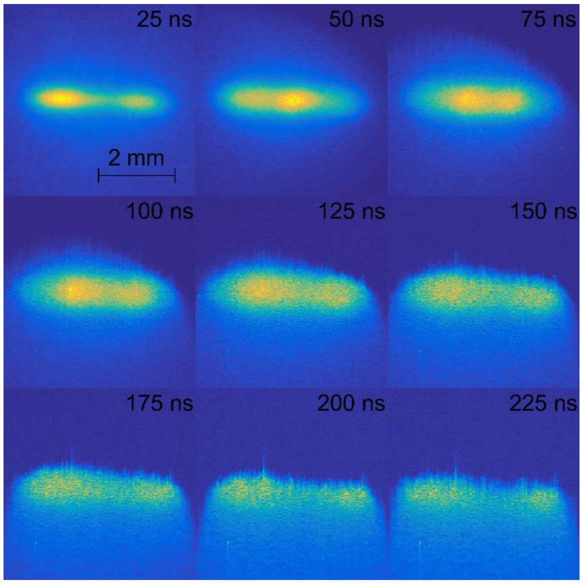

(a)

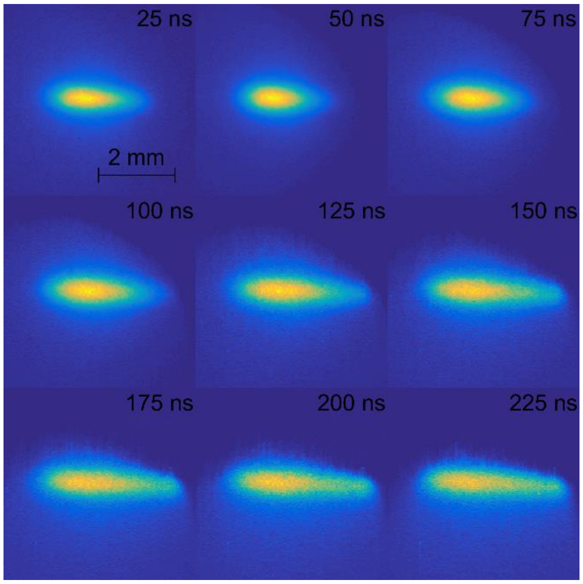

(b)

Figure 13. (a) The spontaneous emission from laser-induced breakdown in ambient air by using 532-nm laser beam. (b) The spontaneous emission from laser-induced breakdown in air at 10 bar_g by using 532-nm laser beam.

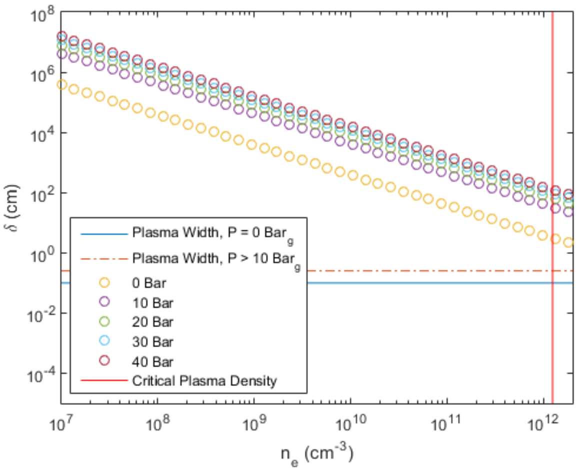

Figure 14. Calculated skin depth versus electron number density for an air plasma illuminated by 10 GHz microwave. Estimated plasma column diameters of 1 mm and 1.5 mm correspond to atmospheric and elevated (>10 Bar_g) are shown for comparison with skin depth. The critical plasma density acts as the limit for the measurement for the cases presented in this work.

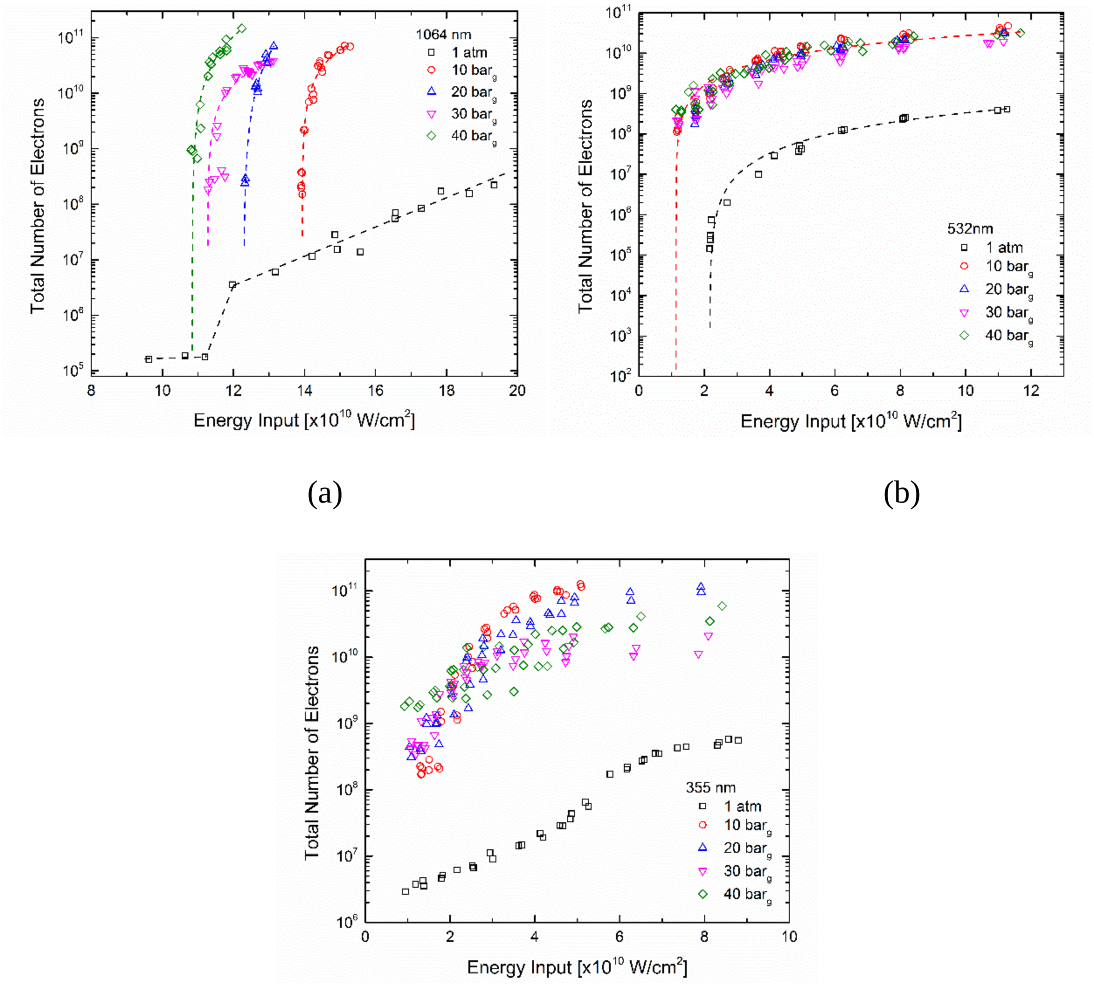

(a)

(b)

(c)

Figure 15. (a) Total number of electron versus laser intensity for the 1064 nm wavelength beam. (b) Total number of electron versus laser intensity for the 532 nm wavelength beam. (c) Total number of electrons versus laser intensity for the 355 nm wavelength beam.

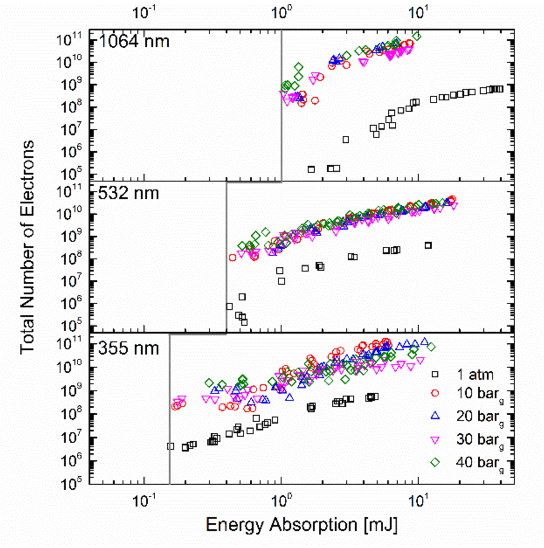

Figure 16. Total electron number versus laser energy absorption during laser induced breakdown in air at pressures ranging from atmospheric to 40 bar$_g$ with 1064 nm, 532 nm, and 355 nm wavelength beams.

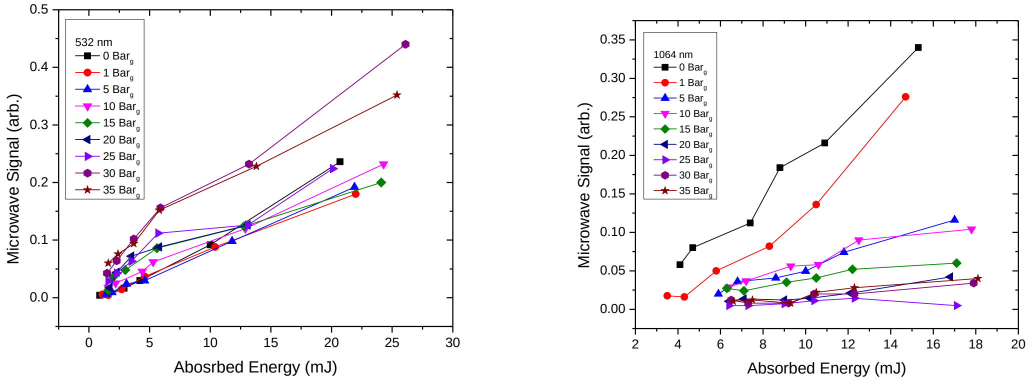

(a) (b)

Figure 17. (a) Peak microwave signal versus absorbed laser energy during laser induced breakdown of air with a 532 nm 100 ps beam. (b) Peak microwave signal versus absorbed laser energy during laser induced breakdown of air with a 1064 nm 100 ps beam.

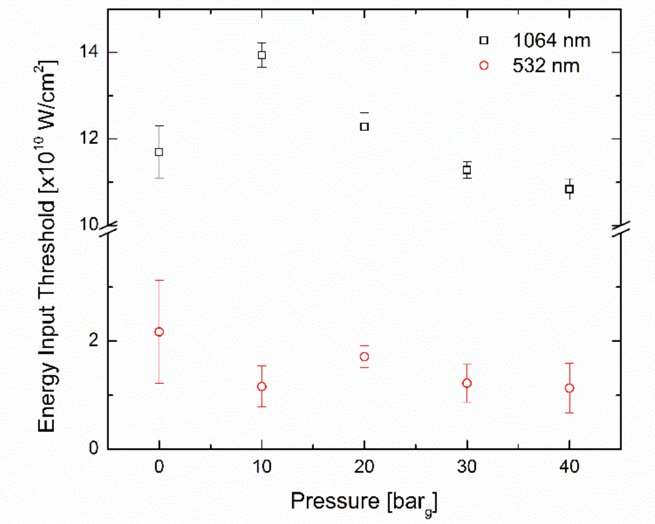

Figure 18. Laser-induced air breakdown threshold versus air pressure for 1064 nm and 532 nm laser wavelengths.

CHAPTER III

HIGH-REPETITION-RATE LASER IGNITION OF FUEL-AIR MIXTURES

This article, “High-Repetition-Rate Laser Ignition of Fuel-Air Mixtures”, was received on the 5th of February 2016, accepted on the 2nd of March 2016, and published on the 29th of March 2016.

Author affiliations:

Paul S. Hsu[1], Zhili Zhang[2], Jordan Sawyer[2], Mikhail N. Slipchenko[1], James R. Gord[3], and Sukesh Roy[1]

[1]Spectral Energies, LLC, Dayton, OH 45431, USA

[2]Department of Mechanical, Aerospace, and Biomedical Engineering, University of Tennessee, Knoxville, TN 37996, USA

[3]Air Force Research Laboratory, Aerospace Systems Directorate, Wright-Patterson AFB, OH 45433, USA

Hsu, P.S., et al., High-repetition-rate laser ignition of fuel–air mixtures. Optics Letters, 2016. 41(7): p. 1570-1573.

Abstract

In this chapter, a new approach to laser ignition (LI) of fuel-air mixtures that utilizes a high-repetition-rate (HRR) nanosecond laser pulse train scheme is presented. The most common traditional LI employs single-nanosecond laser pulses with energies on the order of tens of milijoules to ignite combustible gaseous mixtures. Due to these high energy per pulse requirements, fiber coupling of traditional LI systems is difficult and limits implementation to real world systems that have limited optical access (e.g. combustors and engines). The HRR LI technique demonstrated here has per-pulse energy requirements ~10 times lower than the traditional single-pulse LI technique allowing for delivery through standard commercial optical fibers. Additionally, the HRR LI approach significantly increases the ignition probability of lean combustible mixtures in high-speed flows while maintaining low per-pulse energies.

Introduction

Laser ignition (LI) is an advanced ignition method that has several advantages over traditional electric spark plugs and gaseous torches for fuel-lean, high-pressure ignition environments [1-5]. It also provides precise ignition timing, large penetration depth, and ignition at desired location(s) for optimal combustion performance. LI has been used for a wide variety of applications, including ignition of gaseous fuels for internal-combustion engines [6] and rocket engines [7] and initiation of nuclear fission/fusion reactions [8]. There is particular interest in the use of LI for stationary gas engines owing to the possibility of increased engine efficiency and reduced NOx emission [5]. Additionally, there is interest in using laser sparks for ignition of aircraft gas turbine engines to achieve rapid relight [9].

Among the available LI methods, the non-resonant breakdown LI technique has been the most widely used because of its simplicity in implementation and rapid ignition [1-5]. In the Non-resonant breakdown LI process, seed electrons are generated through the non-resonant, multi-photon ionization process using a high-intensity laser pulse (intensity must exceed the air-breakdown threshold ~10^{11} W/cm^2). Subsequently, the electrons are accelerated via the inverse-bremsstrahlung process with the same intense pulse. Collisions between these accelerated electrons and other molecules liberate additional electrons and induce an electron avalanche that forms a laser-induced plasma. Joule heating of the surrounding combustible gaseous mixture and the production of highly reactive chemical intermediates leads to localized thermal runaway. Non-resonant LI pulse energy [i.e, minimum ignition energy (MIE)] varies with the applications but, in general, is ~10-20 mJ/pulse for natural-gas engines [10] and ~30-60 mJ/pulse for aero-turbine engines [11]. The MIE increases significantly when the fuel/air mixture becomes lean (i.e., equivalence ratio φ <0.7) [1-3, 11]. Additionally, the MIE increases with flow rate and flow turbulence level [12].

This conventional LI technique faces stiff challenges when implemented in practical engines and combustion devices where optical access is typically limited. During the past decade, researchers attempted to develop a fiber-optic beam-delivery system for LI [13-19]. However, because of the high-energy requirements for conventional LI, it remains difficult to deliver the required laser beam through flexible optical fibers for practical engine applications. A solid-core silica fiber with large core size (~1 mm) can transmit ~10 mJ/pulse [14-16, 20], which is barely sufficient for ignition. Hollow-core fibers, because of the absence of a solid core that enables a high damage threshold, have been used for delivering the required laser beam for ignition [15, 17]. However, since this fiber is very sensitive to bending loss, it not ideal for practical applications. Mullett et al. investigated various available fibers for LI and came to the conclusion that until significant advances in the development of optical fibers are made, the ability to reliably deliver the laser beam for single-pulse LI will be severely limited in real-world applications [15]. Recently Beaudou et al. [18] and Dumitrache et al. [19] demonstrated the delivery of high-energy laser pulses (~4 mJ/pulse of 10-ns-duration or ~30 mJ/pulse of 30-ns-duration) while maintaining high beam quality using a special hollow-core, photonic crystal fiber for ignition of a combustible mixture limited to near-stoichiometric conditions (φ ~1). In order to achieve LI in fuel lean or high speed flows, while not exceeding the fiber damage threshold, a deviation from the traditional single pulse methods may be necessary.

Osborne et al. [7] and Cheng et al. [21] report enhancement in igniting lean fuel/air mixtures using dual pulse (pulse spacing ~10-200 ns). Osborne et al. showed that extension of the laser spark lifetime and optimization of the local energy deposition are highly dependent on delays between two pulses [7]. Zhang et al. [22] showed that in atmospheric-pressure air, plasma enhancement can be achieved with two pulses that are separated by > 50 μs.

In the present study, we demonstrate LI of combustible gaseous mixtures with order-of-magnitude reduction in per-pulse energy can be achieved using a high-repetition-rate (HRR) nanosecond laser pulse train. The HRR pulses are generated from a Nd:YAG-based burst-mode laser (Quasimodo, Spectral Energies).[23] The HRR (10-100 kHz) laser pulse train induces a weakly-ionized plasma typically within the first few pulses. The subsequent laser pulses enhance the plasma through energy deposition and leads to sustained ignition. Generally, this approach can be viewed as an extension of the dual pulse technique with the number of pulses easily changeable from a few to multiple of tens. The HRR LI approach increases the ignition probability of lean combustible mixtures in high-speed flows while maintaining low individual pulse energies.

Experimental Setup

Figure 19 displays the experimental setup used for laser ignition of isobutane/air and ethylene/air pre-mixed flows from a Hencken burner at atmospheric-pressure. The second harmonic of the burst-mode laser generated 10-ns laser pulses at various repetition rates (10 kHz-100 kHz). The laser beam with a beam diameter of ~6 mm was focused to the center of the Hencken burner using a spherical lens with a focal length of *f* = 50 mm and a diameter of 50.8 mm. The beam waist at the focal point was measured by a beam profiler (Spiricon, LW230); the typical beam waist at the focus was ~ 60 μm. To understand the laser-plasma interaction during the laser ignition process, the generated plasma (i.e., free electrons) was detected by coherent microwave scattering [22]. Additionally, a high-speed camera (Photron SA-Z, at up to 100,000 frames per second) that was equipped with an intensifier (LaVision IRO) was used to track the chemiluminescence from the flame-ignition and flame-propagation events. OH* chemiluminescence was collected around 310 nm with a Cerco UV 45-mm, f/1.8 lens. A narrow bandpass interference filter (Semrock, FF01-3080/10-25) was placed on the imaging lens. OH* chemiluminescence was utilized to identify the flame reaction zone and capture the flame front and propagation. The 2-D OH* chemiluminescence images were acquired with a ~ 2 μs exposure time. Ignition delays and reaction times can also be determined from the same measurements.

Results and Discussion

Figure 20 shows the coherent microwave scattering from a weakly-ionized laser-induced plasma formed in air by a 10-kHz pulse train and the pulse energy distribution of said pulse train. To avoid saturating the microwave detector, we intentionally placed the detector at a distance from the laser-induced spark location. Hence, the weak plasma created by the laser pulses during the first 2 ms (~20 pulses) is not detectable. The first few pulses generated the weakly-ionized plasma. Because the plasma lifetime at atmospheric pressure is ~100 μs and larger than the temporal spacing of the 10-kHz pulse train [22], the plasma is greatly enhanced by the subsequent pulses. Generally this enhancement is shown by the increase in the microwave peaks with superimposed oscillations over the time span of the pulse train. These oscillations are most likely due to small fluctuations in the plasma position due to ambient air flow in the room. The enhanced plasma heats the surrounding gas and most likely forms highly reactive chemical intermediates. When such a plasma is formed in a combustible gaseous mixtures this can lead to localized thermal runaway and ignition.

Figure 21 shows a comparison of laser ignition in a combustible mixture using a single pulse (i.e., 10-Hz laser) and HRR pulses [i.e., pulse repetition rate (PRR) of 10 kHz and 20 kHz). This figure displays the temporally resolved images of OH* chemiluminescence from a typical ignition of an isobutane/air mixture above a Hencken burner using a standard 10-Hz laser and the burst-mode laser operated at 10-kHz and 20-kHz repetition rate. The flow and beam conditions (i.e., focused beam diameter, fuel/air mixture, and flow rate) are consistent for all three cases. The pulse energy used for ignition for the 10-Hz laser, 10-kHz laser, and 20-kHz laser was ~30 mJ/pulse, ~3 mJ/pulse, and ~2.8 mJ/pulse, respectively. For 10-Hz laser ignition, a high per-pulse energy is required to generate a plasma (bright emission spot shown in 10 Hz-figure) for heating the surrounding fuel/air mixture and initiating the ignition process. It was found that the hot plasma is quickly quenched within ~0.1 ms. The third to the fifth images show a flame front evolution that is highly similar to an outwardly propagating spherical flame. For 10-kHz and 20-kHz laser ignition, each individual pulse energy is ~ 10 times weaker than that used for 10-Hz laser ignition. We have verified that with a 10-Hz laser, the pulse energy < 5 mJ/pulse generates a weakly-ionized plasma that cannot initiate the ignition process. The emission from the plasma created by the low-energy laser pulse is weak; therefore, after attenuation by the OH* band-pass filter, the emission cannot be detected by the intensified camera. For both 10-kHz and 20-kHz cases, it was observed that a weakly-ionized plasma was created after three to four consecutive laser pulses. It was observed that once the plasma was created, the subsequent HRR laser pulses could sustain them. The lifetime of the plasma was characterized by strong emissions using the intensified camera. T 10-kHz laser and the 20-kHz laser is ~0.2 ms and ~0.3 ms, respectively. For all of the cases, the premixed flame finally stabilized on the burner surface after ~7 ms.

Figure 22(a) shows the minimum ignition energy (MIE) as a function of pulse repetition frequency for the ignition of isobutane/air mixtures with equivalence ratio φ= 1 at atmospheric pressure. At 10 Hz the ns lasers have a very high MIE of ~30 mJ/pulse. It is observed that the MIE decreases with an increase in PRR. When PRR increases from 10 Hz to 10 kHz, the MIE decreases an order of magnitude. Particularly, the MIE decreases ~10-12 times for PRR in the range 10-100 kHz. We also noticed that the laser-energy absorption by plasma increases from ~12% to ~40% when PRR increases from 10-Hz to 10-kHz (incident laser energy remains at ~3 mJ/pulse). This indicates that the HRR pulse-train approach can more efficiently deposit laser energy to the plasma. Figure 22(b) shows that the HRR laser-ignition approach can maintain the same energy per pulse across a wide equivalence-ratio range (φ =0.65-1.2, ethylene/air mixture). The energy per pulse decreases ~10 times for the HRR LI approach as compared to 10-Hz-pulsed LI (φ=0.65-1.2). The limitation of this approach is that the per pulse energy must be greater than that needed for laser induced breakdown of the mixture. This is most likely causing the MIE of HRR LI to asymptotically approach the breakdown threshold energy of the mixture.

Ignition in high-speed flows is often challenging because of increased convective heat losses. Figure 23 shows the ignition probability of an isobutane/oxygen/nitrogen mixture by various pulse trains at different repetition rates while maintaining the same per-pulse energy of ~ 1.5 mJ/pulse. Clearly, an increase of repetition rate can increase the ignition probability for higher flow speeds. This is most likely due to the plasma enhancement over the pulse. It should be noted that for this test, we were able to ignite the isobutane/air mixture with HRR pulses; however, the flame could not be sustained because the flow speed was faster than the isobutane flame speed (~0.3 m/s).

In summary, we have demonstrated that the HRR LI approach has significantly lower per-pulse energy requirements for ignition of combustible gaseous mixtures, as compared to the traditional single-pulse LI approach. Approximately an order-of-magnitude reduction for the ignition threshold energy (per pulse) was achieved. The HRR LI technique utilizes laser beams with per-pulse energies that will not damage standard commercial multimode and hollow-core fibers. Additionally, we demonstrated that the plasma enhancement from HRR LI technique can increase the ignition probability of lean and/or high-speed flows of an isobutane/air mixture while maintaining low individual pulse energies. A similar phenomenon may be achievable with other temporally separated muli-beam techniques such as double pulse. By reducing the burst duration those techniques are approached.

Future work will focus on HRR LI at elevated pressures. The enhanced plasma quenching due to collisions at elevated will lead to shorter plasma lifetimes; thus, it is expected that the PRR should increased to achieve efficient energy deposition. We have verified experimentally that the overall plasma lifetime in air at 40-bars is ~ 30 μs. Therefore, in principle, a HRR pulse train with 50-kHz repetition rate (i.e., 20-μs pulse interval) could be efficiently applied for ignition at high pressure.

Acknowledgements

The authors gratefully acknowledge useful discussions with Dr. Anil K. Patnaik of the Air Force Research Laboratory (AFRL). Funding for this research was provided by the AFRL under Contract Nos. FA9101-14-M-0011.

References

1. Bradley, D., et al., *Fundamentals of high-energy spark ignition with lasers.* Combustion and Flame, 2004. **138**(1): p. 55-77.

2. Phuoc, T.X., *Laser-induced spark ignition fundamental and applications.* Optics and Lasers in Engineering, 2006. **44**(5): p. 351-397.

3. Tauer, J., H. Kofler, and E. Wintner, *Laser-initiated ignition.* Laser & Photonics Reviews, 2010. **4**(1): p. 99-122.

4. Dearden, G. and T. Shenton, *Laser ignited engines: progress, challenges and prospects.* Optics express, 2013. **21**(106): p. A1113-A1125.

5. Ronney, P.D., *Laser versus conventional ignition of flames.* Optical Engineering, 1994. **33**(2): p. 510-521.

6. Dale, J., P. Smy, and R. Clements, *Laser ignited internal combustion engine-an experimental study*. 1978, SAE Technical Paper.

7. Osborne, R.J., et al., 'Evaluation and Characterization Study of Dual Pulse Laser-Induced Spark (DPLIS) for Rocket Engine Ignition System Application. Powered Flight- The Next Century, 2003.

8. Hurricane, O., et al., Fuel gain exceeding unity in an inertially confined fusion implosion. Nature, 2014. **506**(7488): p. 343-348.

9. Oldenborg, R., J. Early, and C. Lester, *Advanced ignition and propulsion technology program*. 1998, Los Alamos National Lab., NM (US).

10. Kopecek, H., et al., Laser-induced ignition of methane-air mixtures at pressures up to 4 MPa. Laser physics, 2003. **13**(11): p. 1365-1369.

11. El-Rabii, H., et al., *Laser spark ignition of two-phase monodisperse mixtures.* Optics communications, 2005. **256**(4): p. 495-506.

12. Weinrotter, M., et al., *Laser ignition of ultra-lean methane/hydrogen/air mixtures at high temperature and pressure.* Experimental Thermal and Fluid Science, 2005. **29**(5): p. 569-577.

13. Yalin, A.P., *High power fiber delivery for laser ignition applications.* Optics express, 2013. **21**(106): p. A1102-A1112.

14. El-Rabii, H. and G. Gaborel, *Laser ignition of flammable mixtures via a solid core optical fiber.* Applied Physics B, 2007. **87**(1): p. 139-144.

15. Mullett, J., et al., *A comparative study of optical fibre types for application in a laser-induced ignition system.* Journal of Optics A: Pure and Applied Optics, 2009. **11**(5): p. 054007.

16. Joshi, S., N. Wilvert, and A.P. Yalin, *Delivery of high intensity beams with large clad step-index fibers for engine ignition.* Applied Physics B, 2012. **108**(4): p. 925-932.

17. Joshi, S., A.P. Yalin, and A. Galvanauskas, Use of hollow core fibers, fiber lasers, and photonic crystal fibers for spark delivery and laser ignition in gases. Applied optics, 2007. **46**(19): p. 4057-4064.

18. Beaudou, B., et al., Millijoule laser pulse delivery for spark ignition through kagome hollow-core fiber. Optics letters, 2012. **37**(9): p. 1430-1432.

19. Dumitrache, C., J. Rath, and A.P. Yalin, *High power spark delivery system using hollow core kagome lattice fibers.* Materials, 2014. **7**(8): p. 5700-5710.

20. Hsu, P.S., et al., Investigation of optical fibers for coherent anti-Stokes Raman scattering (CARS) spectroscopy in reacting flows. Experiments in fluids, 2010. **49**(4): p. 969-984.

21. Cheng, H., et al. Multiple Pulse Laser Ignition Control Application in GDI Lean Combustion. in Laser Ignition Conference. 2015. Optical Society of America.

22. Zhang, Z., M.N. Shneider, and R.B. Miles, *Microwave diagnostics of laser-induced avalanche ionization in air*. Journal of applied physics, 2006. **100**(7): p. 074912.

23. Slipchenko, M.N., et al., *Quasi-continuous burst-mode laser for high-speed planar imaging*. Optics letters, 2012. **37**(8): p. 1346-1348.

Appendix

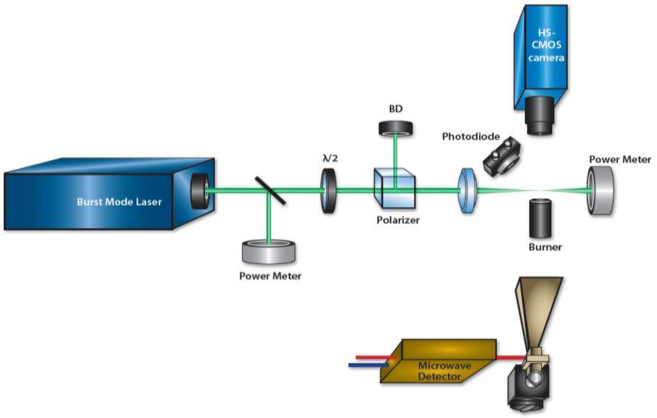

Figure 19. Schematic view of the experimental setup for laser ignition in Hencken burner.

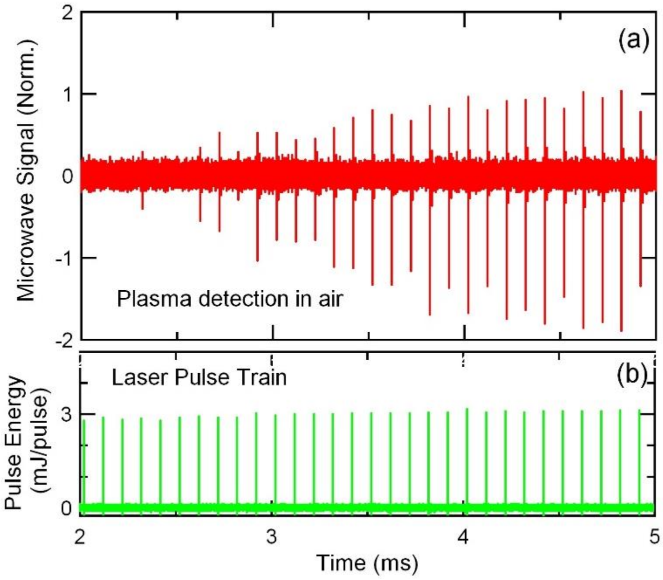

Figure 20. (a) Normalized microwave scattering and photodiode signals within a 532-nm, 10-kHz pulse train;. data were taken in the air. (b) Corresponding excitation pulse energy.

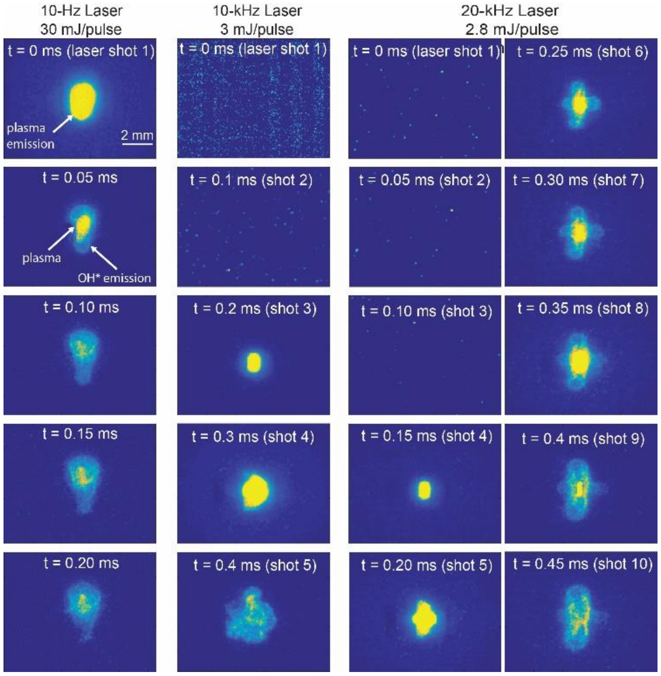

Figure 21. Laser ignition in isobutane/air mixture at equivalence ratio φ=1 using 10-Hz laser (single laser shot) and HRR laser (10-kHz and 20-kHz repetition rate). Ignition-core evolution in isobutane/air mixture above Hencken burner was tracked by monitoring OH* chemiluminescence.

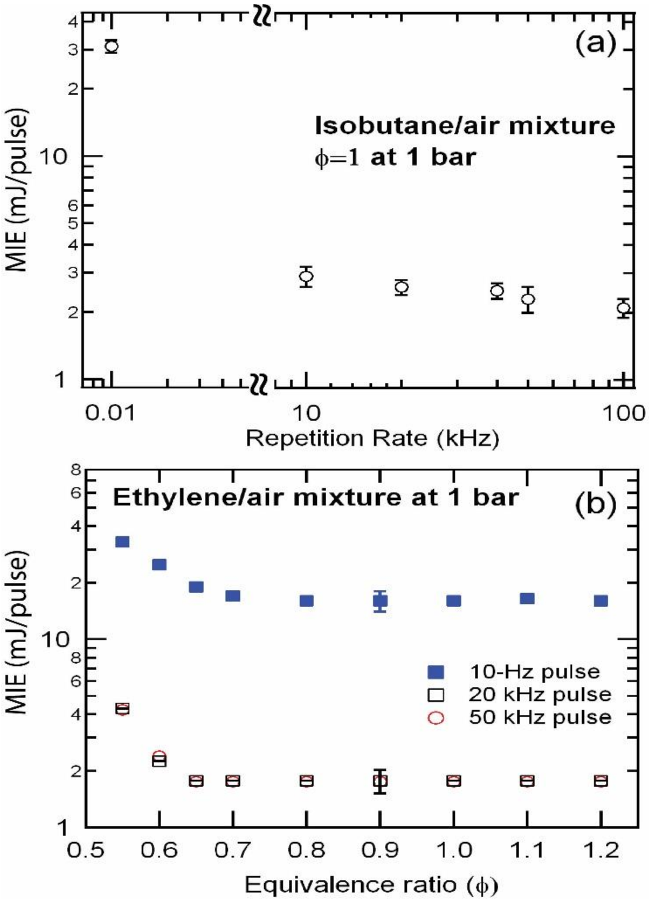

Figure 22. (a) MIE (input energy) as a function of repetition frequency. Isobutane/air mixture of φ=1 at atmospheric pressure. (b) MIE as a function of equivalence ratio for ethylene/air mixture at atmospheric pressure. The burst duration for all HRR pulses is 0.5 ms.

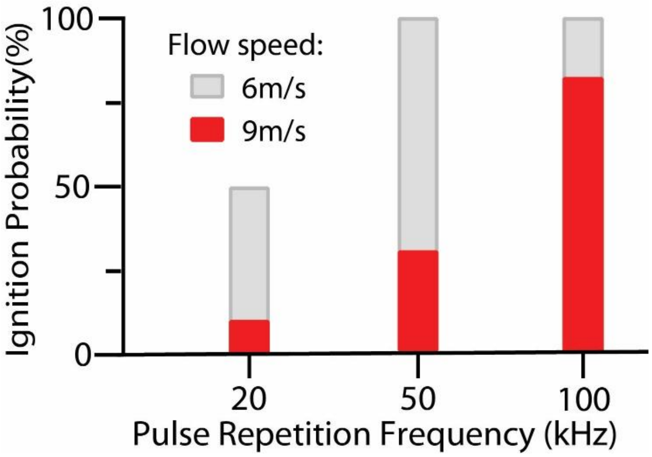

Figure 23. Ignition probabilities of isobutane/oxygen/nitrogen mixtures for 10-ns pulse train with various repetition frequencies at various flow speeds. The probability for flow speed of 6 m/s and 9 m/s is shown in gray and red, respectively. Each pulse energy and burst duration was maintained at ~1.5 mJ/pulse and 1 ms, respectively.

CHAPTER IV

SODIUM CLUSTER ION RECOMBINATION RATE MEASUREMENTS BY RADAR REMPI

This article, “Sodium Cluster Ion Recombination Rate Measurements by Radar REMPI”, was presented at the 52nd AIAA Aerospace Sciences Meeting on the 16th of January 2014 and published online later in 2014.

Author affiliations:

Jordan Sawyer[1], Yue Wu[1], Zhili Zhang[1], and Albert A. Viggiano[2]

[1]Department of Mechanical, Aerospace and Biomedical Engineering, University of Tennessee, Knoxville TN 37996, USA

[2]Air Force Research Laboratory, Space Vehicles Directorate, Kirtland Air Force Base, New Mexico 87117,USA

Sawyer, J., et al., Sodium Cluster Ion Recombination Rate Measurements by Radar REMPI, in 52nd Aerospace Sciences Meeting. 2014, American Institute of Aeronautics and Astronautics.

Abstract

This paper presents non-intrusive measurements of sodium-argon and sodium-nitrogen cluster ion recombination with electrons based on coherent microwave scattering (Radar) from Resonance Enhanced Multi-Photon Ionization (REMPI). The number density of sodium, in a mixture of sodium vapor with argon or nitrogen buffer gas, was determined by direct absorption measurement. Sodium was resonantly ionized by a tunable laser beam in the 2+1 REMPI process. Since the plasma is mainly made of sodium ions in the mixture, the sodium ion clusters are thus formed by the Chaperone process. The dissociative recombination rate of sodium-argon and sodium-nitrogen and the neutral stabilized recombination rate of sodium ions were determined from a least-squares Monte Carlo algorithm (LSM) that fitted the plasma dynamic model to the direct measurement of the total electron number in the laser-induced plasma. At 300°C, $\mathrm{n_{Na}} = 5.79 \times 10^{11}/\mathrm{cm}^3$ and $\mathrm{P_{Ar}} = 100\,\mathrm{Torr}$, the dissociative recombination rate of $\mathrm{Na^{+}{\cdot}(Ar)}$ was

determined to be $\beta_{dr} = 5.42 \times 10^{-7} cm^3/s$ and the neutral stabilized recombination rate was determined to be $\beta_{3N} = 1.26 \times 10^{-26} cm^6/s$. At 300°C, $n_{Na} = 3.22 \times 10^{11}/cm^3$ and $P_{N_2} = 100$ Torr, the dissociative recombination rate of $Na^+ \cdot (N_2)$ was determined to be $\beta_{dr} = 1.31 \times 10^{-7} cm^3/s$ and the neutral stabilized recombination rate was determined to be $\beta_{3N} = 6.1 \times 10^{-26} cm^6/s$ .The method can be easily extended to measurements of other cluster ion species over a wide range of temperatures and pressures in various mixture compositions, such as Mg and Ca with N_2 and CO_2. The results are of fundamental importance to the plasma chemistry field and hypersonic research. The present model does not take into account the backwards reaction of cluster ion formation which makes the presented at best a rough estimate.

Introduction

The unique combination of the relatively low ionization potential of alkali metals and the high temperatures behind the bow shock of a hypersonic vehicle in flight allows for rapid vaporization and thermal ionization of alkali metals.[1] Studies have shown that the electrical conductivity of the flow near the surface of a hypersonic vehicle can be augmented by seeding the flow with alkali metals. This in turn would allow for better control of a hypersonic vehicle by magnetohydrodynamics (MHD).[2, 3] Additionally, hypersonic and atmospheric reentry vehicles have a fair amount of alkali metal impurities in the vehicle surface. During the course of hypersonic flight or atmospheric reentry a significant amount of these impurities are inevitably vaporized and ionized in the flow.[2-8] These alkali cations play a significant role in the formation of the plasma within the vehicle's boundary ("plasma sheath"). The plasma sheath leads to many adverse changes in the vehicle's communication and navigation capabilities such as loss of telemetry, GPS, and radio "blackout".[9, 10] Also, the plasma sheath can lead to significant effects in the vehicle's aerodynamic performance, stability, and thermal protection system.[8, 11, 12] Developing a better understanding of the fundamental plasma chemistry involved in the recombination processes for alkali metal ions is of vital importance to hypersonic and plasma dynamic research.

Alkali metal cations generally have a low radiative recombination rate. Thus at higher pressures in atmospheric gases, such as those around a hypersonic vehicle, the plasma neutralizations is controlled primarily by three-body processes.[13] These processes include electron (e^- as the third body) and neutral stabilized collisions as well as chaperone mechanisms. The lack of knowledge of these processes is heavily due to the difficulty to make quantitative measurements of the recombination rates. Past measurements have involved techniques such as ion storage rings, stationary afterglow (SA), and flow afterglow (FA). The main drawbacks of these techniques come in the form of a limited range of experimental pressures and temperatures. Additionally, all of these techniques use ionization methods that lead to ions others than those that are desired, which naturally complicates the overall chemistry. Primarily, Penning ionization of Ar by a He microwave discharge is used in these apparatuses.

In this work, coherent microwave scattering (Radar) from Resonance Enhanced Multi-Photon Ionization (REMPI) is utilized for the measurement of sodium ion neutral stabilized and cluster dissociative recombination rates. The separation of the ionization and detection mechanisms greatly simplifies the experimental procedure. Radar REMPI as a stationary technique allows for a wide range of experimental temperatures and pressures including those above atmospheric conditions.[14-18] REMPI allows for selective ionization of the sodium and minimizes all other cation species generated in the plasma. Coherent microwave scattering from the electrons in the decaying plasma allows in-situ measurement throughout time without extracting electrons or cations. Recombination rates were then deduced using a least-squares Monte Carlo algorithm (LSM). Neutral stabilized recombination rates for sodium ions in argon and nitrogen buffer gases along with the dissociative recombination rates of sodium-argon and sodium-nitrogen cluster ions are presented here.

Sodium Number Density Measurement

Absorption Theory

The attenuation of a beam of light as it passes through an absorbing medium is described by the Beer-Lambert law. The Beer-Lambert law relates the exponential decay of the intensity of the light to the absorption coefficient, α, and the optical path length, l, as

$$\frac{I}{I_0} = e^{-\alpha l} \qquad (1)$$

where I_0 and I are the total and transmitted intensities of the light, respectively. The absorption coefficient of the media is given by

$$\alpha = n\sigma$$

(2)

where n is the number density of the absorbers in the media and σ is their optical cross sections. The cross section, $\sigma(\omega)$, depends on transition properties between an upper and lower state given by

$$\sigma(\omega) = \frac{1}{4}\left(\frac{g_2}{g_1}\right)\lambda_{21}^2 g(\omega) A_{21}$$

(3)

where A_{21} is the Einstein spontaneous emission coefficient, λ_{21} is the absorption line wavelength of the absorbed photon, and g_1 and g_2 are the degeneracy of the lower and upper levels.

In a mixture of the buffer gas and the vaporized sodium the line shape functions $g(\omega)$ of the sodium absorption lines are complicated by both self-broadening collisions and foreign gas collisions. Additionally, radiation trapping is present. The line widths, Γ, due to self-broadening and foreign gas collisions depend on the broadening rate coefficients $k_{\mathrm{C}}^{\mathrm{self}}$ and $k_{\mathrm{C}}^{\mathrm{Ar}}$, the number density of sodium vapor n_{Na} and foreign gas n_{Ar} are given by

$$\Gamma_{\mathrm{C}}^{\mathrm{self}} = \mathrm{n}_{\mathrm{Na}} \cdot \mathrm{k}_{\mathrm{C}}^{\mathrm{self}} \qquad (4)$$

$$\Gamma_{\mathrm{C}}^{\mathrm{Ar}} = \mathrm{n}_{\mathrm{Ar}} \cdot \mathrm{k}_{\mathrm{C}}^{\mathrm{Ar}} \qquad (5)$$

The total collisional-broadening rate, Γ_{c}, can be expressed as the sum of self-broadening and foreign-gas broadening given by

$$\Gamma_{\mathrm{C}} = \Gamma_{\mathrm{C}}^{\mathrm{self}} + \Gamma_{\mathrm{C}}^{\mathrm{Ar}} = \mathrm{n}_{\mathrm{Na}} \cdot \mathrm{k}_{\mathrm{C}}^{\mathrm{self}} + \mathrm{n}_{\mathrm{Ar}} \cdot \mathrm{k}_{\mathrm{C}}^{\mathrm{Ar}} \qquad (6)$$

An equivalent line width for collisional and natural broadening may then be expressed as

$$\mathrm{W}_{\lambda} = \frac{\lambda^2}{\mathrm{c}}\left(\frac{\lambda^2}{8\pi^2}\frac{\mathrm{g}_2}{\mathrm{g}_1}\ln(\Gamma_{\mathrm{C}}\Gamma_{\mathrm{natural}})\right)^{\frac{1}{2}} \qquad (7)$$

A convolution of the effects of natural broadening, Doppler broadening, collisional-broadening and the laser line shape give the line shape function $g(\omega)$. The resulting line shape is a Voigt profile because of the convolution of the Gaussian profile of the laser light pulse and Doppler broadening with the Lorentzian profile of collisional broadening and natural broadening. A Voigt profile may be calculated by the Whitening approximation given by

$$\frac{I_{\lambda}}{I_{\lambda_{GL}}} = \left[1 - \frac{w_l}{w_v}\right]\exp^{-4\ln 2\left(\frac{\lambda-\lambda_{12}}{w_v}\right)^2} + \left[\frac{w_l}{w_v}\right]\frac{1}{1+4\left(\frac{\lambda-\lambda_{12}}{w_v}\right)^2} + 0.016\left[1-\frac{w_l}{w_v}\right]\left[\frac{w_l}{w_v}\right]\left\{\exp^{-0.4\left(\frac{\lambda-\lambda_{12}}{w_v}\right)^{2.25}} - \frac{10}{10+\left(\frac{\lambda-\lambda_{12}}{w_v}\right)^{2.25}}\right\} \qquad (8)$$

$$w_v = \frac{w_l}{2} + \sqrt{\left(\frac{w_l^2}{4} + w_g^2\right)}$$

$$I_{\lambda_{GL}} = \frac{1}{w_v[1.065 + 0.447(w_l / w_v) + 0.058(w_l / w_v)^2]}$$

where w_g and w_l are the linewidth (FWHM) of Gaussian profile and Lorentzian profile respectively, is the linewidth of Voigt profile, and $I_{\lambda_{GL}}$ is the normalization factor of the Voigt profile. Table 1 gives the various parameters needed to calculate the absorption cross section of a standard Voigt profile, with the laser linewidth (FWHM) at 0.01nm. The higher degeneracy of the excited states for the D_2 line lead to a larger absorption cross section (and consequently greater absorption) in comparison to the D_1 line.

Experimental Measurements

Figure 24 shows a schematic of the experimental setup used for the sodium absorption measurements. The second harmonic of a Nd:YAG laser was used to pump a dye laser, with Rhodamine 6G as the dye. The laser power was reduced by irises to eliminate any nonlinear optical effects and saturation of the photodiodes. The tunable output beam of the dye laser was partially reflected by a mirror and passed through an iris before arriving at a photodiode (PD1). The remainder of the beam passed through an iris and quartz cell filled with a mixture of sodium vapor and the buffer gas. The attenuated beam then passed through an iris before arriving at the second photodiode (PD2). The temperature inside of the furnace was regulated by a PID controller that controlled the current to a concrete block heater and received feedback from a thermocouple. The system had an accuracy of ±1K. The sodium number density in the cell was regulated by a pump that was used to reduce the sodium partial pressure to a level below sodium vapor pressure at the specified temperature. The cell was then filled with the buffer gas to a set pressure and allowed to reach equilibrium before measurement.

The output pulses from the two high speed photodiodes were recorded on an oscilloscope, and their ratio as the frequency was scanned through gave the absorption spectrum. The laser wavelength was calibrated by the sodium observed sodium D_1 and D_2. The sodium number density was found by means of a least squares algorithm used to fit the simulated spectra. Figure 25 shows two measured absorption spectra with their corresponding least squares fit from simulation. The first spectrum corresponds to a mixture of 5.79E11 cm^{-3} sodium vapor with 100 Torr argon at 300 ^{o}C. The second spectrum corresponds to a mixture of 3.22E11 cm^{-3} sodium vapor with 100 Torr nitrogen at 300 ^{o}C. The change in buffer gas from argon to nitrogen appeared to result in relatively negligible changes in the absorption spectrum so the properties given in Table 1. Properties of sodium D1 and D2 lines from NIST were used for both fitting routines. The laser linewidth (FWHM) was measured to be about 0.006 nm during all experiments.

Sodium Cluster Ion Generation

Sodium density was measured every time before generating sodium cluster ions. The same laser system, with the addition of a focusing lens, as shown in Figure 24 was used to generate Resonance Enhanced Multi-Photon Ionization (REMPI) of the sodium atoms in the mixture of sodium vapor and buffer gas in the cell. The second harmonic (532 nm) was used to pump a dye laser (Rhodamine 6G as the dye). The dye laser output was roughly 3 mJ/pulse with a pulse width of 8 ns. The laser beam was split with a small portion going to a photodiode (PD1). The photodiode (PD1) was used to trigger the microwave data acquisition system as well as monitor the laser power over the course of experiments. The remainder was focused by a 10 cm focal length plano-convex lens. Gaussian beam calculations give an estimation of roughly a 15 μm for the focal spot size. The laser frequency was tunned near the REMPI peak to achieve variable ionization of the sodium atoms. The experimental setup can be seen in Figure 26.

A microwave homodyne system was used to detect the REMPI plasma.[17] A 10 dBm tunable microwave source (HP 8350B sweep oscillator, set at ~10 GHz) was first split into two channels. One was used to illuminate the ionization point through a microwave horn (WR75, 15dB gain). Microwave scattering from the plasma was collected by the same microwave horn. The received microwave passed through a microwave circulator and was amplified 30 dB by one preamplifier at ~10 GHz. After the frequency was converted down in the mixer, two other amplifiers with bandwidth of 2.5 KHz to 1.0 GHz amplified the signal by another factor of 60dB. From the geometry of dipole radiation, the polarization of the microwave was chosen to be along the propagation direction of the laser to maximize the scattering signal. The time-accurate microwave scattering signal was monitored by an oscilloscope. The microwave signal was also input into an automatic data acquisition system, which recorded the REMPI spectrum as the laser was tuned. A more detailed description of the microwave system can be found in previous publications.

Figure 27 shows the 2+1 REMPI spectrum of sodium by measured by coherent microwave scattering immediately following the laser pulse. Figure 27 was obtained for a mixture of sodium vapor and nitrogen buffer gas at 350℃ and 100 Torr. Laser was scanned from 578.45 nm to 578.85 nm at 0.001nm per second. Averaging of the microwave signal can result in better signal to noise ratio for the spectrum. Spectra were obtained for the sodium at different number densities and buffer gas composition, temperatures, and pressures. In each measurement negligible signal was seen far from the REMPI peak. Thus very little direct ionization of the buffer gas and sodium occurred during experimentation. Sodium can be efficiently ionized by the REMPI process even if the conditions of the mixtures, such as sodium number density, temperature, pressure of the buffer gases, drastically change. The sodium REMPI spectra do not depend on pressure of buffer gases and sodium number density.

Plasma Dynamic Modeling

In this work, a partially ionized plasma of sodium and argon, which consists of neutrals, electrons, ions and molecular ions, is modeled. The model begins at the end of the 8 ns where we assume that the ions in the plasma consist entirely of sodium cations. Table 2 shows the reactions used in the model along with their corresponding rate constants. The reactions include radiative, electron stabilized, neutral stabilized, and dissociative recombination along with ion cluster conversion and switching with the buffer gas and water vapor. Diffusion was reasonably assumed to be dominated by ambipolar diffusion. The diffusion coefficient was based on sodium ion nobilities of 3.4E-4 and 3.23E-4 ($m^2/s*V$) in ATP nitrogen and argon buffer gases, respectively.[19] The ion mobility at the experimental pressure and temperature was obtained by gas kinetic theory. Ambipolar diffusion was treated as a first order loss mechanism. The rate constants for neutral stabilized recombination, β_{3N}, and dissociative recombination, β_{dr}, are unknown. The determination of the β_{3N} and β_{dr} values is the goal of this work.

Rate equations for four species were obtained from the reactions listed in Table 2. The rate equations are given below in equations (9-12) with neutral buffer gas specie denoted by M (Ar or N_2) and buffer gas cluster ion denoted by C ($Na^+ \cdot Ar$ or $Na^+ \cdot N_2$). Rate constants for known but unreferenced reactions were taken to be similar to those of similar reactions. The number densities of electrons n_e, sodium cations n_{Na+}, sodium ion clusters with the neutral buffer gas n_{NaM+}, and sodium clusters with water vapor n_{NaH2O+} were obtained by the solution of this system of odes. Initial concentrations are based on the assumption that sodium is fully ionized. Therefore $n_e(t = 0) = n_{Na^+}(t = 0) = n_{Na}$, where n_{Na} is the sodium number density obtained from the absorption measurement. Also, the initial concentration of the sodium cluster ions is taken to be zero. An impurity of 10 ppm water vapor was assumed in all calculations.

$$\frac{dn_e}{dt} = -k_1 n_e n_{Na^+} - \beta_{3N} n_M n_e n_{Na^+} - \beta_{3e} n_e n_e n_{Na^+} - \beta_{dr} n_e n_C - k_8 n_e n_{NaH_2O^+} - D_a n_e \tag{9}$$

$$\frac{dn_{Na^+}}{dt} = -k_1 n_e n_{Na^+} - \beta_{3N} n_M n_e n_{Na^+} - \beta_{3e} n_e n_e n_{Na^+} - k_{conv} n_{Na^+} n_M n_M - k_6 n_{Na^+}\left(n_{H_2O} - n_{NaH_2O^+}\right) n_M$$

$$-D_a n_e \cdot \frac{n_{Na^+}}{n_{Na^+} + n_C + n_{NaH_2O^+}} \tag{10}$$

$$\frac{dn_C}{dt} = -\beta_{dr} n_e n_C + k_{conv} n_{Na^+} n_M n_M - k_7 n_C\left(n_{H_2O} - n_{NaH_2O^+}\right) - D_a n_e \cdot \frac{n_C}{n_{Na^+} + n_C + n_{NaH_2O^+}} \tag{11}$$

$$\frac{dn_{NaH_2O^+}}{dt} = -\beta_{dr} n_e n_C + k_{conv} n_{Na^+} n_M n_M + k_7 n_C\left(n_{H_2O} - n_{NaH_2O^+}\right) + k_6 n_{Na^+}\left(n_{H_2O} - n_{NaH_2O^+}\right) n_M$$

$$-D_a n_e \cdot \frac{n_{NaH_2O^+}}{n_{Na^+} + n_C + n_{NaH_2O^+}} \tag{12}$$

Sodium Cluster Ion Recombination Rate Characterization

A least-squares Monte Carlo algorithm (LSM) was used to optimize the “fit” of the simulated electron number density to the total electron number density curve from direct measurement of coherent microwave scattering. The algorithm optimized this fit by manipulating the β_{3N} and β_{dr} rate constants within specified bounds. One hundred random initial guesses were made for these values within a range of four orders of magnitude on each variable. Only the first 40 microseconds of the plasma decay was simulated. On longer time scales the volume of the plasma expanded to a volume much larger than the focal size of the laser. The electron number density will also be significantly lower than at the end of the laser pulse. These two factors may lead to a breakdown of the 0D model and nullify coherent microwave scattering as an accurate diagnostic technique. Figure 28 and Figure 29 show a comparison of the measured and “fitted” simulation electron number density curves for the first 40 microseconds after the laser pulse. Figure 28 corresponds to a mixture of $n_{Na} = 5.79 \times 10^{11}/cm^3$ in a Ar buffer gas at 100 Torr and 300 ^{o}C. The LSM algorithm found the dissociative recombination rate of to be $\beta_{dr} = 5.42 \times 10^{-7} cm^3/s$ and the neutral stabilized recombination rate to be $\beta_{3N} = 1.26 \times 10^{-26} \mathrm{cm}^6/\mathrm{s}$ at these conditions. Figure 29 corresponds to a mixture of $n_{Na} = 3.22 \times 10^{11}/\mathrm{cm}^3$ in a N_2 buffer gas at 100 Torr and 300 °C. The dissociative recombination rate was determined to be $\beta_{dr} = 1.31 \times 10^{-7} \mathrm{cm}^3/\mathrm{s}$ and the neutral stabilized recombination rate was determined to be $\beta_{3N} = 6.1 \times 10^{-26} \mathrm{cm}^6/s$. Figure 30 and Figure 31 show the simulated electron, sodium cation, and sodium cluster ion number density curves for these conditions for argon and nitrogen buffer gases, respectively.

microseconds of plasma decay in a Ar buffer gas at 100 Torr and 300°C with nNa=5.79 × 1011/cm3.

microseconds of plasma decay in a N_2 buffer gas at 100 Torr and 300°C with nNa=3.22 × 1011/cm3.

for the first 40 microseconds of plasma decay in a Ar buffer gas at 100 Torr and 300°C with nNa=5.79 × 1011/cm3.

for the first 40 microseconds of plasma decay in a N_2 buffer gas at 100 Torr and 300°C with nNa=3.22 × 1011/cm3.

Conclusions

The sodium number density in the sodium vapor and buffer gas mixture was determined by the direct absorption measurements. The 2+1 REMPI process was used to generate sodium ions in a mixture of sodium vapor with argon or nitrogen. Coherent microwave scattering measurements were performed to determine the electron number density in decaying plasma throughout time. Since the plasma is mainly made of sodium ions in the mixture, the sodium argon ion clusters are thus formed by the Chaperone process. The sodium cluster ion recombination rate and neutral stabilized recombination rate were determined with the use of a least-squares Monte Carlo algorithm (LSM). The LSM algorithm fit the output of the plasma dynamic model to direct measurement of the electron number density for the first 40 microseconds after the end of the laser pulse. This method can be easily extended to other cluster ions, such as $Na^{+}\cdot(CO_2)$ and a wide range of pressures and temperatures. The results presented here are a fundamental building block for plasma chemistry and hypersonic research.

Acknowledgements

This work was supported by Kirtland Air Force Research Laboratory.

References

1. Larsson, M. and A.E. Orel, *Dissociative Recombination of Moleculear Ions*. 2008, Cambridge UK: Cambridge University Press.

2. Bisek, N.J. and J. Poggie, Exploration of MHD Flow Control for a Hypersonic Blunt Elliptic Cone with an Impregnated Ablator, in 49th AIAA Aerospace Sciences Meeting including the New Horizons Forum and Aerospace Exposition. 2011, AIAA: Orlando FL.

3. Macheret, S.O., M.N. Shneider, and G. Candler, Modeling of MHD Power Generation on Board Reentry Vehicles, in 42nd AIAA Aerospace Sciences Meeting and Exhibit. 2004, AIAA: Reno, NV. p. AIAA-2004-1024.

4. Miner, E.W. and C.H. Lewis, *Hypersonic Ionizing Air Viscous Shock-Layer Flows over Sphere Cones.* Aiaa Journal, 1975. **13**(1): p. 80-88.

5. Macheret, S.O., Weakly Ionized Plasmas in Hypersonics: Fundamental Kinetics and Flight Applications, in AIP Conference Proceedings. 2005. p. 1197-1210.

6. Shneider, M.N. and S.O. Macheret, Hypersonic Aerodynamic Control and Thrust Vectoring by Nonequilibrium Cold-Air MHD Devices, in 43rd AIAA Aerospace Sciences Meeting and Exhibit. 2005, AIAA: Reno, NV. p. AIAA-2005-979.

7. Boyd, I.D., Modeling of associative ionization reactions in hypersonic rarefied flows. Physics of Fluids, 2007. **19**(9): p. 096102.

8. Ozawa, T., J.Q. Zhong, and D.A. Levin, Development of kinetic-based energy exchange models for noncontinuum, ionized hypersonic flows. Physics of Fluids, 2008. **20**(4): p. 046102.

9. Starkey, R.P., Electromagnetic Wave/Magnetoactive Plasma Sheath Interaction for Hypersonic Vehicle Telemetry Blackout Analysis, in AIAA. 2003. p. AIAA2003-4167.

10. Gillman, E.D., J.E. Foster, and I.M. Blankson, Review of Leading Approaches for Mitigating Hypersonic Vehicle Communications Blackout and a Method of Ceramic Particulate Injection Via Cathode Spot Arcs for Blackout Mitigation, in Report. 2010, NASA Glenn Research Center: Cleveland, Ohio.

11. Johnson, J.E., R.P. Starkey, and M.J. Lewis, *Aerodynamic Stability of Reentry Heat Shield Shapes for a Crew Exploration Vehicle*. Journal of Spacecraft and Rockets, 2006. **43**(4): p. 721-730.

12. Zhong, J.Q., T. Ozawa, and D.A. Levin, *Modeling of Stardust Reentry Ablation Flows in the Near-Continuum Flight Regime* AIAA Journal, 2008. **46**(10): p. 2568-2581.

13. Zhaunerchyk, V., et al., *Dissociative recombination study of Na+(D2O) in a storage ring.* The Journal of Chemical Physics, 2004. **121**(21): p. 10483-10488.

14. Shneider, M.N. and R.B. Miles, *Microwave diagnostics of small plasma objects.* Journal of Applied Physics, 2005. **98**(3).

15. Shneider, M.N., Z. Zhang, and R.B. Miles, Simultaneous resonant enhanced multiphoton ionization and electron avalanche ionization in gas mixtures. Journal of Applied Physics, 2008. **104**(2): p. 9.

16. Miles, R.B., et al., Microwave scattering from laser ionized molecules: A new approach to nonintrusive diagnostics. AIAA Journal, 2007. **45**(3): p. 513-515.

17. Zhang, Z. and M.N. Shneider, Measurement of plasma decay processes in mixture of sodium and argon by coherent microwave scattering. Physics of Plasmas, 2010. **17**(1).

18. Wu, Y., et al., Measurement of sodium-argon cluster ion recombination by coherent microwave scattering. Applied Physics Letters, 2012. **100**(11): p. -.

19. Leake, J.W., *Tables of Physical & Chemical Constants*, K.L. Online, Editor. 1995, Kaye & Laby Online.

20. Raizer, Y.P., *Gas discharge physics*. 1997: Springer, New York.

Appendix

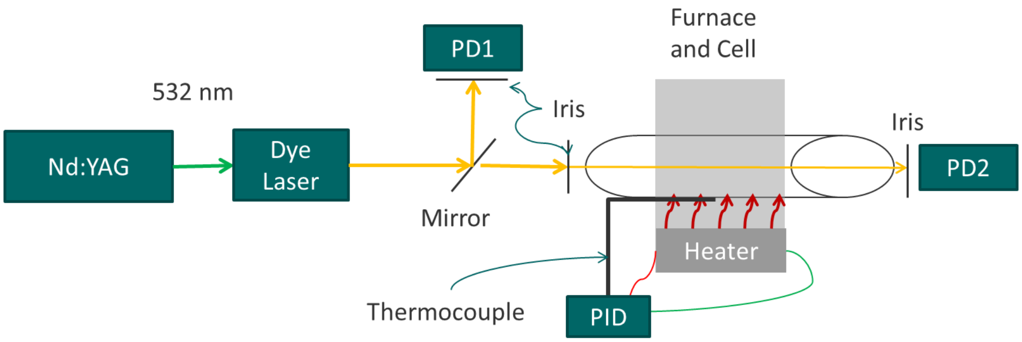

Figure 24. Schematics of experimental setup. The sodium cell is heated by two separate heaters. The concrete block heater controls the overall number density of the cell and the temperature of the main body. Three irises limit the amount of light into the photodiodes, PD_1 and PD_2 to avoid the saturation.

Table 1. Properties of sodium D_1 and D_2 lines from NIST.

Line	D_1	Units	D_2	Units
Wavelength(nm)	589.5924	nm	588.995	Nm
Temperature(K)	673	K	673K	K
Number Density of Argon	100	Torr	100	Torr
Number Density of Sodium	10	$10^{10}/cm^3$	10	$10^{10}/cm^3$
Einstein Coeff. A_{21}	6.14×10^7	s^{-1}	6.16×10^7	s^{-1}
Degeneracy g_2/g_1	2/2	1	4/2	1
Argon broadening linewidth	1.209413E+09	s^{-1}	1.016000E+09	s^{-1}
Argon shift linewidth	-1.218444E-02	cm^{-1}	-1.300858E-02	cm^{-1}
Self broadening linewidth	3.070000E+04	s^{-1}	4.670000E+04	s^{-1}
Doppler broadening linewidth	2.284049E-12	m	2.281735E-12	M
Natural linewidth	6.140000E+07	s^{-1}	6.160000E+07	s^{-1}
Lorentzian linewidth	1.244528E+10	rad/s	1.614172E+10	rad/s
Gaussian linewidth	6.681119E+10	rad/s	6.679860E+10	rad/s
Cross section	3.397178E-22	m^2	4.063331E-21	m^2

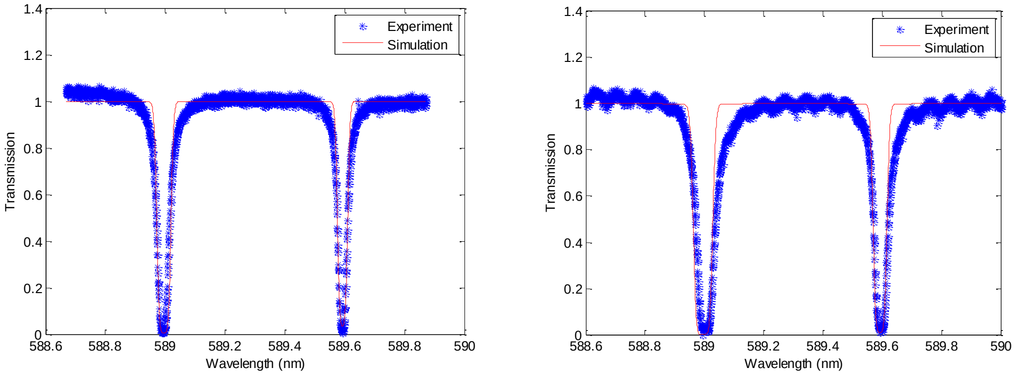

(a) (b)

Figure 25. Comparisons of experimental and theoretical absorption profiles of D_1 and D_2 lines of sodium vapor with a buffer gas of (a) Ar and (b) N_2 at 100 Torr and 300 °C. The fitted sodium densities were determined to be (a) 5.79E11 cm^{-3} and (b) 3.22E11 cm^{-3}.

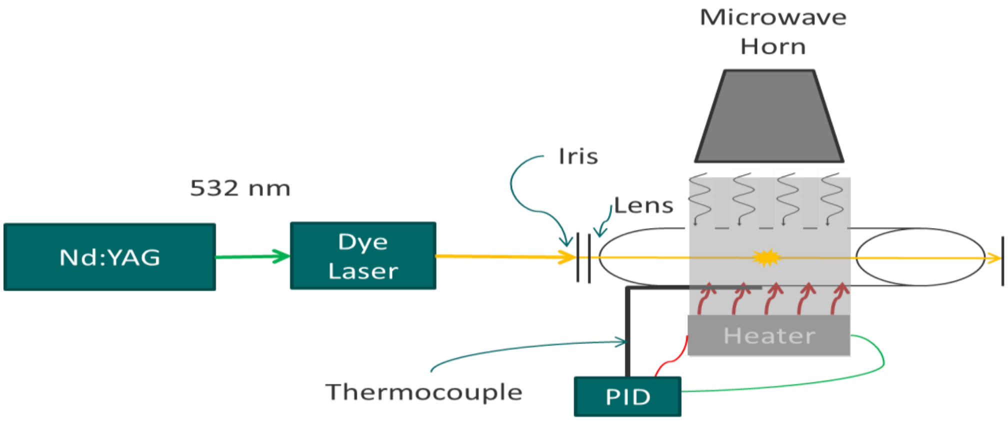

Figure 26. Experimental Radar REMPI setup. The output beam of the dye laser was focused by a 10 cm focal length lens to generate the 2+1 Sodium REMPI plasma. The microwave system was used for detection of the plasma.

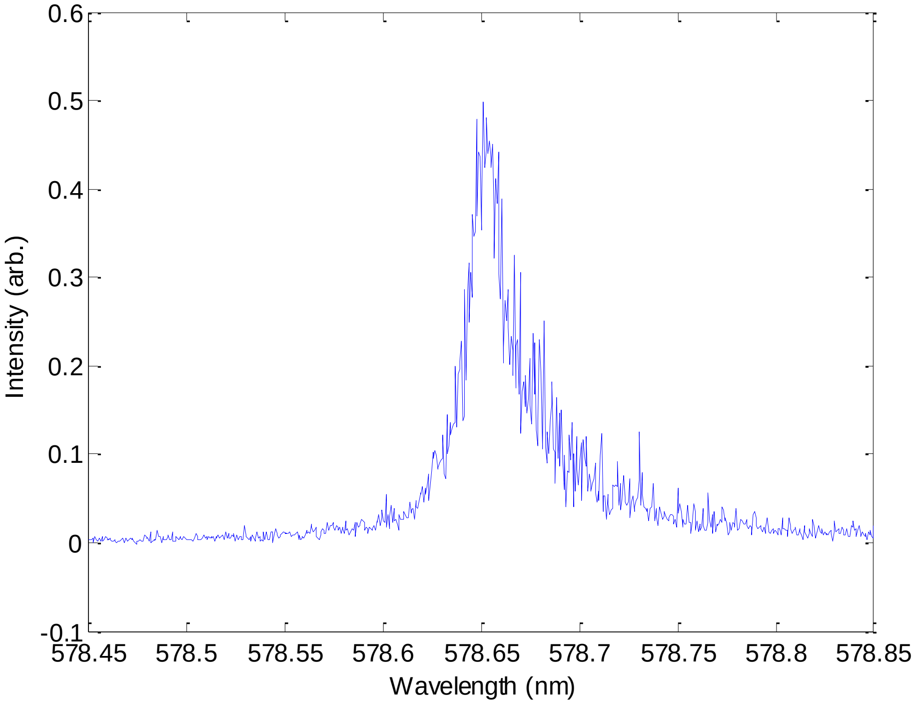

Figure 27. 2+1 REMPI spectrum of sodium in nitrogen buffer gas at 100 Torr.

Table 2. Reactions present in plasma dynamic model.

Reaction	Rate Constant
Radiative Recombination 1) $Na^+ + e^- \rightarrow Na$	$k_1 = 2.7E\text{-}13 * T_e^{-3/4}$ (cm^3/s).[20]
Electron Stabilized Recombination 2) $Na^+ + e^- + e^- \rightarrow Na + e^-$	$\beta_{3e} = 8.75E\text{-}27 * T_e^{-9/2}$ (cm^6/s)[20]
Neutral Stabilized Recombination 3a) $Na^+ + Ar + e^- \rightarrow Na + Ar$ 3b) $Na^+ + N_2 + e^- \rightarrow Na + N_2$	β_{3N} (cm^6/s)=?
Cluster Ion Conversion 4a) $Na^+ + Ar + Ar \rightarrow Na^+ \cdot Ar + Ar$ 4b) $Na^+ + N_2 + N_2 \rightarrow Na^+ \cdot N_2 + N_2$	$k_{conv} = 0.9E\text{-}31 * \left(\frac{317}{T_{gas}}\right)$^3 (cm^6/s) $k_{conv} = (2.6 \pm 1.2)E\text{-}30$ (cm^6/s)
Dissociative recombination 5a) $Na^+ \cdot Ar + e^- \rightarrow Na + Ar$ 5b) $Na^+ \cdot N_2 + e^- \rightarrow Na + N_2$	β_{dr} (cm^6/s)=?
H_2O Clustering 6) $Na^+ + H_2O + N_2 \leftrightarrow Na^+ \cdot H_2O + N_2$	$k_{6,eq} = 1.74E\text{-}4$, [13] $k_{6,f} = 9.5E\text{-}30 * \left(\frac{300}{T_e}\right)^{1.5}$, $k_{6,b} = \frac{k_{6,f}}{k_{6,eq}}$
H_2O Cluster Ion Switching and Dissociation 7) $Na^+ \cdot N_2 + H_2O \rightarrow Na^+ \cdot H_2O + N_2$, 8) $Na^+ \cdot H_2O + e^- \rightarrow Na + H_2O$,	$k_7 = 1E\text{-}29$ (cm^6/s) $k_8 = 2.3E\text{-}7 * \left(\frac{Te}{300}\right)^{-0.95}$ (cm^6/s)
9) Ambipolar Diffusion $D_a \cong \frac{\mu k T_e}{e}, \frac{dn_e}{dt} \approx \frac{dn_{Na+}}{dt} + \frac{dn_{NaN_2^+}}{dt} \approx -D_a n_e$	

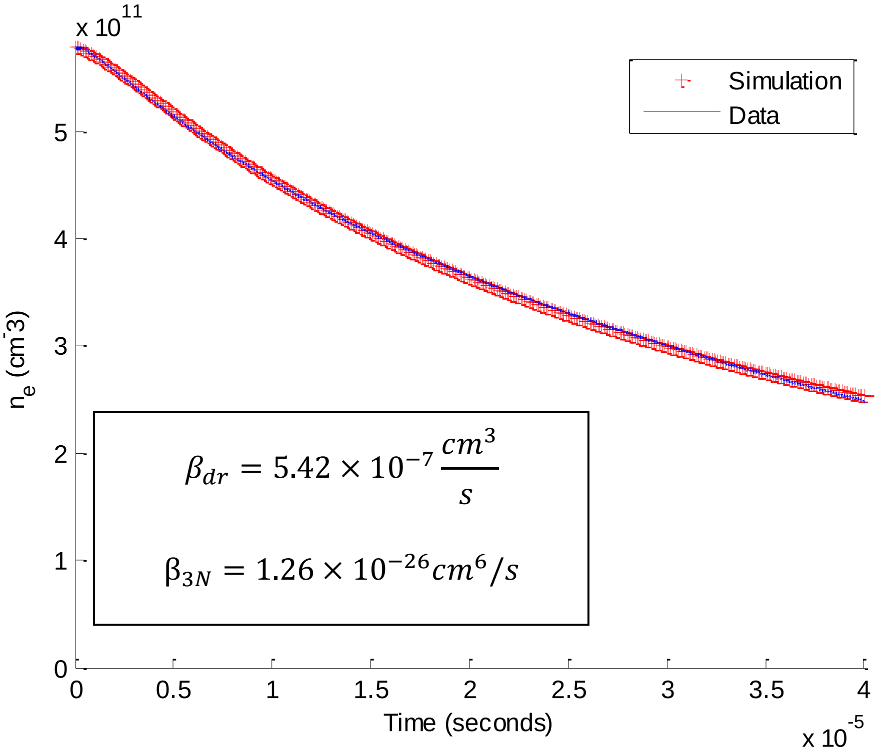

Figure 28. Comparison of experimental and fitted electron number density curves for the first 40 microseconds

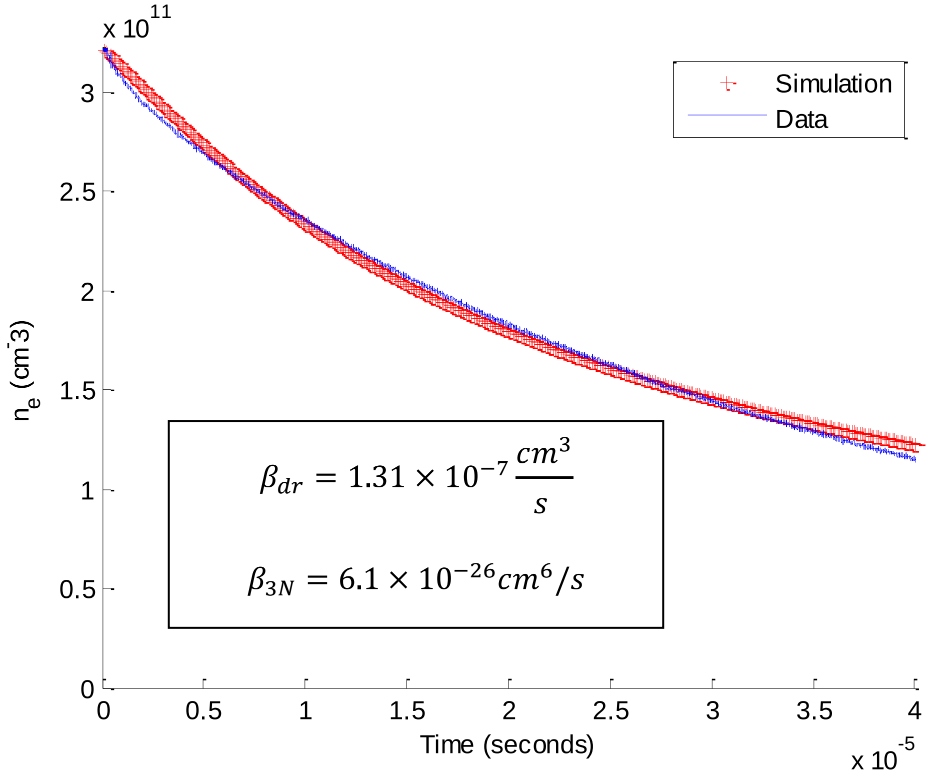

Figure 29. Comparison of experimental and fitted electron number density curves for the first 40 microseconds

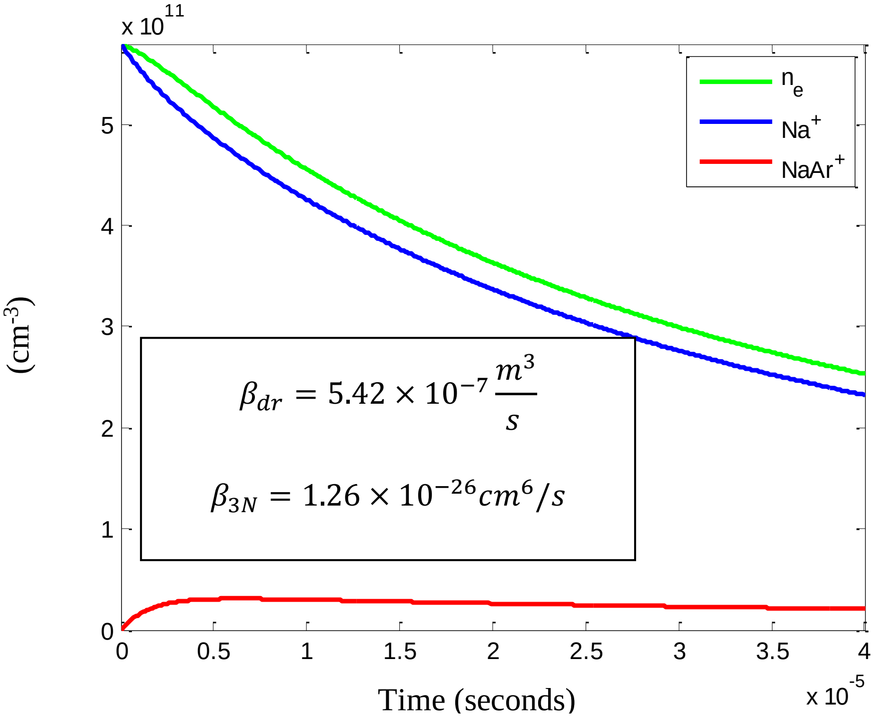

Figure 30. Simulated electron, sodium ion, and sodium-argon cluster ion number density curves

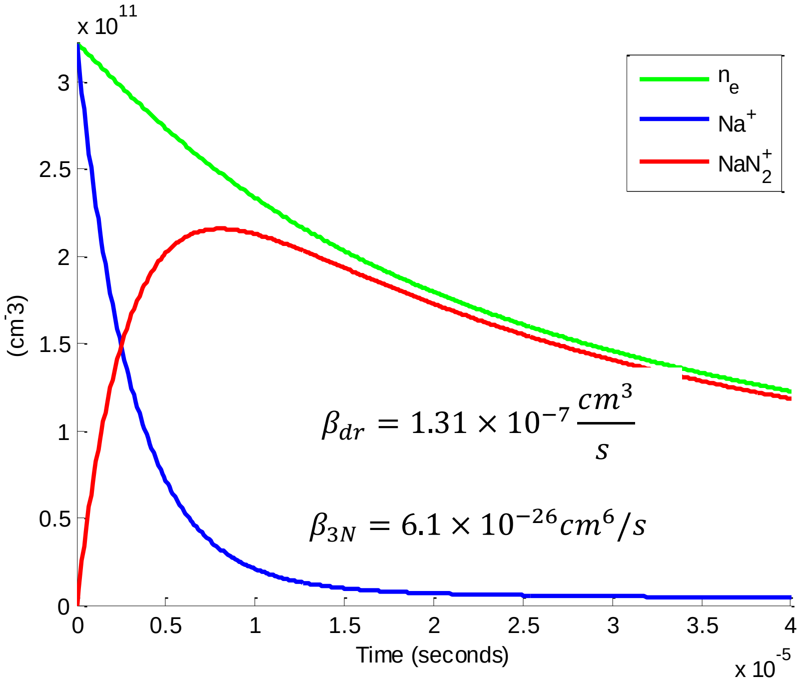

Figure 31. Simulated electron, sodium ion, and sodium-nitrogen cluster ion number density curves

CHAPTER V

O_2 ROTATIONAL TEMPERATURE MEASUREMENTS IN AN ATMOSPHERIC AIR MICRODISCHARGE BY RADAR REMPI

This article, “O2 rotational temperature measurements in an atmospheric air microdischarge by Radar REMPI”, was received on the 8th of March 2013, accepted on the 4th of June 2013, and published on the 19th of June 2013.

Author Affiliations:

Jordan Sawyer[1], Yue Wu[1] and Zhili Zhang[1], and Steven F. Adams[2]

[1]Department of Mechanical, Aerospace and Biomedical Engineering, University of Tennessee, Knoxville TN 37996, USA

[2]Air Force Research Laboratory (AFRL/RQQE), Wright-Patterson AFB, OH 45433-7919, USA

Sawyer, J., et al., O2 rotational temperature measurements in an atmospheric air microdischarge by radar resonance-enhanced multiphoton ionization. Journal of Applied Physics, 2013. 113(23): p. 233304.

Abstract

Nonintrusive spatially-resolved rotational temperature measurements in an atmospheric air microdischarge are presented. The measurements were based on coherent microwave Rayleigh scattering (Radar) from Resonance-Enhanced Multiphoton Ionization (REMPI) of molecular oxygen. The open air DC microdischarge source operated in a stable “normal-glow” mode and pin-to-pin electrodes spaced 1.3 mm apart. The second harmonic of a tunable dye laser beam was focused between the two electrodes and scanned between 286 and 288 nm. Coherent microwave Rayleigh scattering was used to collect the two-photon rotational spectra of O_2 at $C^3\Pi(v=2)\leftarrow X^3\Sigma(v'=0)$ transitions. The Boltzmann plots from analyses of the O_2 rotational lines determined local rotational temperatures at various axial locations between the electrodes. The molecular oxygen rotational temperature varied from ~1150 K to ~1350K within the discharge area. The measurements had an accuracy of ~±50 K.

Introduction

The advent of stable microdischarges dates back to the work of White in the 1950s [1] and gained much attention in spatially confined cavities in the 1990's.[2, 3] Numerous applications, including plasma ignition[4], VUV light sources[5], nanoparticle synthesis[6, 7], and biomedical research [8, 9] have been investigated. Microdischarge devices take advantage of the scaling of breakdown voltage with the product of pressure and gap distance (*pd*) as described by Paschen's Law.[10] Typically, to maintain the stability of "normal-glow" discharges at atmospheric pressure, the inter-electrode separation is confined to distances on the order of 1 mm or less.[11] This small spacing leads to the generation of a non-thermal or "cold" plasma. A striking property of these non-equilibrium plasmas is that the electron temperature, T_e, is often several orders of magnitude larger than the gas temperature, T_g.[11, 12] This excess electron energy can be channeled to drive specific optical or chemical processes at relatively low gas temperature, which opens microdischarges to the wide range of applications previously mentioned.

Although tremendous progress has been made in the area of plasma diagnostics in microdischarges[12], many fundamental properties, such as temperature, are still not satisfactorily measured. A non-thermal plasma is described, not by a single temperature, but by a set of temperatures including electron temperature (T_e) relating to the kinetic energy distribution of the electrons, as well as several molecular temperatures, T_trans, T_vib, and T_rot relating to the translational, vibrational, and rotational energies of the molecules. Typically the temperature set in a non-thermal plasma will have the characteristic of $T_\mathrm{e} >> T_\mathrm{vib} > T_\mathrm{trans} = T_\mathrm{rot,}$ where T_trans and T_rot are commonly identified as the gas temperature, T_g_ENREF_5. The gas temperature in these non-thermal plasmas can range from near room temperature for monatomic gases such as argon to above 2000K in molecular gases such as air,[11, 13] and is highly dependent on discharge source parameters such as electrical current. The most widely published diagnostic works involve determining rotational temperature by optical emission spectroscopy (OES) of the N_2 second positive system.[14-16] Unfortunately, the spatial and temporal resolutions achievable by these methods have stringent limitations. Additionally, OES is limited for certain species in the microplasma.[17] Another temperature measurement using Stark shifting analysis of the H_β transition involves hydrogen seeding, which complicates the overall plasma composition.[18] Cavity Ringdown spectroscopy is a line-of-sight temperature measurement which has limited spatial resolution.[17] Overall, the diagnostic tools available for microdischarge analysis in atmospheric air are scarce and restrict, in some way, what can be accurately derived from the experimental process.

Here, coherent microwave scattering (Radar) from Resonance-Enhanced Multiphoton Ionization (REMPI) boasts excellent spatial and temporal resolutions. Radar REMPI has previously been demonstrated for local rotational temperature measurements of molecular oxygen in static cell[19] and flame[20] environments. In this work Radar REMPI measurements of the local O_2 rotational temperature within an atmospheric air microdischarge are presented. These measurements are performed at eight axial locations between pin-to-pin electrodes; this allowed for an axial temperature distribution within the discharge region to be determined.

Molecular Oxygen Structure and REMPI Scheme

The 2+1 REMPI scheme used here in O_2 with an intermediate $\mathrm{C}^3\Pi(\upsilon = 2) \leftarrow \mathrm{X}^3\Sigma$ transition was described in detail in our previous publications [19, 20]. The molecular oxygen ground state, $\mathrm{O}_2(\mathrm{X}^3\Sigma)$, can be best described as Hund's case (b), and the $\mathrm{O}_2(\mathrm{X}^3\Sigma)$ ground-state term energy can be expressed as

$G_1 = B_\upsilon J(J+1) \text{-} D_\upsilon J^2(J+1)^2 + (2J+3)B_\upsilon \text{-} L \text{-} \sqrt{(2J+3)^2 B_\upsilon^2 + L^2 \text{-} 2LB_\upsilon} + G(J+1)$,

$G_2 = B_\upsilon J(J+1) \text{-} D_\upsilon J^2(J+1)^2$,

$$G_3 = B_\upsilon J(J+1) \text{-} D_\upsilon J^2(J+1)^2 + (2J+1)B_\upsilon \text{-} L \text{-} \sqrt{(2J \text{-} 1)^2 B_\upsilon^2 + L^2 \text{-} 2LB_\upsilon} + GJ$$

where the molecular constants above for the ground-state $X^3\Sigma$ are all well known.[21] The molecular oxygen excited state $O_2(C^3\Pi(\upsilon = 2))$, used as an intermediate state in the experiments, can be best described as Hund's case (a). The energy levels for the excited-state $O_2(C^3\Pi(\upsilon = 2))$ are thus expressed by

$F_1(\Omega = 0) = n_{01} + B_{eff1}J(J+1) \text{-} D_{\upsilon 1}J^2(J+1)^2$,

$F_2(\Omega = 1) = n_{02} + B_{eff2}J(J+1) \text{-} D_{\upsilon 2}J^2(J+1)^2$,

$F_3(\Omega = 2) = n_{03} + B_{eff3}J(J+1) \text{-} D_{\upsilon 3}J^2(J+1)^2$,

where the derived constants of the excited-state $C^3\Pi(\upsilon = 2)$ of molecular oxygen are listed in **Error! Reference source not found.** based on our previous experimental and computational study of the REMPI spectra of molecular oxygen. Both the ground and excited states contribute to the hyperfine structures in the REMPI spectra. The two-photon transition line strength, $T_{f,g}^2$, between the excited-state $C^3\Pi$ and the ground-state $X^3\Sigma$ has been modeled and expressed as

$$T_{f,g}^2 = \sum_{k=0,2} \frac{\left|\beta_k^{(2)}\right|^2}{2k+1} (2J+1)(2J'+1)(2N'+1) \times \begin{bmatrix} J' & S & N' \\ \Lambda' + \Sigma & \text{-}\Sigma & \text{-}\Lambda' \end{bmatrix}^2 \begin{bmatrix} J & k & J' \\ \Omega & \text{-}\Delta\Lambda & \text{-}\Lambda' \text{-}\Sigma \end{bmatrix}^2, \quad (1)$$

where [...] is the Wigner 3-*j* symbol, J is the rotational quantum number, N is total angular momentum except the spin, $\beta_k^{(2)}$ is polarization coefficient, primed parameters are for the ground state of $X^3\Sigma$ and unprimed parameters are for the excited state of $C^3\Pi$. For linearly polarized light, terms of both k=0 and 2 contribute to the final line strength, $\beta_k^{(2)} = \sqrt{10/3}$, while for circularly polarized light, only k = 2 contributes and $\beta_k^{(2)} = \sqrt{5}$.

In the previous O_2 rotational temperature study[22], the S_{21} branch was chosen for the temperature analyses due to the distinctness in spectral position and intensity among the experimentally observable lines at relatively low temperature (<700 K). At elevated temperature, the S branch lines become congested due to the overlap of multiple branches, including the other four common branches O, P, Q, and R.[20] Figure 32 shows a comparison of experimental spectra of molecular oxygen at low temperature in air (~300K) and at a moderately high temperature in an air microdischarge (~1200 K), respectively. The population distribution in the discharge was shifted toward higher rotational states due to the increased temperature, which visibly enhanced several spectral peaks between 286.0 and 288.0 nm and enabled more branches besides S_{21} to be involved in the higher temperature analyses in this paper.

The microwave scattering signal from the REMPI produced plasma is proportional to the total number of electrons inside the plasma, which is proportional to the total number of electron excitations to the continuum through the resonant two photon transition followed by the single photon ionization[23]. The total number of electron excitations to the continuum is thus determined by the product of the number of molecules in the ground state and the rate of multiphoton ionization. An expression for the resulting microwave scattering signal for a given two photon transition from state *g* to *f* can be written as

$$\mathrm{E_{MW}} \propto \mathrm{N_e} = \mathrm{N_0} \cdot \mathrm{T_{f,g}^2 I^2} \cdot \mathrm{T_{fi} I} \cdot \exp\left(\text{-}\mathrm{E_g}/\mathrm{k_B T}\right) \qquad (2)$$

where E_{MW} is the scattering microwave electric field, N_e is total electron number inside the plasma generated by REMPI, N_0 is the total number of oxygen molecules in the laser focal region, E_g is the energy of the ground state of $X^3\Sigma$, k_B is Boltzmann constant, T is temperature, I is the intensity of the laser beam, and T_{fi} is the ionization cross section from the excited state to the ionization continuum.

A rotational temperature can be extracted from the analysis of the ground state rotational energy distribution derived from the REMPI spectrum. The thermal distribution of the rotational levels is given by a statistically weighted (i.e. quantum degenerated) Boltzmann factor of $J(J+1)\exp\left(-E_g/k_BT\right)$. The rotational level with the maximum population shifts toward higher J values with increasing temperature. This shift is reflected in the REMPI spectrum of the molecule. The variation of the intensity of the rotational lines in an electronic manifold is given by the thermal population distribution of the rotational levels. If T_{fi} is assumed to be constant over the limited laser wavelength scanning range and the ground state population N_0 is constant during the scan time, the Boltzmann plots can be formulated as

$$\log(E_{MW}/I^3T_{f,g}^2)/E_g \propto -(k_BT)^{-1}. \qquad (3)$$

When a region of the spectrum including numerous rotational lines is measured, a statistical fit of the Boltzmann plot gives an accurate measurement of the rotational populations and thus the rotational temperature, i.e., the slope of the Boltzmann plot as shown in the *Equation (3)*.

Experimental Setup

The experimental setup of O_2 rotational temperature measurement in a DC air microdischarge is shown in Figure 33. An Nd: YAG laser was used to pump a dye laser with Rhodamine 6G as the dye. The output of the dye laser was frequency doubled by an automatic second harmonic generation and tracking system allowing tunable ultraviolet radiation between 286 and 288 nm. The ultraviolet laser beam (6~8 mJ/pulse), from the tracking system, was first reflected by a pair of mirrors (M1 and M2) on a vertical transition stage, then focused by a lens (f=25mm) to generate the REMPI plasma within the atmospheric air microdischarge. As a rough estimate of the beam diameters, the waist size of the focused light beam is 1.5 μm with a depth of focus of 13 μm at the focal spot for an ideal Gaussian beam. A transition stage was employed in the experiment to vertically move the laser focal point precisely along the interelectrode axis using a stepper motor (SM1). The first eight sequential pictures in Figure 34 approximately show the position of laser focal points by generating laser-induced breakdown between the two electrodes.

A microwave homodyne system (MDS) was used to detect the REMPI plasma[24]. A 10dBm tunable microwave source was first split into two channels. One channel was used to illuminate the ionization point through a microwave horn. Microwave scattering from the plasma was collected by the same microwave horn. The received microwave passed through a microwave circulator and was amplified 30 dB by one preamplifier at ~10 GHz. After frequency was converted down in the mixer, two other amplifiers with bandwidth of 2.5 kHz to 1.0 GHz amplified the signal by another factor of 60 dB. From the geometry of dipole radiation, the polarization of the microwave was chosen to be along the propagation direction of the laser to maximize the scattering signal. The time-accurate microwave scattering signal was monitored by an oscilloscope. The microwave signal was also input into an automatic data acquisition system, which recorded the rotational spectrum of oxygen as the laser wavelength was scanned.

A 5 kV maximum dc power supply was used in series with a 1 MΩ load resistor to energize the microdischarge. The air microdischarge was generated by a pin-to-pin electrode configuration with an inter-electrode gap of 1.30 mm. In the experiments, a 4.8 kV voltage was applied by the dc power supplier which provided the microdischarge with a reasonable electrical and spatial stability. The majority of the high voltage dropped across the load resistor with the remaining 78±2

V dropping across the electrode gap while microdischarge current fluctuated between 4.60 mA and 4.73 mA. The microdischarge observed during the experiments is shown in the last two photographs in Figure 34. The plasma operated in a “normal glow” mode for REMPI temperature measurements. The discharge was reasonably stable and was not disturbed by the focused laser beam. However, when the laser beam focal spot was positioned too close to the anode or cathode, the microwave detection system obtained strong oscillating signals. This was possibly caused by the high energy electrons and molecular ions from the REMPI process near anode and cathode, respectively. Hence, the temperature distribution was measured at eight different axial positions between the electrodes, equally spaced at 0.10 mm intervals, but with an offset distance of 0.28 mm from the anode and cathode. Images of air breakdown emission induced by the intense laser beam spot are shown in the first six photographs of Figure 34, indicating the laser focal positions between the two electrodes with no discharge. Compared to the finite radial width of the microdischarge (<0.4 mm), the depth of focus of the laser beam (13 μm) was much smaller. So while the microdischarge was operating, the laser focal spot was centered radially in the plasma and confined to a region without a significant radial variation in temperature. With the microdischarge on, the focal region was pre-ionized by the plasma and the laser did not induce a more expansive breakdown, in the air, leaving the microwave scattering signal confined to the depth of focus region within the plasma. The environment inside the plasma was quite harsh and different from our previous experimental situations (i.e. pure oxygen in cell and room air), however, detection of the microwave radiation scattered by REMPI electrons was notimpeded by background radiation from the air microdischarge. In fact, the spectra of O_2 were reasonably undisturbed by the microdischarge and fairly good and repeatable experimental data were obtained in this electrically and optically active environment (Figure 32). It is assumed that any heating of the air by the laser beam is negligible since the duty cycle of the laser pulse is small and relatively low average power compared to the microdischarge power.

Results and Discussion

Eight separate spectra of molecular oxygen were analyzed corresponding to the eight different axial positions probed in the microdischarge. The spectrum shown in Figure 35 is for the uppermost scanning position along the microdischarge axis which was 0.28 mm away from the anode. The red circle points in Figure 35 were the peak values extracted from the analysis of the molecular oxygen ground state rotational energy distribution derived from the REMPI spectrum. The transition assignments of these peak points are shown in Table 4.

After all the peak points were assigned in the eight spectra with the branch information shown in Table 4, Boltzmann plots of the selected rotational lines were generated as shown in the following Figure 36. In each Boltzmann plot, a linear curve fit was applied to the peak values of the selected rotational lines. The R-squared value and slope of the fitted line are shown in the left bottom corner of each figure. The temperature at each scanning point was determined by the slope of the linear curve fit.

The O_2 rotational temperature distribution within the microdischarge was derived from the Boltzmann plots in Figure 36 which provided a determination of the O_2 ground-state population distributions at the local positions in the atmospheric microdischarge. The axial temperature distribution of the microdischarge was obtained and is shown in Figure 37. Due to the characteristics of the Boltzmann plot and linear fit, the variation in rotational temperature was highly sensitive to small changes in the slope of the fitted line. Hence this approach could precisely track temperature variation, however, the temperature uncertainties were relatively large (~ ± 50 K in Figure 37) as a trade-off in accuracy. The scanning resolution was 0.10 mm, as mentioned above. This resolution was small enough to reveal the basic envelope of the temperature distribution for a normal glow discharge within 1.30 mm between two electrodes with a pin-to-pin configuration.

Conclusions

This work presents a new diagnostic tool for determining local rotational temperatures in atmospheric air microdischarges. Radar REMPI measurements were made at eight different axial locations in a stable “normal-glow” microdischarge between two pin electrodes. Local rotational temperatures were obtained from the 2+1 REMPI spectra of molecular oxygen $C^3\Pi(v=2) \leftarrow X^3\Sigma(v'=0)$ transition as determined by Radar REMPI. The axial temperature distribution within the microdischarge with a 1.3 mm electrode spacing was determined.

Acknowledgements

This work is being supported by NSF CBET-1032523 and Air Force Office of Scientific Research.

References

1. White, A.D., *New Hollow Cathode Glow Discharge.* Journal of Applied Physics, 1959. **30**(5): p. 711-719.

2. Schoenbach, K.H., et al., *Microhollow cathode discharges.* Applied Physics Letters, 1996. **68**(1): p. 13-15.

3. Iza, F., et al., *Microplasmas: Sources, Particle Kinetics, and Biomedical Applications.* Plasma Processes and Polymers, 2008. **5**(4): p. 322-344.

4. Pancheshnyi, S.V., et al., *Ignition of Propane–Air Mixtures by a Repetitively Pulsed Nanosecond Discharge.* Plasma Science, IEEE Transactions on, 2006. **34**(6): p. 2478-2487.

5. Ren'an, B., et al., *Development of 146nm Vacuum UV Light Source.* Physics Procedia, 2012. **32**(0): p. 477-481.

6. Chiang, W.-H. and R.M. Sankaran, Microplasma synthesis of metal nanoparticles for gas-phase studies of catalyzed carbon nanotube growth. Applied Physics Letters, 2007. **91**(12): p. 121503-3.

7. Richmonds, C. and R.M. Sankaran, Plasma-liquid electrochemistry: Rapid synthesis of colloidal metal nanoparticles by microplasma reduction of aqueous cations. Applied Physics Letters, 2008. **93**(13): p. 131501-3.

8. Goree, J., et al., *Killing of S. mutans Bacteria Using a Plasma Needle at Atmospheric Pressure.* Plasma Science, IEEE Transactions on, 2006. **34**(4): p. 1317-1324.

9. Kim, J.Y., et al., 15-μm-sized single-cellular-level and cell-manipulatable microplasma jet in cancer therapies. Biosensors and Bioelectronics, 2010. **26**(2): p. 555-559.

10. Paschen, F., Ueber die zum Funkenübergang in Luft, Wasserstoff und Kohlensäure bei verschiedenen Drucken erforderliche Potentialdifferenz. Annalen der Physik, 1889. **273**(5): p. 69-96.

11. Foest, R., M. Schmidt, and K. Becker, *Microplasmas, an emerging field of low-temperature plasma science and technology.* International Journal of Mass Spectrometry, 2006. **248**(3): p. 87-102.

12. Laux, C.O., et al., *Optical diagnostics of atmospheric pressure air plasmas.* Plasma Sources Science and Technology, 2003. **12**(2): p. 125.

13. Becker, K.H., K.H. Schoenbach, and J.G. Eden, *Microplasmas and applications.* Journal of Physics D: Applied Physics, 2006. **39**(3): p. R55.

14. Goyette, A.N., et al., Experimental comparison of rotational and gas kinetic temperatures in N2 and He-N2 discharges Journal of Physics D: Applied Physics, 1998. **31**(13): p. 1556.

15. Nassar, H., et al., N 2 + /N 2 ratio and temperature measurements based on the first negative N 2 + and second positive N 2 overlapped molecular emission spectra. Journal of Physics D: Applied Physics, 2004. **37**(14): p. 1904.

16. Staack, D., et al., Spatially Resolved Temperature Measurements of Atmospheric-Pressure Normal Glow Microplasmas in Air. Plasma Science, IEEE Transactions on, 2007. **35**(5): p. 1448-1455.

17. Stancu, G.D., et al., *Atmospheric pressure plasma diagnostics by OES, CRDS and TALIF.* Journal of Physics D: Applied Physics, 2010. **43**(12): p. 124002.

18. Xi-Ming, Z., C. Wen-Cong, and P. Yi-Kang, *Gas temperature, electron density and electron temperature measurement in a microwave excited microplasma.* Journal of Physics D: Applied Physics, 2008. **41**(10): p. 105212.

19. Wu, Y., Z. Zhang, and S.F. Adams, *O2 rotational temperature measurements by coherent microwave scattering from REMPI.* Chemical Physics Letters, 2011. **513**(4–6): p. 191-194.

20. Wu, Y., et al., Flame temperature measurements by radar resonance-enhanced multiphoton ionization of molecular oxygen. Appl. Opt., 2012. **51**(28): p. 6864-6869.

21. Mainos, C., Multiphoton Rotational Line Strength in Diatomic-Molecules and for States with Hunds-Case-(a) or Hunds-Case-(B) Coupling. Physical Review A, 1986. **33**(6): p. 3983-3992.

22. Wu, Y., Z.L. Zhang, and S.F. Adams, *O-2 rotational temperature measurements by coherent microwave scattering from REMPI.* Chemical Physics Letters, 2011. **513**(4-6): p. 191-194.

23. Zhang, Z., Coherent microwave scattering of laser-induced plasma, in Mechanical and Aerospace Engineering 2008, Princetion University. p. 36-46.

24. Zhang, Z.L. and M.N. Shneider, Measurement of plasma decay processes in mixture of sodium and argon by coherent microwave scattering. Physics of Plasmas, 2010. **17**(3).

Appendix

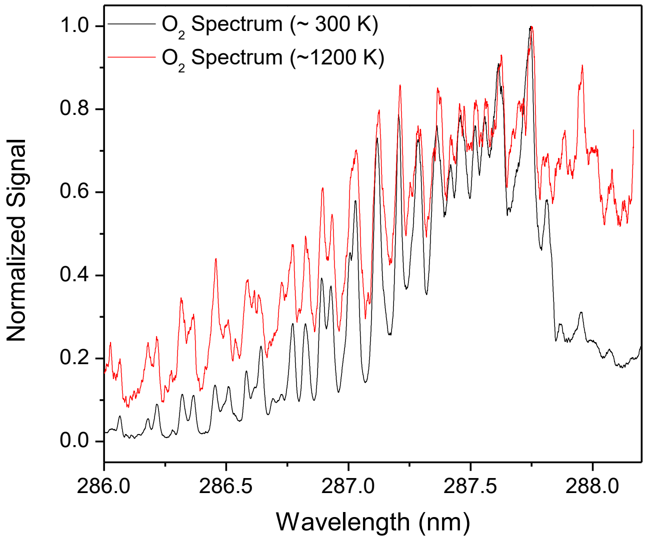

Figure 32. Spectra of molecular oxygen in atmospheric air (300K) and air microdischarge (1200K).

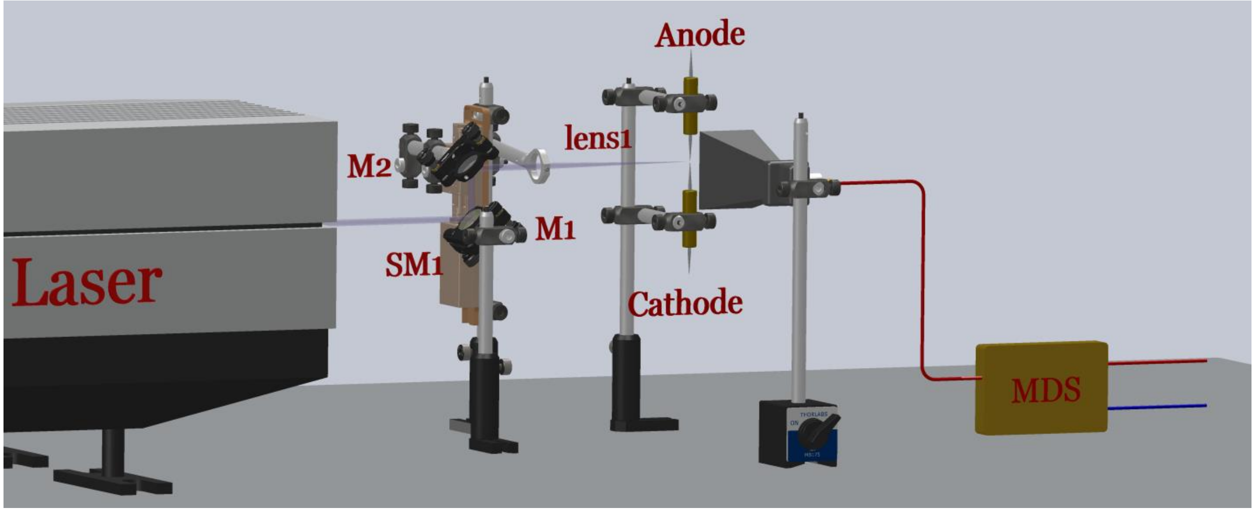

Figure 33. Experimental setup, the microdischarge was generated by two pin electrodes, microwave detection system (MDS) was used to collect the REMPI signal in the microdischarge.

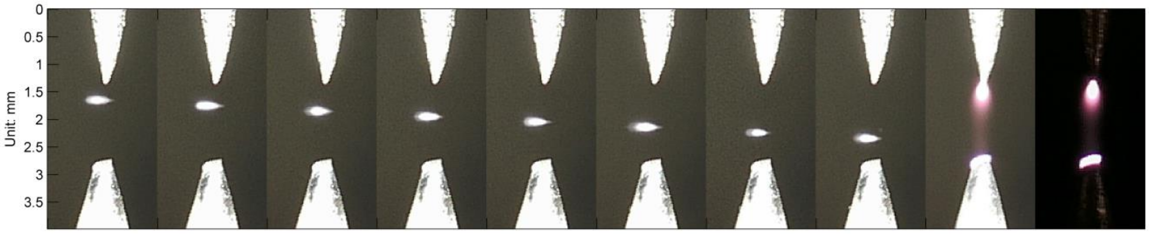

Figure 34. The first eight sequential photographs show the different scanning positions between the two electrodes without the microdischarge; the ninth and tenth photographs show the microdischarge (glow discharge) with and without camera light respectively.

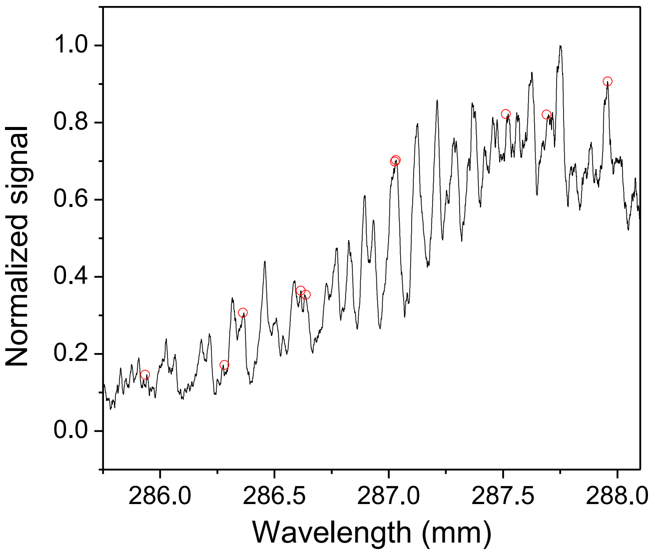

Figure 35. Spectrum of molecular oxygen in an atmospheric microdischarge.

Table 3. Adopted Constants for $C^3\Pi(\upsilon = 2)$ of Molecular Oxygen.

cm^{-1}	$F_1(\Omega = 0)$	$F_2(\Omega = 1)$	$F_3(\Omega = 2)$
n_0	69369(2)	69449(1)	69552(1)
B_{eff}	1.61(5)	1.65(1)	1.69(1)
D_υ	$1.9(5)\times10^{-5}$	$1.6(2)\times10^{-5}$	$1.9(2)\times10^{-5}$

Table 4. Selected rotational lines for temperature measurements in the microdischarge.

Branch	J'	Wavelength (nm)	G_1 (cm^{-1})	$T_{f,g}^2$
R_{11}	42	285.935	2459.69	11.129
P_{32}	43	286.282	2703.41	22.927
R_{11}	36	286.362	1802.31	9.630
R_{12}	39	286.615	2231.73	20.500
R_{11}	32	286.637	1420.02	8.631
R_{11}	26	287.027	931.19	7.132
S_{31}	8	287.031	79.55	3.269
P_{32}	5	287.512	44.20	3.200
R_{11}	14	287.690	260.46	4.138
S_{21}	7	287.958	81.57	3.706

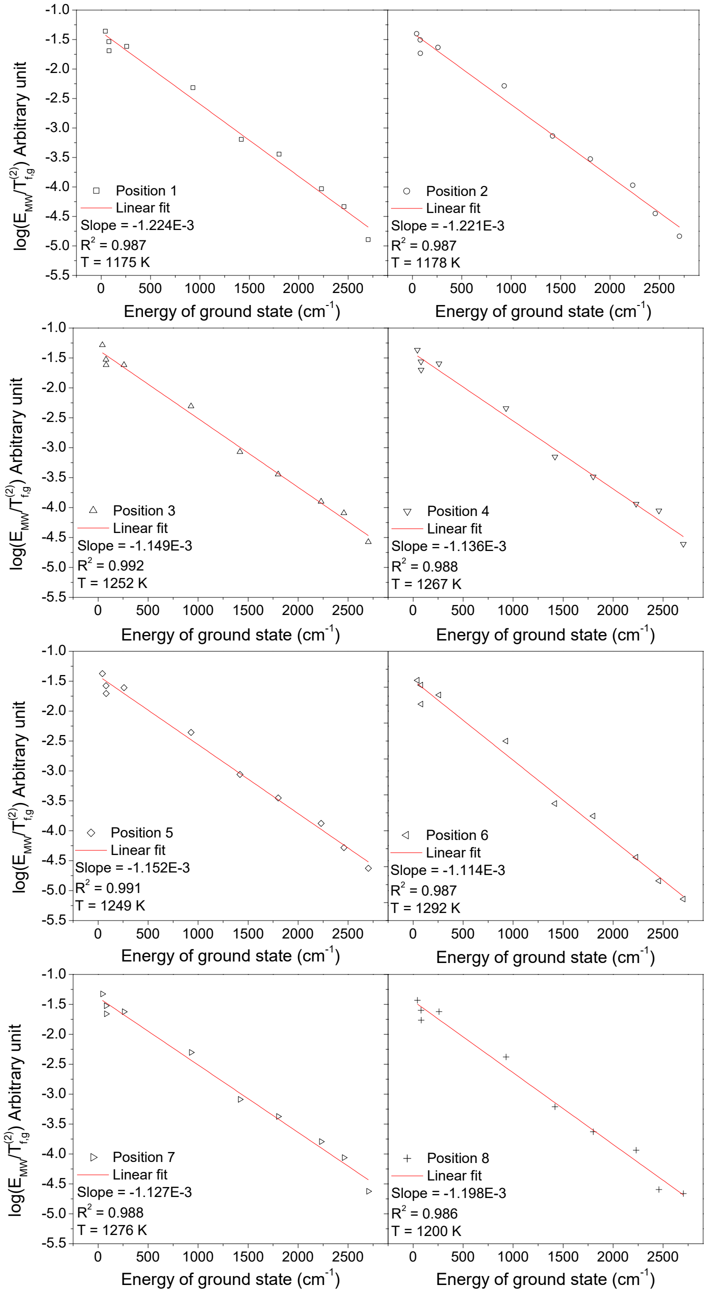

Figure 36. Boltzmann plots at the eight axial locations in the atmospheric microdischarge.

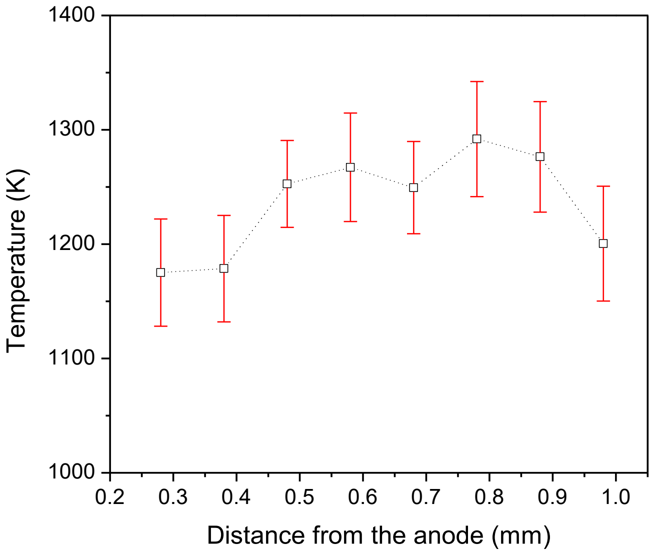

Figure 37. The temperature distribution in the microdischarge was determined by eight points between anode and cathode at equal intervals of 0.10 mm.

CHAPTER VI

ATOMIC OXYGEN MEASUREMENTS IN A LOW PRESSURE DC AND PULSED DISCHARGE VIA RADAR REMPI

Abstract

This chapter presents relative atomic oxygen concentration measurements in low pressure direct current (DC) and pulsed discharges produced in oxygen/helium gas mixtures. These measurements were made by coherent microwave Rayleigh scattering from resonance enhanced multiphoton ionization (REMPI) of atomic oxygen. The 225.6 nm laser wavelength corresponded to a 2+1 REMPI transition utilizing the O $2p^33p(^3P)$ electronically excited state. The low pressure DC and pulsed discharges are characterized over a range of pressures, gas compositions, and discharge voltages. Temporal and spatial profiles of relative atomic oxygen concentration of the pulsed discharge are compared to those made in a similar apparatus via two-photon absorption laser induced fluorescence (TALIF). A method by which quantitative measurement of atomic or radical species concentrations in a discharge environment can be made via dielectric calibration of Radar REMPI is discussed. This technique appears to be a viable alternative to the tunable diode laser absorption spectroscopy (TDLAS) and two-photon absorption laser induced fluorescence (TALIF) methods.

Introduction

There is an ever growing interest in non-equilibrium plasma discharges due to the potential applications in plasma assisted combustion[1, 2], flow control[2], biomedical applications[3], manufacturing[4], arc jet flow heating[5]. However, due to the diversity of the applications of non-equilibrium plasma, there are many experimental difficulties in implementing diagnostics. First, many non-equilibrium plasma discharge devices have small volumes and limited optical access. Additionally, many of these applications involve a wide range of pressures from vacuum to several atmospheres and temperatures from atmospheric to several thousand kelvin. Production of chemical intermediates, such as radical and atomic species, greatly influences many aspects of non-equilibrium plasma discharges and the nearby environment such as: kinetics, electron density, and thermochemistry.

The primary techniques used to determine radical and atomic species concentrations in discharge environments are tunable diode laser absorption spectroscopy (TDLAS) and two-photon absorption laser induced fluorescence (TALIF). TDLAS has been used to measure a wide range of radical species concentrations and kinetics for non-equilibrium plasma discharges in molecular gas mixtures [6-8]. The major limitation of TDLAS is that it is a line-integrated technique, and thus, it cannot be used to probe species in inhomogeneous environments. TALIF has been used to measure atomic species such as: H, O, and N [9-11]. TALIF is not applicable to high-pressure environments due to rapid collisional quenching of the excited states. Both optical techniques can be difficult to implement in "real" facilities such as arc jets.

Coherent microwave scattering (Radar) from small volume plasmas generated by Resonance Enhanced Multiphoton Ionization (REMPI) has rapidly grown as a diagnostic technique since being first proposed nearly a decade ago [12, 13]. This growth is due largely to the benefits of separating the optical plasma generation from the standoff microwave detection, which allows the Radar REMPI system to be easily implemented and also less sensitive to the external environment than fully optical techniques. Detection of trace species such as NO, CO, Xe, Ar in static gas mixtures [14] and CH_3 in a methane/air flame [15] via Radar REMPI has been demonstrated. Kinetic measurements have also been done by utilizing the decay of the Radar REMPI signal. This has been demonstrated by electron loss rate measurements in air [16] and sodium-argon cluster ion recombination rates [17]. O_2 rotational temperature measurement via Radar REMPI has been used to measure gas [18], flame [19], and DC discharge [20] temperatures. Atomic oxygen concentration measurements in a flame were performed using Radar REMPI [21]. As pointed out in this study, photo-dissociation of molecular oxygen can lead to erroneous measurements of atomic oxygen concentrations. Utilizing REMPI from a second gas for calibration, such as xenon, adds significant uncertainty into the concentration measurement. This uncertainty is due to the difficulty in accurately determining the REMPI cross-sections of the target and calibration species. In this work we will present relative atomic oxygen concentration measurements in a low pressure O_2/He DC and pulsed discharge via Radar REMPI. A 2+1 REMPI scheme of atomic oxygen is utilized. The technique of using dielectric calibration to obtain absolute concentration measurements will be presented. The influence of gas composition, laser pulse energy, and pressure on the measurement technique will be explored. It will be shown that for prescribed laser intensities, direct measurement of atomic oxygen can be separated from photo-dissociation. Methodology for separating electrons generated via the REMPI process from those present in the DC and pulsed discharge will be presented. Overall, this work will demonstrate Radar REMPI as a novel technique for making absolute concentration measurements of trace species in non-equilibrium plasma discharges.

Experimental Setup

A sketch of the experimental setup used in this work shown in Figure 38. A frequency doubled Nd:YAG laser (Continuum Surelite SI-10) was used to pump a tunable dye laser (Continuum ND6000, DCM, [2-[2-[4-(dimethylamino)phenyl]ethenyl]-6-methyl-4H- pyran-4-ylidene]-propanedinitrile, $C_{19}H_{17}N_3O$ as the dye) to generate output at 619 nm. The output wavelengths were tunable from 615 to 620 nm, with output power ranging from 10-20 mJ/pulse. The dye laser output is mixed with a 355 nm beam (in BBO) to generate the required UV wavelength of 225 nm with laser energy of 50 – 400 μJ per pulse. The laser output was then focused by a lens with a focal length of 50 cm to generate the REMPI plasma in the discharge cell. The beam height was adjustable by using a mirror pair with the top mirror and the 50 cm lens mounted on a vertical stage. The 2+1 REMPI scheme used in this work is shown in Figure 39.

The flow system consisted of a 200 mL/min (Omega – FMA5510) and a 2 L/min (Omega – FMA5516) to deliver ultra-high purity oxygen and helium respectively. The gases were mixed roughly a meter before entering the discharge cell. A piezoelectric pressure (Kurt J. Lesker – 910) sensor was used to determine the gas pressure shortly before the discharge cell. The desired pressure in the system was obtained by manually adjusting a needling valve to the vacuum pump. The discharge cell consisted of a stainless steel 6-way cross with cf-flanges. Two of the flanges had quartz windows applied with vacuum epoxy. These windows allowed for propagation of the laser beam and microwave into the discharge cell. Two other flanges had ¼ inch Swagelok fittings to allow connection with the flow system. The top and bottom flanges had copper rod electrodes that were electrically isolated from the discharge cell but through the flanges. The electrodes were in a modified pin-to-pin arrangement with hemispherical heads with diameters of 6.35 mm and separated by 8 mm. Photos of the pulsed and DC discharges are displayed in Figure 40.

The same microwave detection system was used for all work presented. A microwave homodyne transceiver detection system, shown in Figure 41, was used to detect the REMPI plasma. A 10 dBm tunable microwave source (HP 8350B sweep oscillator, set at ~10 GHz) was first split into two channels. One channel was used to illuminate the ionization point through a microwave horn (WR75, 15 dB gain). Microwave scattering from the plasma was collected by the same microwave horn. The received microwave passed through a microwave circulator and was amplified 30 dB by one preamplifier at approximately 10 GHz. After the frequency was down converted in the mixer, two other amplifiers with bandwidth of 2.5 kHz to 1.0 GHz amplified the signal by another factor of 60 dB. It should be noted that the filter after the mixer can effectively block the scattering background from the environment. Therefore, Radar REMPI measurements inside an enclosure will not suffer from surface scattering interference. From the geometry of dipole radiation, the polarization of the microwave was chosen to be along the propagation direction of the laser to maximize the scattering signal.

Dielectric Calibration

The derivation of a dielectric calibration process beings with the general ohm's law (considering only magnitudes) which gives:

$$\mathrm{J} = \sigma \mathrm{E} \tag{1}$$

The current density (current per unit area) is defined by:

$$\mathrm{J} = \text{-}n_e e v \tag{2}$$

For a dielectric, polarization occurs when an electric field is applied. The relationship for a time varying field of a single frequency applied to a homogenous linear material is given by:

$$\begin{gathered} P(t) = \chi(\omega)\epsilon_0 E(t) \\ P(\omega)e^{i\omega t} = \chi(\omega)\epsilon_0 E(\omega)e^{i\omega t} \\ P(\omega) = \chi(\omega)\epsilon_0 E(\omega) \end{gathered} \tag{3}$$

The electric susceptibility is then defined as:

$$\chi(\omega) = \epsilon_r(\omega)\text{-}1 \tag{4}$$

Using this definition:

$$P = \epsilon_0(\epsilon_r\text{-}1)E_i \tag{5}$$

Defining the polarization in terms of the number of dipoles per unit volume gives:

$$P = n_e e d(\omega) \tag{6}$$

Where $d(\omega)$ is the oscillation distance. Then it can be determined:

$$-n_e e d(\omega) = \epsilon_0(\epsilon_r\text{-}1)E_i \tag{7}$$

Dividing by the period, T_{osc},of the electron oscillation and comparing with Ohm's law yields the current generated by the electric field (A is the area):

$$I_0 = J \cdot A \approx \frac{n_e e \cdot d(\omega)}{T_{osc}} A = \frac{\epsilon_0(\epsilon_r\text{-}1)E_i}{T_{osc}} A = [\epsilon_0(\epsilon_r\text{-}1)\omega A)]E_i \tag{8}$$

Note that it is assumed that the oscillation frequency of the electron matches the frequency of the incident electromagnetic wave. The scattered field is given by:

$$E_S \propto \frac{\sin(\phi)}{R} I_0 l\omega \tag{9}$$

Upon inserting Eq. 8 into Eq. 9, the scattered field is given by:

$$E_S \propto \frac{\sin(\phi)}{R} [\epsilon_0(\epsilon_r\text{-}1)\omega AE_i)]l\omega \tag{10}$$

$$E_S \propto \frac{E_i \sin(\phi)}{R} \epsilon_0(\epsilon_r\text{-}1)\omega^2 Al \tag{11}$$

Defining the volume as $V = Al$ and noting that the amplitude of the indident field, E_i, is only a function of frequency and is therefore constant for a fixed frequency it can be seen that:

$$E_S \propto \frac{E_i \sin(\phi)}{R} \epsilon_0(\epsilon_r\text{-}1)\omega^2 V \tag{12}$$

Now let β be the constant of proportionality so that:

$$E_S = \frac{\beta E_i \sin(\phi)}{R\epsilon_0(\epsilon_r\text{-}1)} \omega^2 V \tag{13}$$

Since the measured voltage is proportional to the scattered electric field (i.e. $U \propto E_S$) then it can be shown that:

$$U = \left[\frac{\gamma\beta E_i \sin(\phi)}{R}\right] \epsilon_0(\epsilon_r\text{-}1)\omega V \tag{14}$$

Finally the dielectric calibration constant can be defined as:

$$A_c = \frac{\gamma\beta E_i \sin(\phi)}{R} \omega \tag{15}$$

The microwave scattering signal from the detection system can be written for the limiting cases of a perfect conductor or a perfect dielectric scatterer placed in the microwave illumination region as follows:

$$U = \begin{cases} A\sigma V, & \text{for perfect conductor} \\ A\varepsilon_0(\varepsilon_r\text{-}1)\omega V, & \text{for dielectirc} \end{cases} \tag{16}$$

where U is the microwave signal, A is the characteristic parameter of the microwave detection system, σ is the electric conductivity of the scatter, ε is the permittivity of the scatter, ε_0 is the free space permittivity, ω is the angular frequency of microwave, and V is the volume of the scatterer, respectively. By placing a sample with known dielectric properties within the illumination region one may determine the microwave detection system characteristic A at the sample's location. A small cylindrical sample of a dielectric material such as alumina was mounted at the laser beam focal point with the cylinder's axis parallel to the laser's propagation direction. This dielectric calibration approach slightly differed from the previous work[22], which used dielectrics launched through the microwave illumination region.

A sample microwave scattering signals from alumina and PTFE are shown in Figure 42. The measurement of A should be more accurate with the use of alumina due to its larger ε value leading to a stronger scattering signal. With the same detection system and experimental setup, the temporal evolutions of electron density from laser sparks are also shown in Figure 42 with the laser energy input of 70, 35 and 16 mJ at 1064, 532 and 355 nm, respectively. By using the system parameter A and making the approximation that the plasma column is roughly the same size as the laser beam focal region, one can determine the conductivity of the plasma column from the microwave signal. The electron density in the plasma can then be determined by using the expression:

$$\sigma = 2.82 \times 10^{-4} n_e \nu_m (\omega^2 + \nu_m^2) \Omega^{-1}\ \text{cm}^{-1} \tag{17}$$

where ν_m is the frequency of electron-neutral collisions $\nu_m \approx 2 \times 10^9 p[\mathrm{Torr}], s^{-1}$, n_e is the electron density (cm^{-3}), and ω is the angular frequency (s^{-1}) [23].

The characteristic parameter A is highly dependent on the location of the scatter relative to the microwave horn. However for a given system, it is possible to obtain a spatial mapping of the calibration *ex-situ*. This methodology would allow for the implementation of a highly robust Radar REMPI system.

Results

Dielectric Calibration

Using an alumina cylinder of 3.1 mm in diameter and 22.1 mm in length as a microwave scatter resulted in a microwave scattering signal of 0.5 mV. An estimate for the plasma column diameter equal to the Gaussian beam waist of 125 µm was used to calculate a calibration for electron density measurement of $1.97 \times 10^{14} \frac{\mathrm{cm}^{-3}}{100\mathrm{mV}}$. This estimation gives a measured electron number density on the order of 1×10^{13} cm^{-3} for the REMPI plasma in this work. The fraction of ionization calculated by the ratio of the electron number density to the atomic oxygen number density is given by

$$\frac{n_e}{n_O} = \sigma^i \sigma^2 F^3 e^{\left(-\frac{kT}{E_0}\right)} \qquad (18)$$

where σ^i is the one photon ionization cross section, σ^2 is the two-photon excitation cross-section, F is the photon flux, and $e^{\left(-\frac{kT}{E_0}\right)}$ is the Boltzmann factor taken to be 1 here. Values of these cross sections were reported to be $3.30 \times 10^{-19} \mathrm{cm}^2$ and $2.66 \times 10^{-35} \mathrm{cm}^4$ for ionization and excitation, respectively.[24] Using the previously mentioned Gaussian beam waist and a typical laser energy of 200 μJ/pulse one obtains a factiously high fraction of ionization at 62.5%. The factiously high fraction of ionization is most likely due to a laser beam radius that is larger than the estimated Gaussian beam waist. Attempts were made to measure the laser beam radius using laser burn paper but were not successful due to the low laser energy and size of the beam. It can be shown that the measurement of absolute atomic oxygen number density has a relation to the laser beam radius, r, given by:

$$n_O \sim r^6 \tag{19}$$

This large dependence on r causes even small inaccuracies in the laser beam radius to significantly change the measured atomic oxygen density for the dielectric calibration technique. For this reason all results below are presented as normalized electron densities. The results are normalized to the relevant maximum signal in order to allow us to make conclusive remarks on the characterization of atomic oxygen production in the DC and pulsed discharges.

DC Discharge

Figure 43 shows a typical atomic oxygen REMPI spectrum. Measurements were taken in a 5% O_2/He mixture at 25 Torr with and without the 4 kV DC discharge on. The spectrum was taken 1 mm from the anode along the length of the discharge gap. With the discharge on, a single peak is observed at 225.6 nm corresponding to the 2+1 atomic oxygen REMPI scheme outlined previously. Additionally, there is a small peak observed at 225.63 that most likely corresponds to NO produced in the discharge. This would indicate a small air leak into discharge cell.

Figure 44 shows microwave scattering signal versus laser energy squared. These measurements were taken in a 4 kV DC discharge 1 mm from the anode produced in a 5% O_2/He mixture at 25

Torr. A linear fit was applied to the data to assess its linearity. Although a significant amount of scatter is seen in the measurements, the data most closely follows a linear trend attributed to the two-photon excitation process. If a higher order photon process, namely photo-dissociation of molecular oxygen followed by REMPI of atomic oxygen, was the dominant mechanism one would observe a signal dependence on laser energy of cubed or higher. The spectrum most likely indicates that direct Radar REMPI measurement of atomic oxygen produced in the DC discharge is observed here.

Figure 45 shows normalized atomic oxygen density measurements versus (a) % O_2 in a He mixture at 25 Torr and 4 kV supplied voltage, (b) pressure in a 5% O_2/He mixture at 4 kV supplied voltage, and (c) supplied voltage in a 5% O_2/He mixture at 25 Torr. All three data sets were taken 1 mm from the anode. A peak in the atomic oxygen density is observed near 30% O_2/He mixture. Enhanced quenching of atomic oxygen via ozone formation at higher molecular oxygen densities could lead to lower the decrease in atomic oxygen density. This same effect is prevalent in the pressure dependence measurements shown in Figure 45(b). At pressures above 20 Torr the atomic oxygen density appears to rapidly decrease with increasing pressure. Along with the formation of ozone, collisional quenching leading to O_2 formation decreases the atomic oxygen density. Figure 45(c) shows that the atomic oxygen increases with increasing discharge supplied voltage. Increasing the supply voltage increases the strength of the electric field. This in turn leads to a stronger electron avalanche and larger electron densities. Since the primary mechanism for atomic oxygen generation is dissociative recombination of O_2^+, the atomic oxygen density is highly dependent on the discharge supply voltage.

Figure 46 shows normalized atomic oxygen density spatial profile in a 4 kV DC discharge produced in a 5% O_2/He mixture at 25 Torr. The peak atomic oxygen density is observed near the anode, which can most likely be attributed to the elevated electron number densities near the electrode surface due to cascading effect of the electron avalanche within the discharge gap. Another uptick in the atomic oxygen density is seen near 1.75 mm from the anode. One possibility for this would be the formation of a "hotspot" of higher electron density, leading to the higher atomic oxygen density. Near the cathode, the atomic oxygen density rapidly increases, which is likely due to the formation of a plasma sheath of higher ionic density near the surface of the electrode.

Pulsed Discharge

Figure 47 shows typical voltage and current waveforms for the pulsed discharge. These measurements were taken in a 1% O_2/He mixture at 100 Torr and supplied voltage of 4 kV. The gate of the pulse can be seen to be roughly 200 ns wide with peaks in voltage and current observed after 150 ns. A peak voltage across the discharge gap of around 2.3 kV, meaning a 1.7 kV voltage drop at the 1 k-Ohm resistor and within the other elements of the circuit is obtained. A 2.3 ampere peak current is observed. This peak current is significantly higher than the operating current of the DC discharge and will lead to much higher atomic oxygen densities in the discharge.

Figure 48 shows a typical atomic oxygen REMPI spectrum in the pulsed discharge at 1 mm from the anode and 80 microseconds from the start of the pulse discharge. The measurements were taken in a 1% O_2/He mixture at 100 Torr with the 4 kV pulsed discharge off and on. With the discharge on, a peak at 225.6 nm is observed and corresponds to the 2+1 REMPI of atomic oxygen. A large disparity is seen at the off-resonance wavelengths between the discharge on and off curves. The large off-resonance signal is due to the microwave scattering from the electrons produced in the pulsed discharge.

Figure 49 shows temporal profiles of normalized atomic oxygen density in a pulsed discharge for various (a) Pressure, (b) and supplied voltage, (c) %O_2 in He mixture. For all three data sets, there is an early time frame after the pulsed discharge where significant microwave shielding occurs leading to much lower atomic oxygen density measurements. For most of the cases shown below, this shielding time frame occurs around the first 50 microseconds following the pulse discharge. The notable exception being the 0.5% O_2/He mixture case in Figure 49(c), which appears to show significant shielding out to 2000 microseconds after the pulsed discharge. The peak in measured atomic oxygen density is observed after sufficient losses in the background electrons occur to allow for the microwaves to penetrate the REMPI plasma. Following this peak, the atomic oxygen density follows an exponential decay until the next cycle of the pulsed discharge.

Figure 50 shows microwave scattering from the background electrons produced in the pulsed discharge versus time. Typical Radar REMPI signal for a laser pulse at 80 microseconds after the start of the pulsed discharge. These measurements were taken for a 1% O_2/He mixture at 100 Torr with a supplied voltage of 4 kV. The amplitude of the microwave scattering signal with the first 50 microseconds peaks at over 2 volts, significantly larger than the superimposed Radar REMPI signal. Additionally, such high scattering signals correspond to electron densities that will not be fully penetrable to the microwaves and will lead to erroneously low atomic oxygen density measurements.

Figure 51 shows spatial profile of atomic oxygen density normalized for various pressures in a 4 kV pulsed discharge in 1% O_2/He mixture. Measurements were taken 1 mm from the anode. For all three pressure conditions, the peak in atomic oxygen density is observed close to the anode. Approaching the center of the discharge the atomic oxygen density decreases before finally increasing near the cathode. The same boundary effects mentioned for the spatial profiles observed for the DC discharge are observed here.

Figure 52 shows atomic oxygen REMPI signal versus laser energy squared with a linear fit. This measurement was taken at 1 mm from the anode in a 1% O_2/He mixture at 100 Torr with a 4 kV supply voltage. A linear trend to the measurement is much more apparent for the pulsed discharge. The higher atomic oxygen densities in the pulsed discharge lead to a better signal to noise ratio for the measurement.

Figure 53 shows normalized atomic oxygen density measurements in a pulsed discharge versus (a) pressure for a 1% O_2/He mixture at 4 kV supply voltage, (b) supplied voltage for a 1% O_2/He mixture at 100 Torr, and (c) %O_2 in He mixture at 100 Torr and 4 kV supply voltage. Similar to the DC discharge, increasing pressure leads to a decrease in the observed atomic oxygen density due to collisional losses and the formation of ozone. Similarly to DC discharge, and increase in the supplied voltage to the pulsed discharge leads to enhanced electron avalanche and thus higher atomic oxygen densities. As mentioned for the DC discharge measurements, this is most likely due to enhanced electron production due to the stronger electric field at higher supply voltages. Increased atomic oxygen density is observed for increasing % O_2/He mixtures. Unfortunately, measurements greater than 5 % O_2 in the He mixture were not taken here.

Figure 54 shows comparisons of atomic oxygen measurements made via Radar REMPI and TALIF techniques. Both sets of measurements were made in a 4 kV pulsed discharge produced in a 1% O_2/He mixture at 100 Torr. Figure 54(a) shows a comparison of the spatial profile in two similar discharges. Figure 54(b) shows a comparison of the temporal profiles with exponential curve fits and their corresponding 1/e time constants. Measurements were taken at 1 mm from the anode for the two techniques.

Conclusions

In this chapter relative atomic oxygen concentration measurements in low pressure direct current (DC) and pulsed discharges produced in oxygen/helium gas mixtures were presented. Coherent microwave Rayleigh scattering from resonance enhanced multiphoton ionization (REMPI) of atomic oxygen was utilized for these measurements. A 2+1 REMPI scheme was employed using a 225.6 nm laser wavelength corresponding to a two photon transition to the O $2p^33p(^3P)$ electronically excited state. The effects of pressure, gas composition, and discharge voltages on atomic oxygen concentration were explored for the low pressure DC and pulsed discharges are characterized over a range of pressures, gas compositions, and discharge voltages. Comparisons between Radar REMPI and two-photon absorption laser induced fluorescence (TALIF) techniques were made for the measured temporal and spatial profiles of relative atomic oxygen concentration in a pulsed. Dielectric calibration of Radar REMPI was presented as a method by which quantitative measurement of atomic or radical species concentrations in a discharge environment can be made. Although this technique relies on careful determination of the laser beam radius, it appears to be a viable alternative to the measurement of atomic or radical species concentrations in a discharge environment.

Acknowledgments

The work at the University of Tennessee Knoxville was supported by AFRL.

References

1. Sun, W., Non-equilibrium Plasma-Assisted Combustion. 2013.

2. Adamovich, I.V., et al., *Plasma assisted ignition and high-speed flow control: non-thermal and thermal effects.* Plasma Sources Science and Technology, 2009. **18**(3): p. 034018.

3. Lu, X., M. Laroussi, and V. Puech, *On atmospheric-pressure non-equilibrium plasma jets and plasma bullets.* Plasma Sources Science and Technology, 2012. **21**(3): p. 034005.

4. Babayan, S.E., et al., Deposition of silicon dioxide films with a non-equilibrium atmospheric-pressure plasma jet. Plasma Sources Science and Technology, 2001. **10**(4): p. 573.

5. Laux, C.O., et al., *Optical diagnostics of atmospheric pressure air plasmas.* Plasma Sources Science and Technology, 2003. **12**(2): p. 125.

6. Lombardi, G., et al., Quantitative detection of methyl radicals in non-equilibrium plasmas: a comparative study. Plasma Sources Science and Technology, 2004. **13**(1): p. 27.

7. Pipa, A.V., et al., Absolute production rate measurements of nitric oxide by an atmospheric pressure plasma jet (APPJ). Journal of Physics D: Applied Physics, 2008. **41**(19): p. 194011.

8. Welzel, S., et al., *Kinetic and Diagnostic Studies of Molecular Plasmas Using Laser Absorption Techniques.* Journal of Physics: Conference Series, 2007. **86**(1): p. 012012.

9. Schmidt, J.B., Ultrashort Two-Photon-Absorption Laser-Induced Fluorescence in Nanosecond-Duration, Repetitively Pulsed Discharges. 2015, The Ohio State University.

10. Stancu, G.D., et al., *Atmospheric pressure plasma diagnostics by OES, CRDS and TALIF.* Journal of Physics D: Applied Physics, 2010. **43**(12): p. 124002.

11. Sun, W., et al., Kinetic effects of non-equilibrium plasma-assisted methane oxidation on diffusion flame extinction limits. Combustion and Flame, 2012. **159**(1): p. 221-229.

12. Zhang, Z., M.N. Shneider, and R.B. Miles, *Coherent Microwave Rayleigh Scattering from Resonance-Enhanced Multiphoton Ionization in Argon.* Physical Review Letters, 2007. **98**(26): p. 265005.

13. Shneider, M.N., Z. Zhang, and R.B. Miles, *Plasma induced by resonance enhanced multiphoton ionization in inert gas.* Journal of Applied Physics, 2007. **102**(12): p. 123103.

14. Dogariu, A. and R.B. Miles, Detecting localized trace species in air using radar resonance-enhanced multi-photon ionization. Applied Optics, 2011. **50**(4): p. A68-A73.

15. Wu, Y., et al., Direct measurement of methyl radicals in a methane/air flame at atmospheric pressure by radar REMPI. Optics Express, 2011. **19**(24): p. 23997-24004.

16. Dogariu, A., M.N. Shneider, and R.B. Miles, *Versatile radar measurement of the electron loss rate in air.* Applied Physics Letters, 2013. **103**(22): p. 224102.

17. Wu, Y., et al., Measurement of sodium-argon cluster ion recombination by coherent microwave scattering. Applied Physics Letters, 2012. **100**(11): p. 114108.

18. Wu, Y., Z.L. Zhang, and S.F. Adams, *O(2) rotational temperature measurements by coherent microwave scattering from REMPI.* Chemical Physics Letters, 2011. **513**(4-6): p. 191-194.

19. Wu, Y., et al., Flame temperature measurements by radar resonance-enhanced multiphoton ionization of molecular oxygen. Appl. Opt., 2012. **51**(28): p. 6864-6869.

20. Sawyer, J., et al., O2 rotational temperature measurements in an atmospheric air microdischarge by radar resonance-enhanced multiphoton ionization. Journal of Applied Physics, 2013. **113**(23): p. 233304.

21. Tat Loon, C. and M. Richard, Absolute concentration measurements of atomic oxygen in a flame using radar REMPI, in 52nd Aerospace Sciences Meeting. 2014, American Institute of Aeronautics and Astronautics.

22. Shashurin, A., et al., Temporary-resolved measurement of electron density in small atmospheric plasmas. Applied Physics Letters, 2010. **96**(17): p. 171502.

23. Raizer, Y.P., *Gas Discharge Physics*, ed. J.E. Allen. 1991: Springer-Verlag Berlin Heidelberg. 449.

24. Bamford, D.J., L.E. Jusinski, and W.K. Bischel, *Absolute two-photon absorption and three-photon ionization cross sections for atomic oxygen.* Physical Review A, 1986. **34**(1): p. 185-198.

Appendix

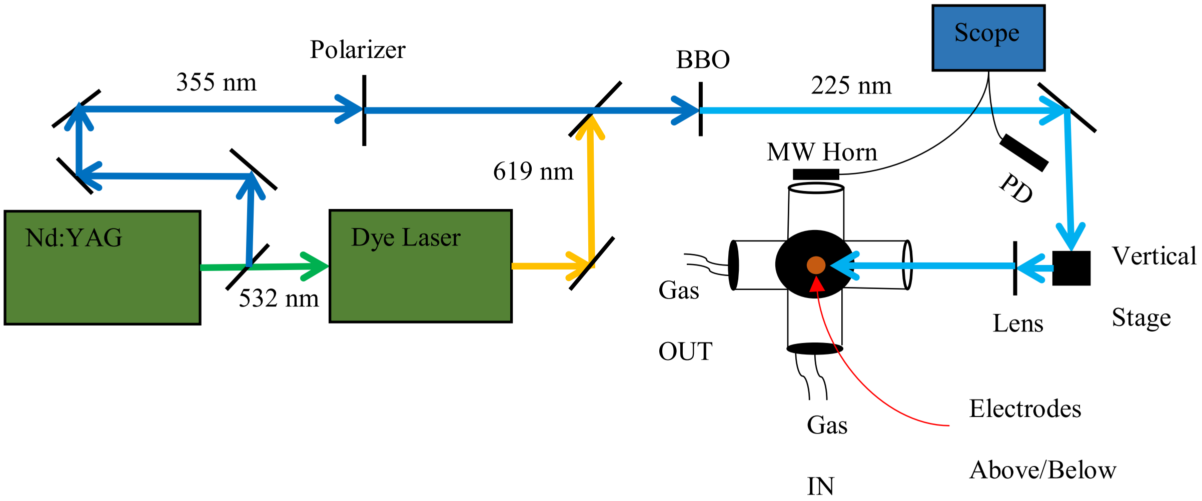

Figure 38. Sketch of experimental setup used for atomic oxygen concentration measurements in O_2/He DC and pulsed Discharge

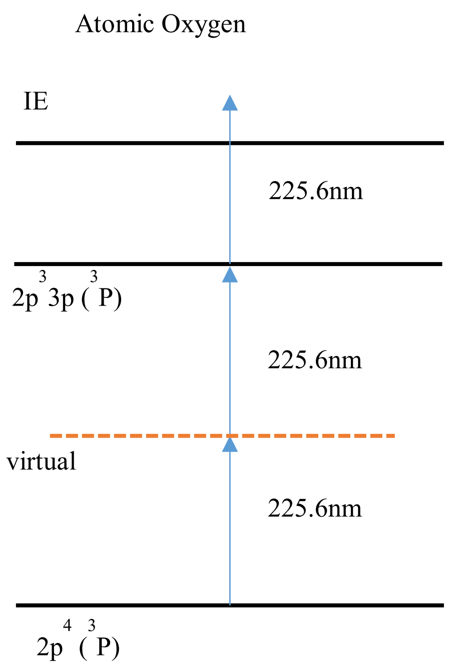

Figure 39. Energy level diagram depicting radar REMPI transitions for (2+1) atomic oxygen O.

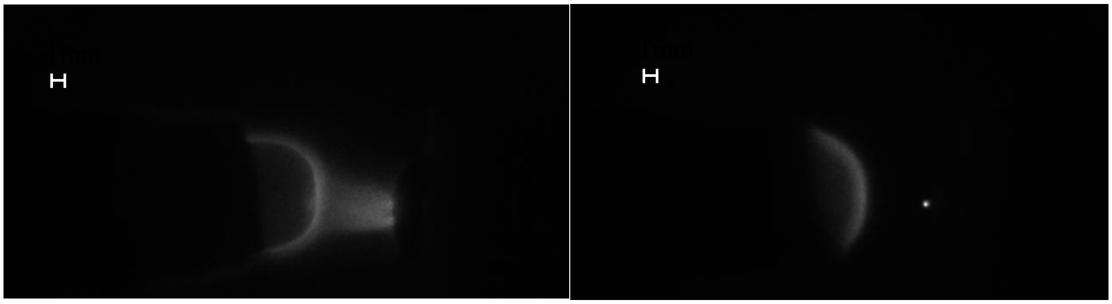
(a) (b)

Figure 40. Photos of discharge in a 1% O_2/He mixture with 50 ns exposure time (a) pulsed and (b) DC discharge.

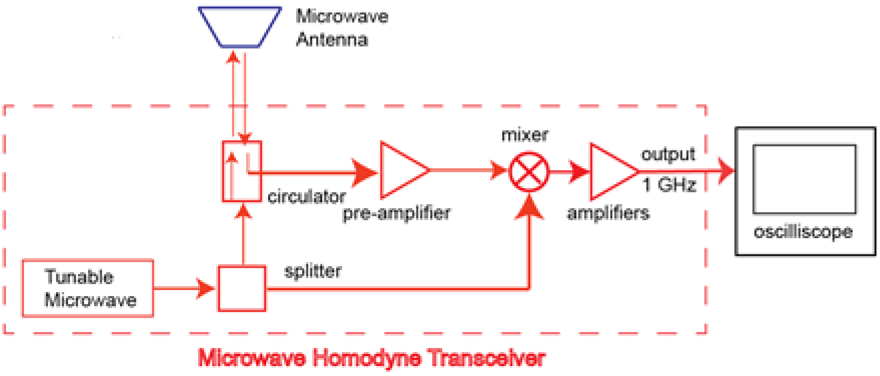

Figure 41. Microwave homodyne detection system.

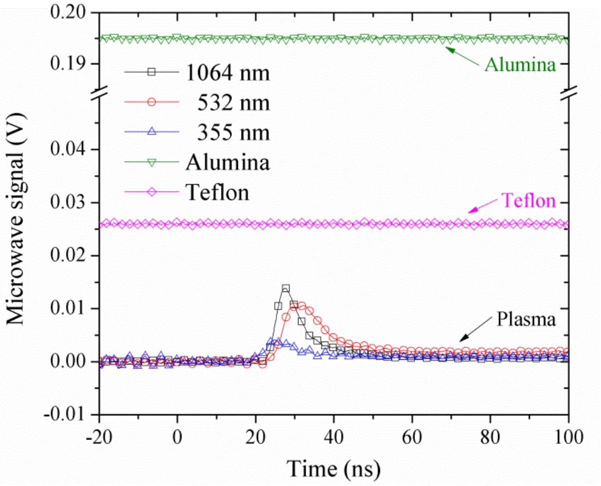

Figure 42. The microwave scattering signals from dielectric materials (alumina and PTFE) and laser-induced air breakdown by using 1064, 532, and 355 nm laser beam, respectively.

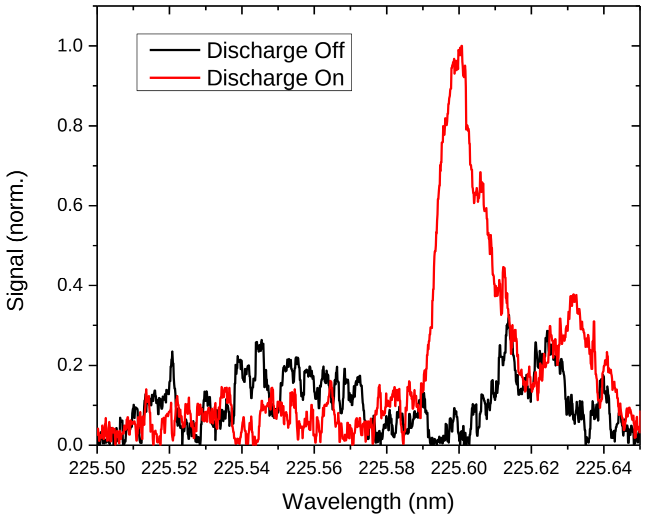

Figure 43. Atomic oxygen REMPI spectrum with the 4 kV DC discharge off and on in a 5% O_2/He mixture at 25 Torr. Spectrum was taken 1 mm from the anode.

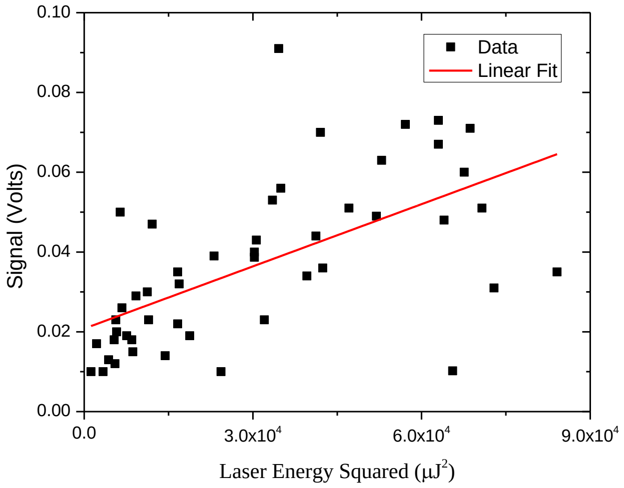

Figure 44. Microwave scattering signal versus laser energy squared with a linear fit. Measurements were taken 1 mm from the anode in a 5% O_2/He mixture at 25 Torr and 4 kV.

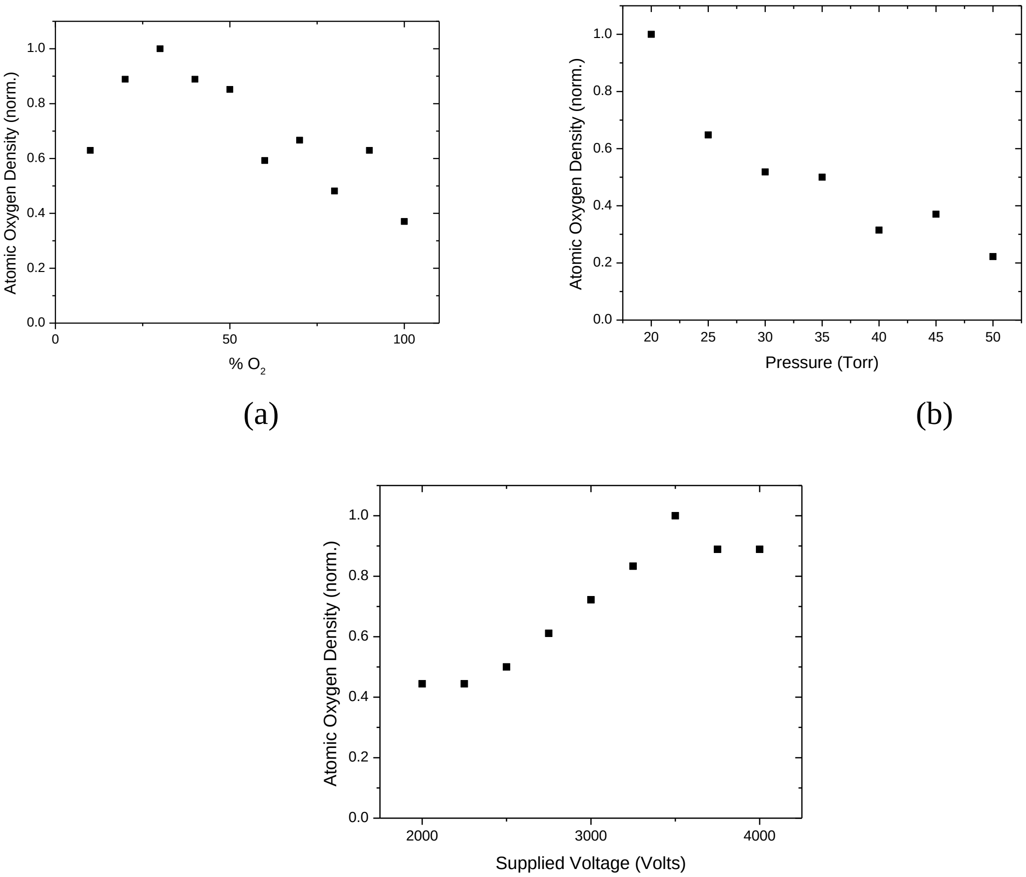

(a)

(b)

(c)

Figure 45. Microwave scattering signal versus (a) % O_2 in a He mixture at 25 Torr and 4kV, (b) Pressure in a 5% O_2/He mixture and 4kV, and (c) Supplied Voltage in a 5% O_2/He mixture at 25 Torr. All three data sets were taken 1 mm from the anode.

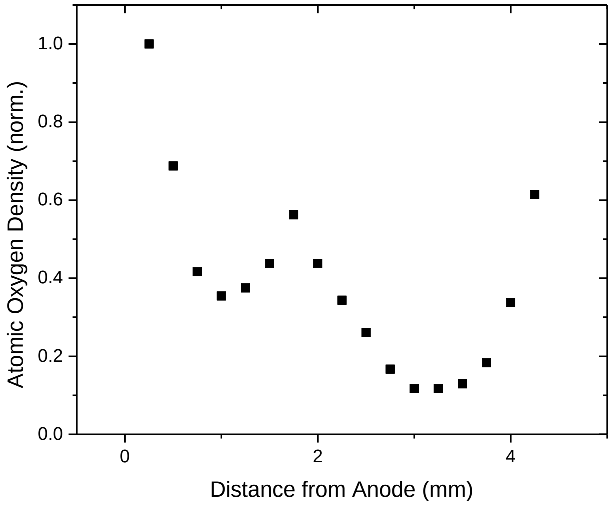

Figure 46. Microwave scattering signal along the length of the discharge gap for 5% O_2/He at 25 Torr and 4 kV supplied voltage.

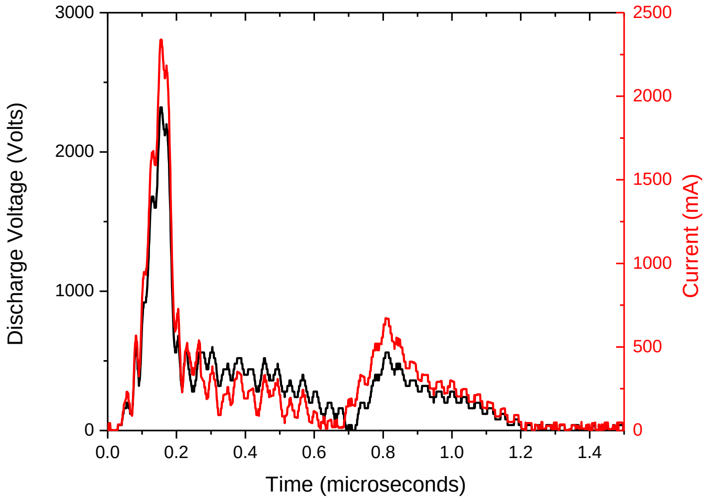

Figure 47. Pulsed discharge voltage and current waveforms in a 1% O_2/He mixture at 100 Torr and set supplied voltage of 4 kV.

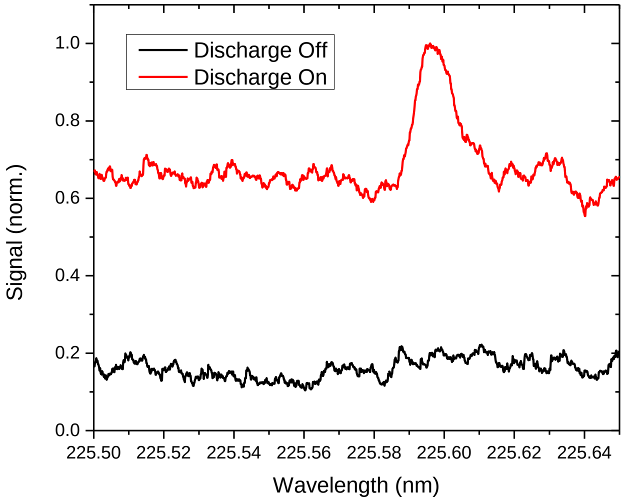

Figure 48. Atomic oxygen REMPI spectrum at 1 mm from the anode in a 1% O_2/He mixture at 100 Torr with the pulsed discharge off and on.

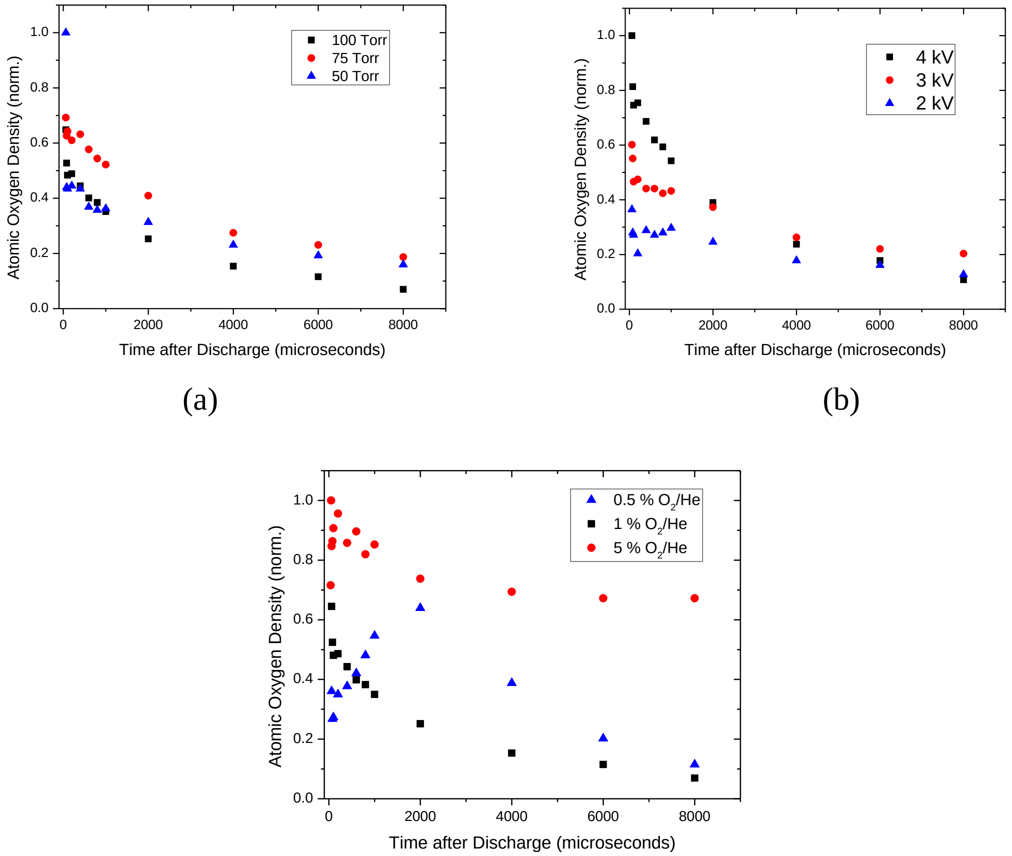

(a)

(b)

(c)

Figure 49. Temporal profiles of normalized atomic oxygen density in pulsed discharge for various (a) Pressure, (b) and supplied voltage, (c) %O_2 in He mixture.

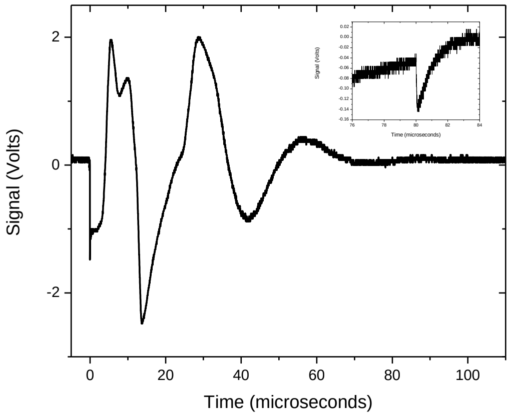

Figure 50. Microwave scattering from electrons produced in pulsed discharge versus time. Typical Radar REMPI signal for a laser pulse at 80 microseconds after the start of the pulsed discharge.

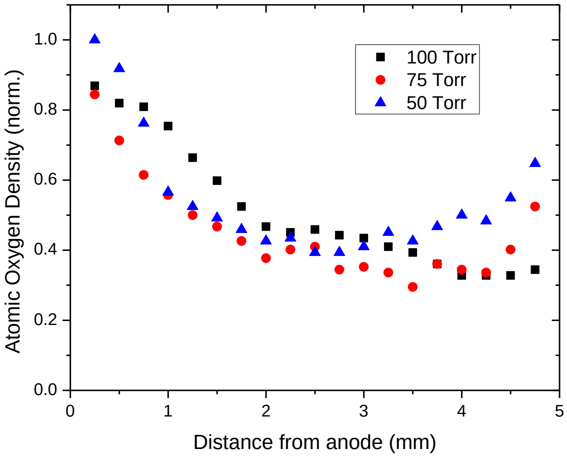

Figure 51. Spatial profiles of normalized atomic oxygen density 80 microseconds after the 4 kV pulsed discharge for various pressures in a 1% O_2/He mixture. Measurements were taken 1 mm from the anode.

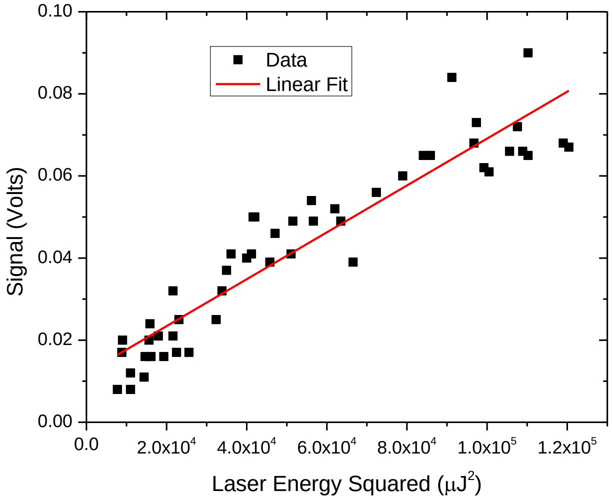

Figure 52. Atomic oxygen REMPI signal versus laser energy squared with linear fit. Measurements were taken 80 microseconds after the discharge at 1 mm from the anode in a 1% O_2/He mixture at 100 Torr and 4 kV supply voltage.

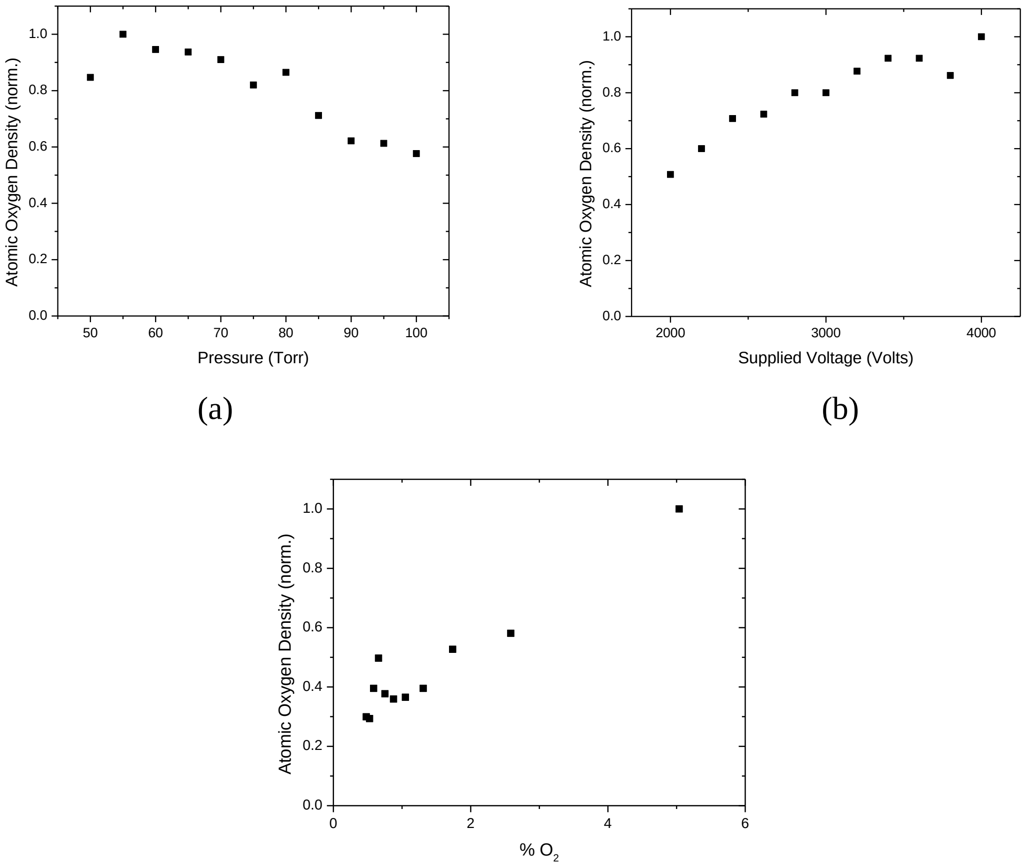

(a)

(b)

(c)

Figure 53. Normalized atomic oxygen density in pulsed discharge versus (a) pressure in a 1% O_2/He mixture at a 4 kV supply voltage , (b) supplied voltage for a 1% O_2/He mixture at 100 Torr, and (c) %O_2 in He mixture at 100 Torr and 4 kV supply voltage. These measurements were taken 1 mm from the anode and 80 microseconds after the discharge.

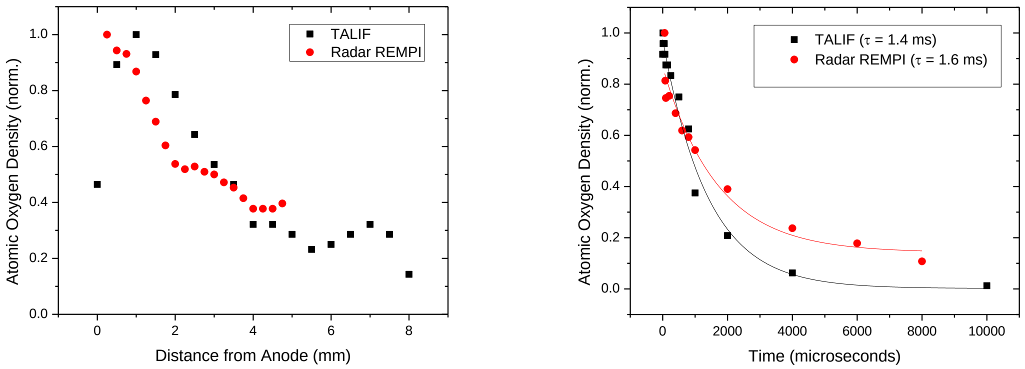

(a) (b)

Figure 54. Comparison of TALIF and Radar REMPI measurements of atomic oxygen produced by a 4 kV pulsed discharge in a 1% O_2/He mixture at 100 Torr. Normalized atomic oxygen density shown as (a) spatial profile and (b) temporal profile.

CHAPTER VII

REDUCTION OF BREAKDOWN THRESHOLD BY METAL NANOPARTICLE SEEDING IN A DC MICRODISCHARGE

This article, “Reduction of Breakdown Threshold by Metal Nanoparticle Seeding in a DC Microdischarge”, was received on the 20th of October 2014, accepted on the 23rd of December 2014, and published on the 28th of January 2015.

Author affiliations:

Jordan Sawyer[1], Jacques Abboud[1], Zhili Zhang[1], and Steven F. Adams[2]

[1]Department of Mechanical, Aerospace and Biomedical Engineering, University of Tennessee, Knoxville TN 37996

[2]Air Force Research Laboratory (AFRL/RQQE), Wright-Patterson AFB, OH 45433-7919

Sawyer, J., et al., Reduction of breakdown threshold by metal nanoparticle seeding in a DC microdischarge. Nanoscale Research Letters, 2015. **10**(1): p. 1-6

Abstract

Significant reduction of the breakdown threshold in a DC microdischarge via seeding metal nanoparticles has been demonstrated. Compared to standard Paschen curves in dry air, reductions in the breakdown voltage of 5 to 25% were obtained for PD values (the product of pressure and electrode gap distance) ranging from 20 to 40 Torr-cm by seeding aluminum and iron nanoparticles with mean sizes of 75nm and 80nm, respectively. No secondary energy source was required to achieve this breakdown threshold reduction. From high-speed chemiluminescence imaging of the discharge evolution, breakdown was shown to be initiated at reduced voltages. Following breakdown, the increase in temperature ignited some of the nanoparticles near the cathode. Results suggest that possible charging of the nanoparticles within the gap may reduce the effective transient distance, leading to the threshold reduction.

Introduction

The mechanisms for breakdown in gas discharges have been studied extensively for over a century.[1] It is well known that the voltage required to initiate breakdown of a gaseous DC discharge depends strongly on the pressure *P* multiplied by the distance *D* of the gap between the electrodes, *PD*, as described by Paschen's Law.[2] For a gas at atmospheric pressure, by limiting the inter-electrode separation to a distance of less than a millimeter, it is possible to produce a stable "normal-glow" microdischarge.[3] Although such a microdischarge is spatially confined compared to a traditional low pressure discharge, the normal glow properties of a non-thermal discharge still apply, such as an electron temperature, T_e, which is several orders of magnitude larger than the gas temperature, T_g.[3-5] Many applications have been explored to exploit this excess electron energy and drive optical or chemical processes such as: vacuum-ultraviolet light sources[6], biomedical systems [7, 8], nanoparticle synthesis[9, 10], and plasma ignition[11]. However in atmospheric air, even with a small inter-electrode separation of less than 1 mm, a sizeable voltage (upwards of 4 to 5 kV) may still be required to initiate breakdown.

A significant reduction of the breakdown threshold within a microdischarge could be a breakthrough that enables numerous applications. Such a breakdown voltage reduction could allow for the use of smaller, cheaper, and safer power supplies. One method of reducing the voltage required to initiate breakdown is to generate seed electrons into the discharge region. Breakdown under these conditions is termed "under-voltage breakdown". Previously studied techniques for achieving under-voltage breakdown have included electron seeding by illumination of the cathode by ultraviolet (UV) light[12-14], resonance enhanced multi-photon ionization (REMPI) by UV pulsed lasers [15, 16], and the use of secondary electrodes or spark plugs[17]. The major limitation of these methods is that they all require a secondary energy source in order to produce the seed electrons which can increase the overall cost, complexity, and weight of the microdischarge system.

On the other hand, the effect of solid particle contamination, whether intentionally introduced or not, on the breakdown process in air gaps has been explored previously. Unwanted solid particle contaminants in commercial electrical systems can lead to arcing and failure of transmission lines and gas insulation systems. Sand and dust with particle sizes above several tens of microns were shown to initiate breakdown across gap lengths of several centimeters.[18, 19] The previous works concluded that the sand and dust particles in the inter-electrode gap played a negligible role in the volume processes during breakdown; however, the formation of a thin contaminant layer on the cathode enhanced secondary electron emission and significantly reduced the breakdown voltage in some circumstances. Other works have shown that larger (100s of microns to 100s mms) conductive particles in an inter-electrode air gap can play a significant role in reducing breakdown voltage, time-lag of impulses, and breakdown probability.[20-22] These previous works have concluded that the degree of influence that the solid particles have on the breakdown process depends on both the discharge properties, namely polarity and field uniformity, as well as properties of the particles such as conductivity, shape, size, concentration, and position relative to the electrodes.

In this study, aluminum and iron nanoparticles were seeded into a DC microdischarge at a very low flow speed. Experimental results indicate that breakdown thresholds of dry air with nanoparticle seeding were significantly reduced compared to standard Paschen law. High-speed chemiluminescence images reveal that the nanoparticles had a major influence in inducing breakdown and subsequent heating that eventually ignited the nanoparticles.

Experimental Setup

The experimental setup consisted of three major components: 1) a microdischarge cell with a gas and particle handling system that produces a DC microdischarge either with or without nanoparticle seeding, 2) a high-voltage power supply, high-voltage probes and data acquisition systems, and 3) a high-speed camera for luminosity measurements. In Figure 55, a home-made glass cell (inner diameter = 1 inch) was equipped with two adjustable electrodes. The cathode was a circular aluminum plate while the anode was a stainless steel needle oriented orthogonally to the circular plane of the cathode. The cathode was attached to the head of a micrometer so that its position relative to the anode could be accurately controlled. The distance between the two electrodes was set to roughly zero as verified by measuring the resistance across the gap with a multimeter. The gap between the electrodes could be determined accurately down to a 0.03 mm resolution.

A custom-made particle seeder, which included a particle container, inlet and outlet tubes, was used to seed the flow with various nanoenergetic materials. Mass measurements, before and after each run, were used to estimate the particle flow rates. Usually about 5 g of aluminum or iron nanoenergetics (nominal diameters of 70 nm, purchased from NanoAmor Inc. without further treatment) were placed along the flow path inside the particle container. The particle seeder inlet tube was submerged below the surface of the piles to generate particle suspensions inside the container. The height of the inlet and outlet were offset to ensure roughly uniform seeding in the flow through the discharge tube. Standard breathing dry air was used as the gas supply. A flow controller (Omega, FMA 5400) regulated the flow rate in the system to 1 ± 0.1 slpm (standard liters per minute). A three-way valve allowed the flow to be switched between the nanoparticle seeder and a bypass line. If particle seeding was desired, the three-way valve and needle valve were opened to allow flow through the seeder. Otherwise the three-way valve and needle valve were closed to isolate the particle seeder. The pressure in the system was monitored downstream of the cell by a piezoelectric pressure sensor (Kurt J. Lesker Company, Series 910), and the desired pressure was obtained by adjusting the needle valve upstream of the vacuum pump.

The high-voltage system included a high-voltage power supply, high-voltage probes, and data acquisition systems. The output of the high-voltage power supply was controlled via Labview^{TM} software on a personal computer. The positive terminal was connected to a 1 MΩ ballast resistor used to limit the current through the discharge circuit. When a sufficient positive voltage was applied to the anode, breakdown occurred within the air between the two electrodes, with the resulting current spike traveling through the circuit to the grounded cathode. The supply voltage was linearly increased until breakdown was achieved. Two high-voltage probes were used to monitor the voltage drop across the electrode gap and across the ballast resistor. The voltage drop across the electrode gap, V_1, was determined directly by measuring the potential at junctions before the anode and after the cathode. The current in the system was obtained by measuring the potential drop across the ballast resistor and electrode gap sequentially. The total applied potential across the ballast and gap could be expressed as $V_2=V_1+V_R$. Rearranging and dividing by the resistance of the ballast resistor, R, the current in the circuit was determined by Ohm's Law to be $I = (V_2-V_1)/R$.

A high-speed camera (Cooke Corporation, HS1200) was used to track the chemiluminescence from the plasma initiation and nanoparticle ignition events. The 2-D chemiluminescence images were acquired with a 1 ms exposure time. Because of the nature of the volume-averaged chemiluminescence images, the measurements can be regarded as an average over the line of sight across the discharge.

Results and Discussions

Figure 2 shows a comparison between theoretical Paschen curves for “clean” dry air and experimental measurements in air with and without Al and Fe nanoparticle seeding. Measurements of the breakdown voltage of the “clean” dry air were taken for a 1 mm gap distance with varying pressures of 200 to 400 Torr. For the dry air case, as seen in Figure 56, a maximum error of less than 12% was observed between theoretical and experimental breakdown voltages. Breakdown voltages for the dry air with nanoparticle seeding were experimentally determined for the 20 to 40 Torr-cm range. The experiment was performed with aluminum and iron nanoparticles with mean diameters of 80 and 75 nm, respectively. The number density flow rate of the nanoparticles had an upper bound of 1×10^{10} $cm^{-3}s^{-1}$ during the course of the experiment. The breakdown threshold values for all three curves appear to coalesce at the lower *PD* scaling close to 20 Torr-cm, however, the experimental data diverge from the theoretical values with increasing *PD* up to 40 Torr-cm. This situation is most commonly due to uncertainty in the secondary ionization coefficient of the cathode. It is clearly seen that nanoparticle seeding resulted in a reduction in the breakdown voltage for the entire 20 to 40 Torr-cm range. However, at lower *PD* values, nanoparticle seeding appeared to cause only a slightly reduced breakdown threshold of a few percent compared to the “clean” dry air case. On the contrary, at larger *PD* values, a more significant reduction in the breakdown voltage, approaching 25%, was apparent with nanoparticle seeding. In Figure 56 a general upward trend is seen in the percentage reduction for increasing PD for the 20 to 40 Torr-cm range. Seeding with Al nanoparticles consistently has a lower breakdown threshold compared to seeding with Fe nanoparticles. This may be due to the difference in electrical conductivity of the particles. Additionally, iron nanoparticles have been shown to have larger more porous oxidation layers which may negatively impact charging of the nanoparticles.[23] Mild day to day variations were seen in the experimental breakdown voltages most likely due to changes in the electrode surfaces over time despite rigorous efforts in polishing and cleaning; however, the above mentioned trends were consistently preserved.

Figure 57 shows a typical plot of the discharge current as the applied voltage was gradually increased, both with and without Al nanoparticle seeding. Initially, in both cases, there is negligible current in the circuit prior to breakdown. Without nanoparticle seeding, there is an almost immediate sharp increase in current at the breakdown voltage. With nanoparticle seeding, short-lived instabilities manifest as peaks in current just prior to breakdown. A slightly elevated current is present as well in the instability region. Once the breakdown threshold was reached in each discharge, there was negligible difference in current at similar applied voltages. Similar properties are shown for the measured gap voltage, with and without aluminum nanoparticle seeding, as shown in Figure 58. Without nanoparticle seeding, there is a sharp decrease in voltage across the gap at the breakdown voltage. For the case with nanoparticle seeding, instabilities appear as dips in the voltage just prior to breakdown. Once the breakdown threshold is reached, it is apparent from the two plots that the nanoparticle seeding causes negligible change to conductivity of the sustained discharge.

Figure 59 shows high speed images of the discharge gap taken during the breakdown process with a resolution of 2 ms between frames. Analysis of these images revealed that the breakdown occurs within the first 2 ms of applying the voltage. Ignition of the nanoparticles due to thermal effects was observed at 4 ms. It was confirmed that breakdown always occurs before the ignition of metal nanoparticles at various conditions. The delay between gas breakdown and the ignition of the nanoparticles varied. In conditions at pressures close to atmosphere and/or larger electrode separations, the thermal ignition of the nanoparticles was both more abundant and less delayed from the breakdown, which was likely due to the higher temperatures under those conditions. Overall, the nanoparticles first acted to reduce the voltage threshold required for gas breakdown. Subsequently the discharge ignited some of the particles between electrodes.

Figure 60 shows scanning electron microscope (SEM) images and statistical analyses of particle sizes from samples of the nanoparticles used in this study. Both the aluminum and iron nanoparticle samples appeared to have Gaussian distributions; however, the mean size of the aluminum nanoparticles is a bit smaller due to the thinner oxidized shell and lower degree of agglomeration. Such ex-situ diagnostic techniques could be used to build empirical correlations between reduction in breakdown voltage and characteristics of the particles such as size, shape, and degree of oxidation.

Based on the experimental observations, the mechanisms for reducing the breakdown threshold may be due to possible charging of the nanoparticles within the gap, which may reduce the effective distance. Since the current across the gap does not vary with and without nanoparticle seeding, the increased conductivity due to the presence of metal nanoparticles is small. Additionally nanoparticles do not start to combust before the breakdown. The Joule heating due to the presence of metal nanoparticles is slow compared to breakdown generation. However evidence of charging of the metal nanoparticles within the gap has been observed in these experiments. For example in Figure 59, the attraction of the nanoparticles to the cathode and the subsequent ignition near the cathode region indicate that the nanoparticles were positively charged. In addition, the chemiluminescence image at 2 ms shows a brighter glow near the cathode, which suggests that the evolution of the breakdown started from anode and turned toward the cathode. The nanoparticles charging and shifting toward the cathode might allow the nanoparticles to serve as effective electrodes within the gap, which could mimic a reduction in the gap distance. It is speculated that the Paschen curve may still hold for the particle laden flow with the addition of the conducting nanoparticles near the cathode leading to an effective reduction in distance between the electrodes, i.e., the PD values on the x axis are reduced.

Conclusions

In this work, the seeding of metal nanoparticles was shown to reduce the voltage required to initiate breakdown in an air DC microdischarge. Reductions in the breakdown voltage were seen to be as high as 25% for a *PD* scaling of 40 Torr-cm. High-speed chemiluminescence imaging of the discharge region revealed that the breakdown process was enhanced by a reduction in the required voltage from nanoparticle seeding, and then heating from the discharge led to ignition of some of the nanoparticles as they flowed through the discharge region. The use of SEM imaging gave detailed information regarding the particle size, shape, and oxidation distributions. Further use of ex-situ diagnostic techniques, such as SEM analyses, could allow for the development of empirical correlations between particle characteristics and reduction in the breakdown voltage. Visual evidence of particle charging being the most likely mechanism for breakdown voltage reduction and subsequent reduction of the effective distance between the electrodes has been presented.

Acknowledgements

We acknowledge support from the AFOSR and NSF CBET-1032523 and CBET - 1346944.

References

1. Townsend, J., *Electricity in gases*. 1915, Oxford,: Clarendon Press. xv, 406 p. incl. tables, diagrs.

2. Paschen, F., Ueber die zum Funkenübergang in Luft, Wasserstoff und Kohlensäure bei verschiedenen Drucken erforderliche Potentialdifferenz. Annalen der Physik, 1889. **273**(5): p. 69-96.

3. Foest, R., M. Schmidt, and K. Becker, *Microplasmas, an emerging field of low-temperature plasma science and technology.* International Journal of Mass Spectrometry, 2006. **248**(3): p. 87-102.

4. Sawyer, J., et al., O2 rotational temperature measurements in an atmospheric air microdischarge by radar resonance-enhanced multiphoton ionization. Journal of Applied Physics, 2013. **113**(23): p. -.

5. Laux, C.O., et al., *Optical diagnostics of atmospheric pressure air plasmas.* Plasma Sources Science and Technology, 2003. **12**(2): p. 125.

6. Ren'an, B., et al., *Development of 146nm Vacuum UV Light Source.* Physics Procedia, 2012. **32**(0): p. 477-481.

7. Goree, J., et al., *Killing of S. mutans Bacteria Using a Plasma Needle at Atmospheric Pressure.* Plasma Science, IEEE Transactions on, 2006. **34**(4): p. 1317-1324.

8. Kim, J.Y., et al., 15-μm-sized single-cellular-level and cell-manipulatable microplasma jet in cancer therapies. Biosensors and Bioelectronics, 2010. **26**(2): p. 555-559.

9. Chiang, W.-H. and R.M. Sankaran, Microplasma synthesis of metal nanoparticles for gas-phase studies of catalyzed carbon nanotube growth. Applied Physics Letters, 2007. **91**(12): p. 121503-3.

10. Richmonds, C. and R.M. Sankaran, Plasma-liquid electrochemistry: Rapid synthesis of colloidal metal nanoparticles by microplasma reduction of aqueous cations. Applied Physics Letters, 2008. **93**(13): p. 131501-3.

11. Pancheshnyi, S.V., et al., *Ignition of Propane–Air Mixtures by a Repetitively Pulsed Nanosecond Discharge.* Plasma Science, IEEE Transactions on, 2006. **34**(6): p. 2478-2487.

12. Frechette, M.F., N. Bouchelouh, and R.Y. Larocque. Laser-induced undervoltage breakdown in atmospheric N₂ correlated with time-resolved avalanches. in Electrical Insulation, 1994., Conference Record of the 1994 IEEE International Symposium on. 1994.

13. Kluckow, R., Über den zeitlichen Verlauf des Stromes einer Gasentladung in Wasserstoff. Zeitschrift für Physik, 1961. **161**(4): p. 353-369.

14. Varney, R.N., Liberation of Electrons by Positive-Ion Impact on the Cathode of a Pulsed Townsend Discharge Tube. Physical Review, 1954. **93**(6): p. 1156-1160.

15. Cooley, J.E. and E.Y. Choueiri, *Threshold criteria for undervoltage breakdown.* Journal of Applied Physics, 2008. **103**(9): p. -.

16. Cooley, J.E., Fundamentals of undervoltage breakdown through the Townsend mechanism. 2008.

17. Hong, T. and V. Scuka, *The breakdown mechanism of a mid-plane triggered spark gap trigatron.* Dielectrics and Electrical Insulation, IEEE Transactions on, 1996. **3**(6): p. 843-848.

18. Al-Arainy, A.A. The influence of dust particles on the DC breakdown voltage of rod-rod air gaps. in Electrical Insulating Materials, 1995. International Symposium on. 1995.

19. Al-Arainy, A.A., N.H. Malik, and M.I. Qureshi, *Influence of sand/dust contamination on the breakdown of asymmetrical air gaps under lightning impulses.* Electrical Insulation, IEEE Transactions on, 1992. **27**(2): p. 193-206.

20. Kubuki, M., et al., *Estimation of dc breakdown mechanisms in air gaps containing floating metallic particles.* Dielectrics and Electrical Insulation, IEEE Transactions on, 1997. **4**(1): p. 92-101.

21. Hara, M. and M. Akazaki, A method for prediction of gaseous discharge threshold voltage in the presence of a conducting particle. Journal of Electrostatics, 1977. **2**(3): p. 223-239.

22. Hara, M., et al., *Particle-triggered pre-breakdown phenomena in atmospheric air gap under AC voltage.* Dielectrics and Electrical Insulation, IEEE Transactions on, 2005. **12**(5): p. 1071-1081.

23. Chong, X., J. Abboud, and Z. Zhang, Plasmonics Resonance Enhanced Active Photothermal Effects of Aluminum and Iron Nanoparticles

Appendix

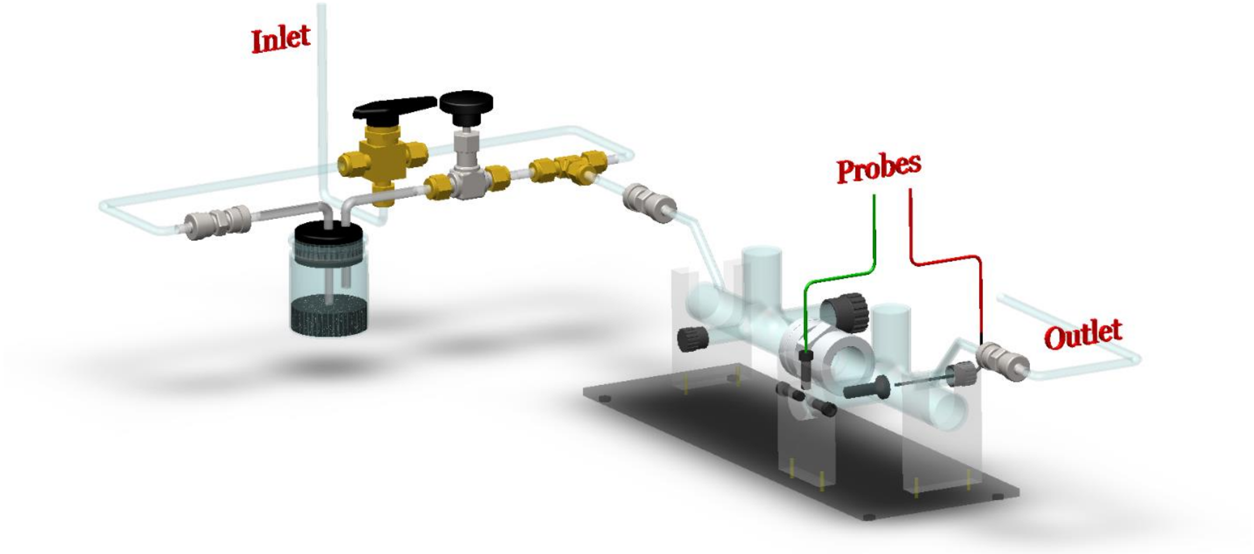

Figure 55. Discharge cell setup for the flow system and particle seeder.

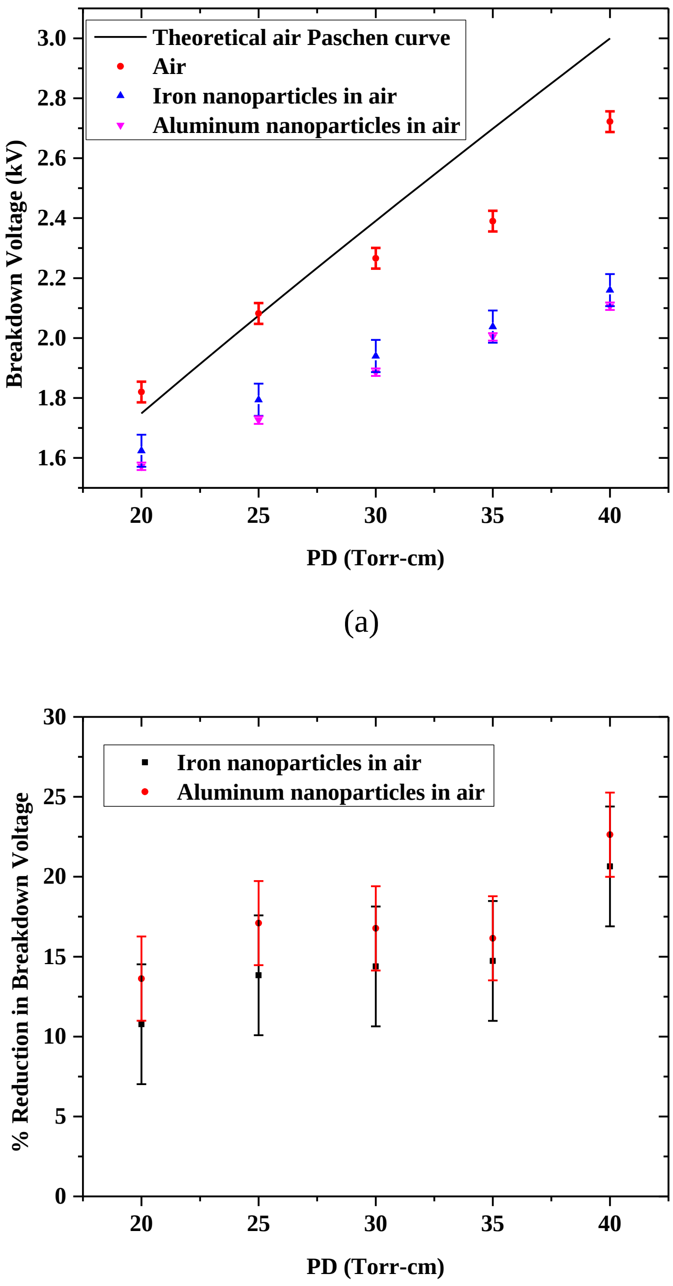

(a)

(b)

Figure 56. (a) Comparison of Paschen curves for “clean” dry air and dry air with nanoparticle seeding with error bars corresponding to one standard deviation. (b) Percent reduction in breakdown voltage from “clean” dry air with aluminum and iron nanoparticle seeding with error bars corresponding to one standard deviation.

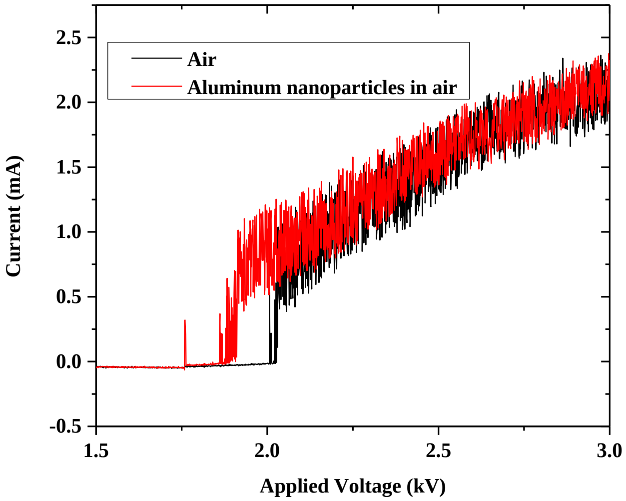

Figure 57. Discharge current versus applied voltage with and without seeding of aluminum nanoparticles at PD=25 Torr-cm.

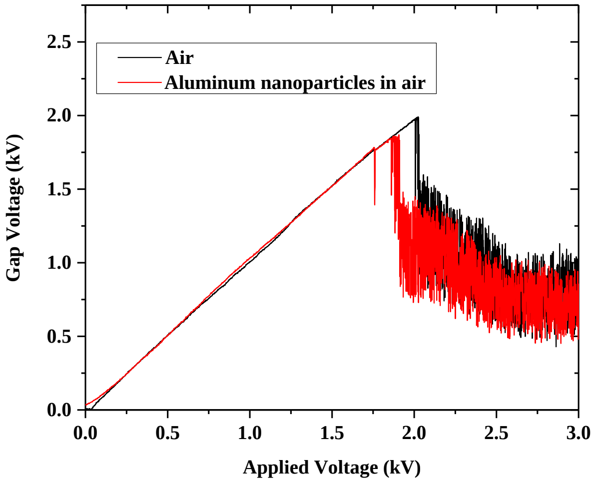

Figure 58. Gap voltage versus applied voltage with and without seeding of aluminum nanoparticles at PD=25 Torr-cm.

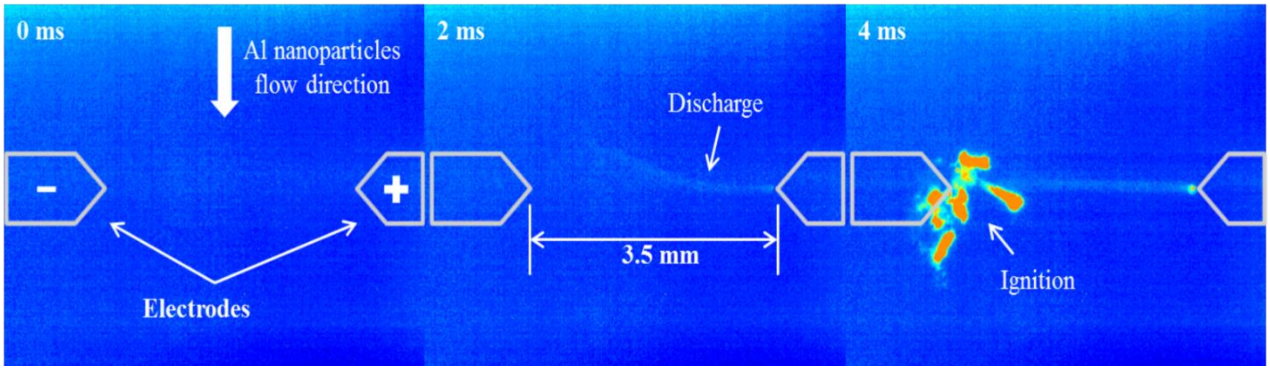

Figure 59. High-speed chemiluminescence images of breakdown in a 3.5 mm gap in atmospheric air.

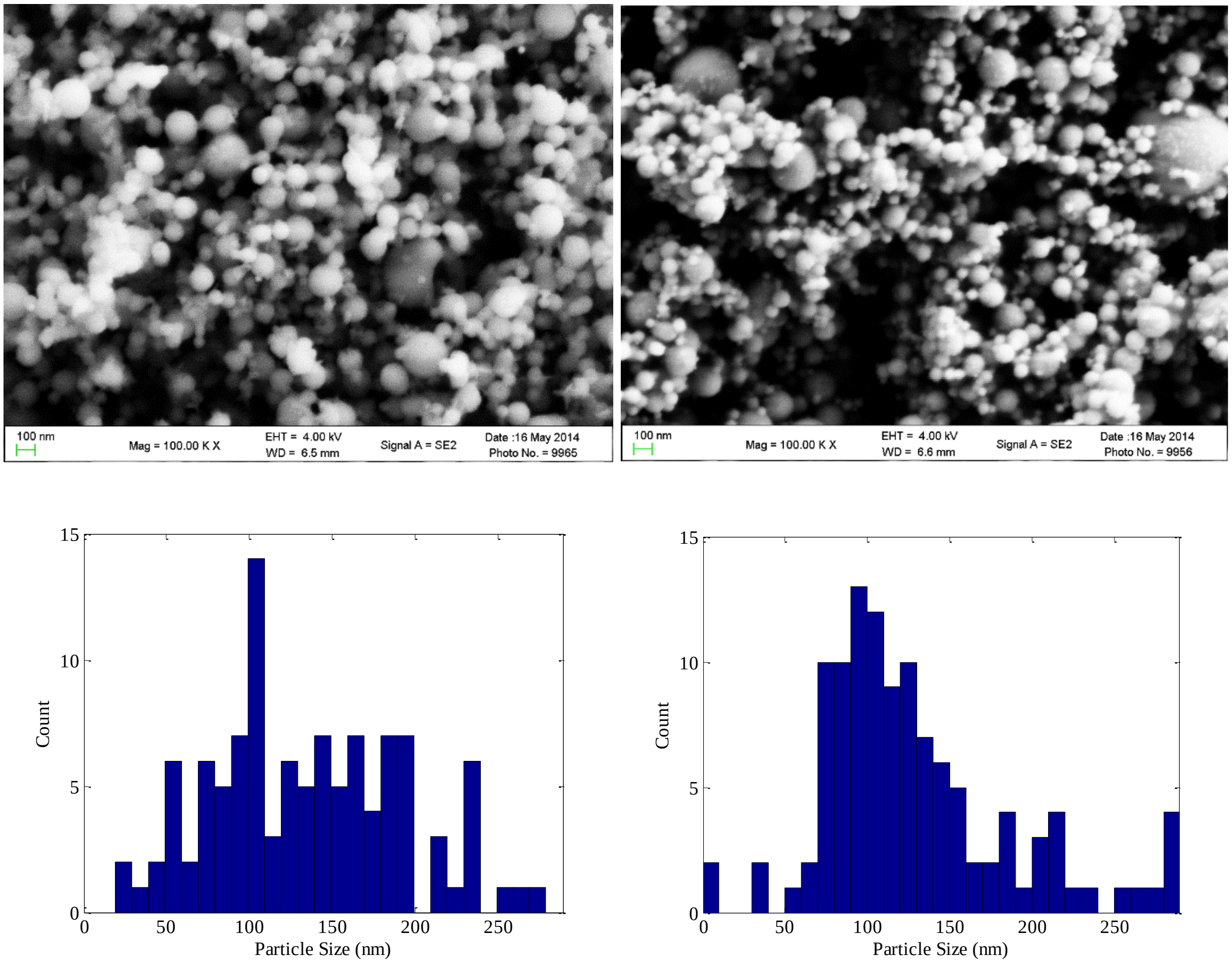

Figure 60. SEM images of (left) Al and (right) Fe nanoparticle samples, and (bottom) statistical analysis of the size distribution of the two samples

CONCLUSION

In the seven chapters of this dissertation novel approaches for the generation and microwave scattering diagnostics of small volume plasmas were presented. Laser-induced plasmas (i.e. laser-induced breakdown and resonance enhanced multiphoton ionization) and non-equilibrium microdischarges are the small volume plasmas illustrated in this work. Excluding the newest work, Chapter 5 “Atomic Oxygen Measurements in a Low Pressure DC and Pulsed Discharge via Radar REMPI”, portions of all of the individual chapters have been published in peer-reviewed journals. Chapter I presents the application of microwave scattering theory to laser-induced breakdown in air. The MIE solution to Maxwell’s equations is employed to reveal three distinct phases of the evolution of the laser-induced breakdown in air. Chapter II presents a novel method of quantifying thresholds for laser-induced breakdown. These thresholds are established via total electron number measurement from dielectric calibration of microwave scattering. Chapter III presents high-repetition-rate (HRR) nanosecond laser pulse train scheme for laser ignition. Demonstration of the ignition of combustible gaseous mixtures is shown to have an order-of-magnitude reduction in per-pulse energy using the HRR LI method over traditional laser ignition methods. Chapter IV presents ion-kinetic measurements of a laser induced plasma in sodium-argon and sodium-air gaseous mixtures. Coherent microwave Rayleigh scattering (Radar) from Resonance Enhanced Multi-Photon Ionization (REMPI) is utilized for the measurement of sodium ion neutral stabilized and cluster dissociative recombination rates.

Chapter V presents rotational temperature measurements in a DC microdischarge produced in air. Radar REMPI measurements of O_2 rotational temperature is performed at eight axial locations between pin-to-pin electrodes. Chapter VI presents relative concentration measurements of atomic oxygen in DC and pulsed Discharges. Relative atomic oxygen conenctrations were obtained via

Radar REMPI. The effects of pressures, gas composition, and discharge voltage were explored for the DC and pulsed discharges. Comparisons between two-photon absorption laser induced fluorescence (TALIF) and Radar REMPI techniques were made for atomic oxygen concentration measurements in a pulsed discharge. Chapter VII presents a method of reducing the breakdown voltage of a DC microdischarge via metal nanoparticle seeding. Reductions in the breakdown voltage were seen to be as high as 25% for a *PD* scaling of 40 Torr-cm from the seeding of iron and aluminum nanoparticles into the discharge gap.

VITA

Jordan Chase Sawyer was born in Knoxville, TN and raised in Morristown TN. In 2007 he enrolled at the University of Tennessee, Knoxville. In the spring of 2011 he obtained his Bachelor of Science in Aerospace Engineering from the University of Tennessee, Knoxville. In the fall of 2013 he obtained his Master of Science in Aerospace Engineering from the University of Tennessee, Knoxville. His Ph.D. research has focused on small volume plasma generation and diagnostics for engineering applications.